Transport and Coherence Properties of Indirect Excitons in Coupled Quantum Wells

Leonidas Mouchliadis

A Thesis submitted to
Cardiff University
for the degree of
Doctor of Philosophy

April 2008

UMI Number: U585113

UMI

Dissertation Publishing

UMI U585113

ProQuest

Declaration

This work has not previously been accepted in substance for any degree and is not being concurrently submitted in candidature for any degree.

Signed: _____

Candidate

Date: _____

07/04/2008

Statement 1

This thesis is being submitted in partial fulfillment of the requirements for the degree of Doctor of Philosophy.

Signed: _____

Candidate

Date: _____

07/04/2008

Statement 2

This thesis is the result of my own independent investigation, except where otherwise stated. Other sources are acknowledged by explicit references.

Signed: _____

Candidate

Date: _____

07/04/2008

Statement 3

I hereby give consent for my thesis, if accepted, to be available for photocopying and for inter-library loan, and for the title and summary to be available to outside organisations.

Signed: _____

Candidate

Date: _____

07/04/2008

Statement 4

I hereby give consent for my thesis, if accepted, to be available for photocopying and for inter-library loans, after expiry of a bar on access previously approved by the Graduate Development Comittee.

Signed: _____

Candidate

Date: _____

To Argyro and my parents

ACKNOWLEDGEMENTS

It has been a great privilege to have been supervised by Prof. Alexei Ivanov, who has guided me through my first steps in research and has assisted me to overcome all the obstacles I have met in the way. I am also grateful to Prof. Leonid Butov and his group at the University of California, San Diego who helped me to obtain a better understanding of the experiments and Prof. Kikuo Cho for many interesting discussions during his stay in Cardiff. I would also like to thank Aaron Hammack and Chih-Wei Lai for providing me with their experimental results and the excellent collaboration we had.

I am indebted to my office mates Celestino, Lois and Nikolay for their support and assistance and for valuable discussions on physical and computational problems. Many thanks to Fabio as well for always being eager to help me with numerics.

I would also like to express my gratitude to my professors at the University of Crete who provided me with a solid background in Physics and especially E. N. Economou, P. Lambropoulos and G. C. Psaltakis.

Many thanks to Thomas, Meletis, Marco and Danilo for their friendship and pleasant company during the last three years in Cardiff. Thanks in particular to Meletis for reading through my thesis, and giving useful suggestions.

Last but not least, I am grateful to my parents Anastasios and Styliani and my sister Argyro for their continuous support during my studies all these years. This dissertation would never be possible without their help and it is dedicated to them.

ABSTRACT

This dissertation consists of a theoretical investigation into the transport and co-herence properties of indirect excitons in coupled quantum wells (QWs) at helium temperatures.

The motion of excitons along the quantum well plane is described through a quantum diffusion equation and the possibility of excitonic cloud formation is studied both due to the natural potential fluctuations and externally applied confining potentials. The photoluminescence (PL) of decaying excitons is used as a probe for their properties such as concentration, effective temperature and optical lifetime.

The exciton thermalisation from an initial high energy to the lattice temperature is achieved within their lifetime due to a very effective coupling between the exciton states and a continuum of phonon states, a direct consequence of the relaxation of momentum conservation along the growth direction of a QW. Moreover, the natural spatial separation between electrons and holes prevents their recombination, resulting in long lifetimes.

The dynamics of the system of excitons in optically-induced traps is also studied and the numerical solution of the quantum diffusion equation provides an insight into the extremely fast loading times of the trap with a highly degenerate exciton gas. The hierarchy of timescales in such a trap allows for the creation of a cold and dense gas confined within the trap, opening a new route towards the long sought Bose-Einstein Condensation (BEC) in solid state.

Finally the issue of exciton spatial coherence is studied and an analytic expression for the coherence function, i.e., the measure of the coherence in a system, is derived. A direct comparison with large coherence lengths recently observed in systems of quantum well excitons and microcavity polaritons is attempted and interesting conclusions are drawn regarding the build up of spontaneous coherence in these systems.

PUBLICATIONS

L Mouchliadis and A L Ivanov. First-order spatial coherence of excitons in planar nanostructures: A k-filtering effect. *Phys. Rev.* B **77**, 033306, 2008.

A A High, A T Hammack, L V Butov, L Mouchliadis, A L Ivanov, M Hanson and A C Gossard. Localization and interaction of indirect excitons in GaAs coupled quantum wells. Submitted to Phys. Rev. Lett., 2008.

A T Hammack, L V Butov, L Mouchliadis, A L Ivanov and A C Gossard. Kinetics of indirect excitons in an optically induced trap in GaAs quantum wells *Phys. Rev.* B **76**, 193308, 2007.

L Mouchliadis and A L Ivanov. Anti-trapping of indirect excitons by a current filament. *J. Phys.: Condens. Matter* **19**, 295215, 2007.

L Mouchliadis, C W Lai and A L Ivanov. Current induced anti-traps for indirect excitons. *Superlat. and Microstr.* **41**, 392, 2007.

PRESENTATIONS

L Mouchliadis, L E Smallwood, A L Ivanov, A T Hammack, L V Butov and A C Gossard. Dynamics of indirect excitons in optically-induced traps. *Condensed Matter and Materials Physics Conference (CMMP)*, Leicester (12-13 April 2007).

A T Hammack, L V Butov, L Mouchliadis, L E Smallwood, A L Ivanov, and A C Gossard. Kinematics of cold excitons in the laser-induced exciton trap. *APS March Meeting Physics Conference*, Denver (12-13 March 2007).

L Mouchliadis and A L Ivanov. Electric current-induced anti-traps for indirect excitons. *6th International Conference on the Physics of Light Matter Coupling in Nanostructures (PLMCN6)*, Magdeburg (25-29 September 2006).

L Mouchliadis and A L Ivanov. Space charge induced transport of electrons, holes and excitons in coupled quantum wells. *Photon Mediated Phenomena Meeting*, Cambridge (23-26 June 2006).

CONTENTS

LIST OF FIGURES

1 INTRODUCTION

Physical phenomena in lower than three dimensions have attracted huge scientific interest in the past decades due to their unusual nature. The modern advent in the fabrication of low-dimensional systems has initiated a substantial amount of experimental and theoretical work on these systems. In particular, quasi-two-dimensional excitons created in quantum well structures have been thoroughly investigated, as their long lifetime renders them unique candidates for the appearance of Bose-Einstein condensation in a solid state system.

In this thesis the transport of excitons in the quantum well plane is studied theoretically and modelled numerically and a direct comparison with experimental results is attempted. In particular, the influence of local potential fluctuations – both intrinsic and extrinsic – in the exciton transport is analysed and the utilisation of these repulsive and attractive potentials for the creation of a degenerate exciton gas is discussed.

The main challenge is that excitons reach a quasi-equilibrium within their lifetime, *i.e.*, before they decay radiatively, and therefore an effective temperature of the excitonic gas can be established. The appearance of spontaneous coherence in such a non-equilibrium system is an issue of current investigation.

1.1   OVERVIEW

The first Chapter provides the necessary background information for the work pre-
sented in the remainder of the thesis. The system of indirect excitons is described
theoretically and its main properties are studied. An extensive literature review serves
as a guide to the vast experimental and theoretical results present in the bibliography.

The following Chapter is entitled "Exciton rings formation" and deals with the ex-
planation of photoluminescence (PL) patterns reported in experiments with laser
excitation in quantum wells (QWs). Several randomly distributed PL rings appeared
in these experiments enclosed by an external ring of macroscopic diameter. As the po-
sitions of the PL centres remained unchanged, they were ascribed to current filaments
crossing the quantum well plane and creating a high energy electron gas embedded
in a hole rich area. The creation of excitons by binding of the oppositely charged
electrons and holes occurs in the interface of the two regions giving rise to excitonic
rings. Exciton creation is therefore described by a quantum mass action law and the
calculated ring size around the repulsive potential of the filament is in agreement with
the experimental data.

In the third Chapter entitled "Dynamics of indirect excitons in optical traps", the
kinetics of an optically confined exciton gas is studied by means of a quantum dif-
fusion and a thermalisation equation. Direct comparison with recent experimental
results reveals an excellent agreement between theory and experiment. The motion
of excitons towards the centre of the optical trap is accompanied by scattering with
phonons which results in the exciton thermalisation towards the lattice temperature.
An increase in the diffusion coefficient with time is understood in terms of effective
screening of the quantum well interface roughness. The short – compared to the other
timescales in the system – trap loading time, renders optical trapping of excitons a
powerful method for the creation of a dense, degenerate gas of bosons.

In Chapter four the issue of excitonic coherence is addressed in connection with recent
reports on large coherence lengths in systems of quantum well excitons and micro-
cavity polaritons. The difference on the decay of correlations between classical and
Bose-Einstein statistics is analysed and the first-order coherence function is calculated
for a 2D system of bosons. An increase of the coherence length with decreasing tem-
perature is shown and various asymptotic limits are obtained. In order to explain the
macroscopically large coherence lengths observed in the experiments the concept of

k-filtering is introduced while the effect of interactions between excitons is also taken into account. Although the dipole-dipole repulsion between indirect excitons tends to limit spatial coherence, the collection of PL signal from a small angular aperture reflects a very narrow distribution in momentum space and, as a result, maintenance of the coherence for large distances. The sharp cut-off in momentum space is responsible for the oscillatory behaviour of the coherence function indicating the appearance of interference.

Finally in Chapter five the main conclusions are summarised and future prospects are proposed.

1.2 EXCITONS

According to solid state theory, the discrete electronic states of isolated atoms turn into allowed energy bands separated by forbidden energy gaps when many of these atoms are brought together to form a crystal lattice [4]. In the simplest case, the ground state of a semiconductor comprises a fully occupied valence band and a completely empty conduction band. The lowest single-particle electronic excitations are an additional electron in the conduction band or a single empty orbital – a hole – in the valence band characterised by effective masses m_e and m_h, respectively, and equal but positive charges. When an electron is promoted from the valence to the conduction band, usually by absorbing a photon with energy equal to or greater than the bandgap energy, it is accompanied by the creation of a positively charged hole in the valence band, and the Coulomb interaction between them tends to create a bound state, as is schematically depicted in Fig. 1.1. This two-particle excitation is called an *exciton* and can be seen as an electronic excitation travelling in a periodic structure [5].

Excitons can be tightly bound essentially localised in a single lattice site or weakly bound with a radius extending over many lattice constants. In the former case they are called Frenkel excitons [6, 7] and appear most commonly in biological molecules and molecular crystals, whereas in the latter case they are called Wannier-Mott excitons [8, 9] and are typical in most semiconductors – herein only Wannier-Mott excitons are considered. Despite the similarities between an exciton and the hydrogen atom two main differences exist: (i) the effective masses of the electron and the hole are comparable and (ii) the Coulomb attraction is effectively screened by the presence of
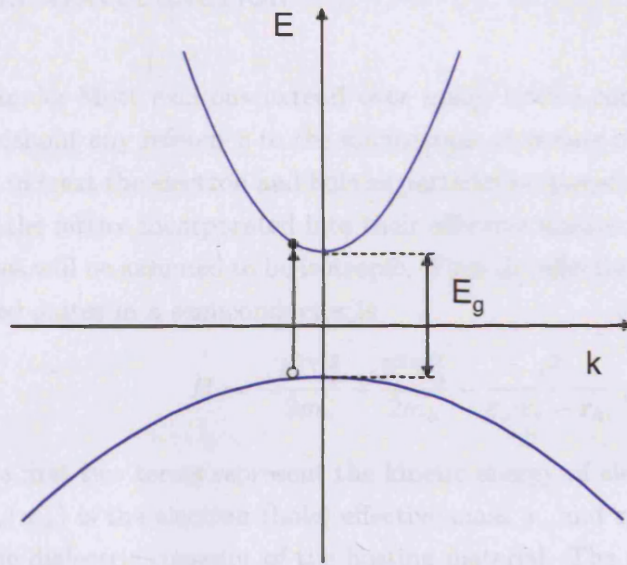
Figure 1.1: An idealised band structure of a direct-gap semiconductor in the vicinity of the Fermi energy and the the centre of the Brillouin zone. The arrow shows an electronic excitation where an electron is promoted from the valence to the conduction band, leaving a positively charged hole in the valence band.

the lattice atoms and therefore reduced by a factor equal to the dielectric constant of the hosting crystal.

Excitons are created by absorption of photons and are *metastable* as there is a finite probability for the excited electron to recombine with the hole. They are mobile and move through the solid carrying energy and momentum but not mass or charge. Being the compound of two fermions an exciton is expected to behave as a boson as long as the interparticle distance is large enough to prevent its fermionic constituents from feeling each other's presence. As the density increases the bosonic character is weakened and Pauli's exclusion principle results in an effective *phase space filling*. This transition in the nature of the system of free or bound electron-hole pairs makes it unique in the study of a broad range of phenomena from Bose-Einstein condensation (BEC) of excitons to superfluidity of an electron-hole liquid or appearance of the Mott insulator. In the following subsections a more formal approach to the properties excitons is presented and their main features are discussed with emphasis given on excitons in quantum wells.

EXCITON WAVEFUNCTION

Since Wannier-Mott excitons extend over many lattice constants, they can be described without any reference to the microscopic structure of their constituents. It is sufficient to treat the electron and hole as particles propagating in free space, with the effects of the lattice incorporated into their effective masses. For simplicity the effective masses will be assumed to be isotropic. Thus the effective Hamiltonian describing the excited states in a semiconductor is

$$H = -\frac{\hbar^2 \nabla_e^2}{2m_e} - \frac{\hbar^2 \nabla_h^2}{2m_h} - \frac{e^2}{\varepsilon_b |\mathbf{r}_e - \mathbf{r}_h|}, \tag{1.1}$$

where the first two terms represent the kinetic energy of electrons and holes respectively, $m_e(m_h)$ is the electron (hole) effective mass, $\mathbf{r}_e$ and $\mathbf{r}_h$ the spatial coordinates and ε_b the dielectric constant of the hosting material. The third term is the mutual Coulomb attraction between the oppositely charged electron and hole, screened by the electrons in the valence band and the ions in the lattice.

The eigenstates of Hamiltonian (1.1) comprise a series of bound states, the excitonic states, and a continuum of free electron-hole pairs. Making a coordinate transformation to the centre of mass $\mathbf{R} = (m_e \mathbf{r}_e + m_h \mathbf{r}_h)/M_\mathrm{x}$ and relative coordinates $\mathbf{r} = \mathbf{r}_e - \mathbf{r}_h$, Eq. (1.1) may be rewritten as

$$H = -\frac{\hbar^2 \nabla_R^2}{2M_\mathrm{x}} - \frac{\hbar^2 \nabla_r^2}{2\mu} - \frac{e^2}{\varepsilon_b r}, \tag{1.2}$$

where $M_\mathrm{x} = m_e + m_h$ is the total mass and $\mu = m_e m_h / M_\mathrm{x}$ is the reduced mass. In this coordinate system the envelope wavefunction is written as the product

$$\Psi(\mathbf{R}, \mathbf{r}) = \Phi(\mathbf{R})\, \varphi_n(\mathbf{r}). \tag{1.3}$$

Here, $\Phi(\mathbf{R})$ describes the free motion of the centre of mass of the exciton and $\varphi_n(\mathbf{r})$ is a hydrogen-like wave function with effective Rydberg energy

$$Ry^* = \frac{\mu e^4}{2\hbar^2 \varepsilon_b^2} = \frac{\hbar^2}{2\mu a_0^2}, \tag{1.4}$$

where the excitonic Bohr radius is given by

$$a_0 = \frac{\hbar^2 \varepsilon_b}{e^2 \mu}. \tag{1.5}$$

Thus an exciton related to a pair of parabolic bands has the following energy dispersion relation:

$$E_n = E_\text{g} + \frac{\hbar^2 k^2}{2M_\text{x}} - \frac{Ry^*}{n^2}, \qquad n = 1, 2, 3, \dots \tag{1.6}$$

where n is the principal quantum number. Note that here we neglect the electron-hole exchange interaction which leads to extra shifts and splittings of the exciton states. For typical values of GaAs with relative permittivity $\varepsilon_\text{b} \sim 10$ and ratio of the reduced mass to bare electron mass $\mu/m_0 \sim 0.05$, the exciton Bohr radius is $a_0 \sim 100\text{\AA}$ and the corresponding binding energy for the state with $n = 1$ is $E_\text{b} \sim 10\,\text{meV}$, thus the exciton is indeed a loosely bound and extended object.

In the framework of second quantisation formalism the Bloch states

$$\phi_{\mathbf{k},n}(\mathbf{r}) = \frac{1}{\sqrt{V}} e^{i\mathbf{k}\cdot\mathbf{r}} u_{\mathbf{k},n}(\mathbf{r}), \tag{1.7}$$

can be used as a basis to determine the actual electronic state of an exciton. These states are labelled by a wavevector in the first Brillouin zone, $\mathbf{k}$ and a band index n. The first excited state of a crystal containing one exciton of wavevector $\mathbf{K}$ is a superposition of free electron-hole pairs

$$|\mathbf{K}, n\rangle = B_{\mathbf{K},n}^\dagger |0\rangle = \frac{1}{\sqrt{V}} \sum_\mathbf{k} \phi_n(\mathbf{k}) a_{\beta\mathbf{K}+\mathbf{k}}^\dagger b_{\alpha\mathbf{K}-\mathbf{k}}^\dagger |0\rangle, \tag{1.8}$$

where $\alpha = m_e/M_\text{x}$, $\beta = m_h/M_\text{x}$, $a^\dagger$ and $b^\dagger$ denote the creation operator for an electron in the conduction band and a hole in the valence band, respectively and $\phi_n(\mathbf{k})$ is the internal exciton wavefunction in momentum space. Equation (1.8) defines the exciton creation operator $B_{\mathbf{K},n}^\dagger$ through the creation operators of electrons and holes. The corresponding commutation relations for the exciton operators read

$$[B_{\mathbf{K}',n'}, B_{\mathbf{K},n}] = 0, \tag{1.9}$$

$$[B_{\mathbf{K}',n'}^\dagger, B_{\mathbf{K},n}^\dagger] = 0, \tag{1.10}$$

$$[B_{\mathbf{K}',n'}, B_{\mathbf{K},n}^\dagger] = \delta_{\mathbf{K},\mathbf{K}'}\delta_{n,n'} - \frac{1}{V} \sum_\mathbf{k} \phi_{n'}^*(\mathbf{k})\phi_n(\mathbf{k})(1 - b_{\alpha\mathbf{K}-\mathbf{k}}^\dagger b_{\alpha\mathbf{K}-\mathbf{k}} - a_{\beta\mathbf{K}+\mathbf{k}}^\dagger a_{\beta\mathbf{K}+\mathbf{k}}). \tag{1.11}$$

The fact that excitons are bound states of two fermions and therefore should behave as bosons in the limit of low densities is readily reflected on the commutation relation (1.11). In this dilute limit the possibility of Bose-Einstein condensation (BEC) is a subject of ongoing research.

EXCITON OSCILLATOR STRENGTH

It is customary to describe the probability of a dipole transition from an initial state $|i\rangle$ with energy E_i to a final state $|f\rangle$ with energy E_f, in terms of the *oscillator strength*. In time-dependent perturbation theory, the oscillator strength $f_{\hat{\epsilon}}$ is a dimensionless quantity defined as

$$f_{\hat{\epsilon}} = \frac{2}{m_0 \hbar \omega} |\langle f | \hat{\epsilon} \cdot \sum_i \mathbf{p}_i | i \rangle|^2 , \tag{1.12}$$

where $\hbar\omega = E_f - E_i$, $\mathbf{p}_i$ are the momentum operators of the electrons, $\hat{\epsilon}$ is the polarisation vector related to the plane wave of frequency ω inducing the transition and m_0 is the free electron mass. Hence, the oscillator strength of the transition from the crystal ground state to the exciton state, is defined as [10]

$$f_{\hat{\epsilon}} = \frac{2}{m_0 \hbar \omega} \left| \langle \Psi_{\text{exc}} | \hat{\epsilon} \cdot \sum_i \mathbf{p}_i | \Psi_0 \rangle \right|^2 , \tag{1.13}$$

where $\hbar\omega = E_{\text{exc}} - E_0$ is the transition energy. For Wannier-Mott excitons and if the real-space envelope function is expressed in terms of the relative and centre-of-mass coordinates the oscillator strength reads

$$f_{\hat{\epsilon}} = \frac{2 |\hat{\epsilon} \cdot \mathbf{p}_{\text{cv}}|^2}{m_0 \hbar \omega} \left| \int \Psi(\mathbf{R}, \mathbf{r} = 0) d\mathbf{R} \right|^2 , \tag{1.14}$$

where $\mathbf{p}_{\text{cv}}$ is the interband momentum matrix element. Thus the exciton oscillator strength depends on the envelope function evaluated at zero electron-hole separation. In the case of free excitons in bulk semiconductors, the exciton wavevector $\mathbf{K}$ is conserved, and the envelope wavefunction takes the form $\Psi(\mathbf{r}, \mathbf{R}) = e^{i\mathbf{K}\cdot\mathbf{R}}\phi(\mathbf{r})$ yielding for the oscillator strength the result

$$f_{\hat{\epsilon}} = g \frac{2 |\hat{\epsilon} \cdot \mathbf{p}_{\text{cv}}|^2}{m_0 \hbar \omega} V |\phi_n(0)|^2 \delta_{\mathbf{K},0} , \tag{1.15}$$

where g is a spin-orbit factor taking into account the spin (singlet) component of the exciton state. As the exciton centre-of-mass wavefunction extends over the whole crystal the dimensionless exciton oscillator strength is proportional to the crystal volume V and therefore the meaningful quantity is the oscillator strength per unit volume, $f_{\hat{\epsilon}}/V$.

If the polariton effect is neglected, the oscillator strength per unit volume is related

to the absorption coefficient $\alpha(\omega)$ integrated over the absorption peak through:

$$\int \alpha(\omega)\mathrm{d}\omega = \frac{2\pi^2 e^2}{n m_0 c} \frac{f}{V}. \tag{1.16}$$

In quantum wells the relaxation of momentum conservation along the growth direction influences considerably the exciton oscillator strength as it is discussed in the following Section.

1.3 QUANTUM WELL EXCITONS

The quantum confinement of a particle in one direction results in quantisation of its momentum and energy along this direction while its motion in the other two dimensions remains unaffected. This effect becomes prominent when confinement becomes comparable with the de Broglie wavelength of the particle. A typical case where this kind of confinement takes place is a quantum well. When a thin layer of semiconductor is embedded in thick layers of a different semiconducting material with larger band-gap, a discontinuity between band edges appears and the particle's wavefunction is restricted within the quantum well with small probability to tunnel through the barrier. Due to reduced dimensionality a splitting of the valence band states occurs and one has to distinguish between light and heavy-hole excitons [11].

In a quantum well the confinement potential leads to quantisation of the electron and hole motion along the growth direction (which usually is taken to coincide with the z-direction) and the resulting energy levels, called *subbands*, have a two-dimensional dispersion $E_n(\mathbf{k}_\parallel)$ as a function of the in-plane wavevector $\mathbf{k}_\parallel$. This situation can be described by the Hamiltonian

$$H = E_{\mathrm{g}} - \frac{\hbar^2 \nabla_e^2}{2m_e} - \frac{\hbar^2 \nabla_h^2}{2m_h} + V_e(z_e) + V_h(z_h) - \frac{e^2}{\varepsilon_b |\mathbf{r}_e - \mathbf{r}_h|}, \tag{1.17}$$

where $V_e(z_e)$, $V_h(z_h)$ are the square-well confining potentials for electrons and holes, respectively, and E_{g} is the band-gap of the well material.

A direct consequence of exciton confinement is an increase in its binding energy compared to the bulk value. This is due to the removal of one degree of freedom in the kinetic energy which tends to separate the electron and hole while the potential

energy – responsible for the bound state – remains unchanged. As a result, the excitonic states inside a quantum well are more stable than in bulk materials and there is an enhancement in the optical effects. In the ideal two-dimensional limit of vanishing well width and infinite barrier height the exciton dispersion is given by

$$E_n = E_{\mathrm{g}} + \frac{\hbar^2 k^2}{2M_{\mathrm{x}}} - \frac{Ry^*}{(n - 1/2)^2}.$$ (1.18)

Thus the binding energy of the ground state exciton in a quantum well is $4Ry^*$ and its effective Bohr radius is $a_0/2$, *i.e.*, the exciton is more tightly bound. The binding energy increases monotonically with decreasing well width from the bulk value Ry^* to the 2D value $4Ry^*$ [12, 13]. However, this is true only for the case of an ideal QW, as in a realistic (finite) band offset the carriers' wavefunctions have always a finite probability to tunnel into the barrier material and, as a consequence, the binding energy reaches a maximum and then decreases towards the bulk value when the well width goes to zero [14].

The breaking of translational symmetry along the growth direction of a QW, results in relaxation of momentum conservation in this direction and only the in-plane wavevector $k_{\|}$ is still conserved. Accordingly, the real-space envelope function describing the exciton wavefunction is factorised as $\Psi(\mathbf{r}_{\mathrm{e}}, \mathbf{r}_{\mathrm{h}}) = e^{i k_{\|} \cdot \mathbf{R}_{\|}} \Psi(r, z_{\mathrm{e}}, z_{\mathrm{h}})$, where $\mathbf{r}$ and $\mathbf{R}_{\|}$) are the in-plane relative and centre-of-mass coordinates, respectively. Therefore, in this case the oscillator strength of QW excitons per unit area S is given by

$$\frac{f_{\hat{\epsilon}}}{S} = g \frac{2|\hat{\epsilon} \cdot \mathbf{p}_{\mathrm{cv}}|^2}{m_0 \hbar \omega} \left| \int \Psi(\mathbf{r} = 0, z) dz \right|^2.$$ (1.19)

(a) No applied electric field.   (b) Electric field applied perpendic-
                                        ular to the QW plane.
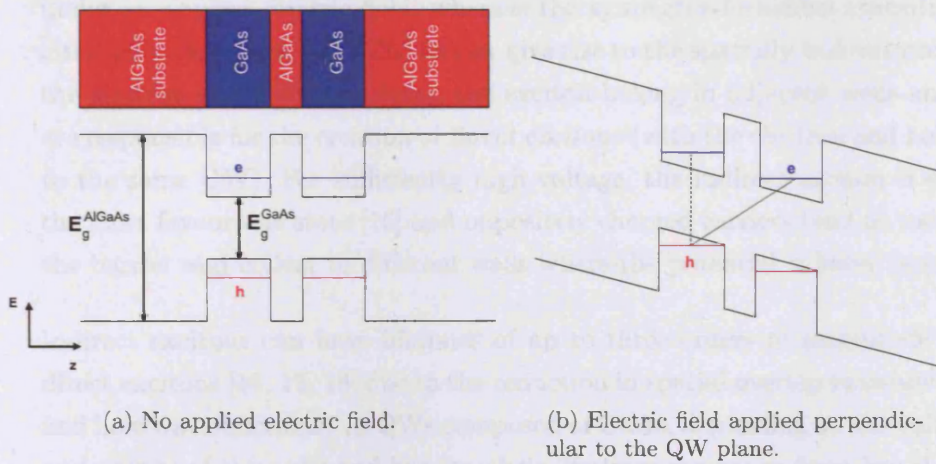
Figure 1.2: Energy band diagrams of a coupled quantum well structure. The indirect
exciton transition is shown by the green solid line in (b) where the electron and hole
are located in adjacent wells. The direct transition is depicted by the green dashed
line.

INDIRECT EXCITONS

When a strong electric field is applied in a bulk semiconductor the optical absorption
near the band edge is hugely modified, a phenomenon known as the Franz-Keldysh
effect. This effect is even more pronounced in the case of electrons and holes confined
in a QW. An electric field in excess of 10^5 kV/cm can be applied in the growth
direction of a QW either by embedding it in the active region of a p-i-n or n-i-n
junction or directly via a Schottky barrier. The consequent modifications of the
optical properties can be traced back to the change of the spatial confinement of the
electron and hole wavefunctions. In particular, there is a shift in the absorption edge
also known as the quantum confined Stark effect.

In the case of double quantum wells separated by a thin barrier the degenerate single
QW well states give rise to superpositions of symmetric or antisymmetric states. The
transitions between these levels in the flat-band condition are essentially determined
by parity symmetry since in the absence of an electric field the coupled states posses
definite parity under reflection in the z-direction. However, when a perpendicular
electric field is applied, the carrier wavefunctions are distorted and, as a result, the
selection rules are relaxed and all transitions become dipole allowed. In particular, the
symmetry allowed transitions in the flat-band condition become inter-well transitions

under an applied electric field, whereas the symmetry-forbidden transitions become intra-well transitions [15]. The former give rise to the spatially *indirect excitons* where the electron and hole comprising the exciton belong in adjacent wells and the latter are responsible for the creation of *direct excitons* (with the electron and hole belonging to the same QW). For sufficiently high voltage, the indirect exciton is energetically the most favourable state [16] and oppositely charged carriers tend to tunnel through the barrier and collect to different wells where the potential is lower (see Fig. 1.2).

Indirect excitons can have lifetimes of up to three orders of magnitude larger than direct excitons [15, 17, 18] due to the reduction in spatial overlap between the electron and hole wavefunctions. In QWs composed of GaAs, depending on the voltage applied and widths of the wells and barrier, their lifetimes can range from less than 1 ns to a few μs. The energy of the indirect exciton changes with the applied voltage, V_g, as the energy difference between the electron and hole changes. Above a critical value of the voltage, the indirect exciton energy line in experiments shifts almost linearly toward lower energies as the applied voltage increases [19].

Indirect excitons have an intrinsic dipole moment as they are dipoles oriented perpendicular to the QW plane. The dipole-dipole repulsion between them, stabilises the exciton gas against the formation of electron-hole droplets. The shift in exciton energy with increasing density, observed in experiments, offers a good estimate for the exciton concentration by means of the plate capacitor formula for the interaction between dipoles $n_{2D} = \varepsilon_b \delta E/(4\pi e^2 d)$, with d being the separation between electron and hole layers. A more formal approach is presented in Chapter 4 where the spatial coherence of excitons is discussed. It is shown there that the first-order spatial coherence is limited due to the dipole-dipole repulsion.

1.4   Phase Transitions of Excitons

The appearance of coherence in an exciton system can be either spontaneous or driven by a coherent pump source. In the former case the system reaches a quasi-equilibrium with a well-defined temperature and chemical potential while in the latter the coherence of the laser photons is preserved in the excited electronic states by means of the electron-hole pairing. When excitons can reach a quasi-equilibrium within their lifetime the possibility of Bose-Einstein condensation arises where a macroscopic number of excitons occupy the same quantum state. This means that the electronic state of

the crystal will have a definite polarisation and phase [20] and its luminescence will
be coherent. If we treat excitons as ideal bosons it follows from elementary statistical
mechanics [21] that the distribution number of particles is

$$N_{\mathbf{k}} = \frac{1}{e^{\beta(E_{\mathbf{k}} - \mu_{3D})} - 1} , \tag{1.20}$$

where μ_{3D} is the chemical potential measured from the bottom of the exciton band,
$\beta = 1/k_B T$ and $E_{\mathbf{k}} = \hbar^2 k^2 / 2 M_x$ denotes the single particles energies. The condition
which defines the chemical potential in thermal equilibrium is that the total number
of particles in the system be equal to the sum of the occupation numbers of the
single-particle states, namely

$$N = g \sum_{\mathbf{k}} N_{\mathbf{k}} , \tag{1.21}$$

where g accounts for spin multiplicity. If the spacing between the particle states is
assumed to be small one can replace the sum in Eq. (1.21) by an integral as long as
the density of states is taken into account

$$N/g = \int_0^\infty \rho(E) \, N_E \, dE . \tag{1.22}$$

For an ideal non-interacting 3D system the density of states has the form $\rho(E) \propto E^{1/2}$
and the integral in Eq. (1.22) approaches a finite value as μ_{3D} tends to zero. This
implies for the chemical potential an upper bound of zero for the distribution function
to remain well-defined at all energies. Consequently, a critical concentration exists
above which no more particles can be added to the excited states and any additional
particles must then *condense* into the state with $E = 0$.

The critical temperature for exciton BEC at fixed density is given by [22]

$$T_c = 3.31 \frac{\hbar^2}{M_x k_B} \left(\frac{n_{3D}}{g} \right)^{2/3} , \tag{1.23}$$

where $n_{3D} = N/V$ is the concentration of bulk excitons. For typical exciton con-
centration of $n_{3D} \sim 10^{17} \mathrm{cm}^{-3}$ and mass M_x of the order of the electron mass (*e.g.*
excitons in Cu_2O) one finds $T_c \sim 1\mathrm{K}$. Deviations of the distribution function of ex-
citons from a Maxwell-Boltzmann form will only occur at a density where their de
Broglie wavelength $\lambda_T = \sqrt{2\pi\hbar^2/(M_x k_B T)}$ becomes comparable with the interpar-
ticle spacing. As indicated by Eqs. (1.9)–(1.11) if the excitonic density reaches too
high a value the constituent Fermi nature becomes manifest and a phase-space filling

occurs. The resulting phase transition is an electron-hole liquid (EHL). If there exist attractive interactions between excitons, binding to excitonic molecules (biexcitons) may occur and these coexist with the exciton gas [23]. However, this is not the case for indirect excitons in coupled quantum wells as the overall repulsive interaction prevents the formation of such complexes and stabilises the exciton state. Even in the absence of attractive interactions a phase transition from the insulating exciton gas to a conducting electron-hole plasma (EHP) can take place when the high density of free carriers screens the Coulomb attraction and the bound states dissociate (*ionisation catastrophe*). The reverse transition from an EHP to an insulating phase is called *Mott transition* and occurs when the screening length in the plasma becomes larger than the excitonic Bohr radius. In this thesis the concentration of excitons is always considered to be low enough so that we can consider them as structureless bosons neglecting their underlying Fermi nature. Therefore, the only phase transition that may occur is that of BEC and its features are addressed in detail in the next subsection.

BEC OF EXCITONS

Although the phenomenon of BEC was proposed in the early twenties [24, 25] its observation for weakly-interacting bosons was made feasible only in recent years in alkali atoms [26, 27]. For this to be possible an advanced evaporative cooling technique had to be developed in magnetic traps, where high energy particles are removed leaving only well thermalised atoms inside the trap [27, 28]. By means of this technique extremely low temperatures of μK or even nK became accessible, and the creation of Bose-Einstein condensates is nowdays routinely achieved in various atomic systems [29-33].

The possibility of BEC in a solid state system has been predicted theoretically in the early sixties [34, 35] and excitons appeared to be the most suitable candidates for the appearance of spontaneous coherence, due to their extremely small translational mass which would allow a high temperature BEC. This assumption was thoroughly investigated in the seminal work of Keldysh and Kozlov [36] where they have shown that in the low density limit the exciton gas indeed exhibits bosonic behaviour and thus should undergo a phase transition into a condensate. This prediction generated a substantial amount of experimental efforts in order to observe BEC in excitonic systems.

Initially the research was focused on bulk semiconductors and mainly excitons in cuprous oxide (Cu_2O) were considered [37-49]. The reason that this system appeared particularly appealing was a very low radiative recombination rate of excitons due to its optically-inactive ground state. However, a high rate of non-radiative Auger processes at high excitation levels prevented the creation of dense and thermalised exciton gases as they reduce the exciton density and heat the system [44, 50, 51].

Another promising system for exciton BEC is that of indirect excitons in coupled quantum wells. Their long lifetime and high cooling rates renders them unique candidates for establishment of thermal equilibrium before recombination occurs. Moreover, the dipole-dipole repulsion prevents the formation of electron-hole droplets. The quasi-two-dimensional nature of indirect excitons may appear as an obstacle towards this goal. Indeed for a 2D system the density of states is constant and the integral in Eq. (1.22) is infinite as the chemical potential approaches zero. Thus there is no finite temperature below which the ground state mode can accommodate a macroscopically large number of particles. This situation holds for systems which contain infinite number of particles N and have infinite size S but with a finite value for the ratio N/S, i.e., in the thermodynamic limit. However, all systems have a finite size and contain a large — but not infinite — number of particles. As a result BEC is possible in finite 2D systems as long as a large fraction of particles occupy the state with $E = 0$ [52]. For this to be possible the separation between exciton energy levels should be small and the need for confinement in a trapping potential arises.

Bagnato et al. [53], have shown that 2D systems display BEC in a potential trap of the form $U(x) \sim x^\kappa$ for any finite value of $\kappa < 2$. BEC in low-dimensional systems with a finite number of particles has also been considered [54], and the corrections due to the finite particle number were proven to be small. The kinetics of indirect excitons in a trapping potential is studied in Chapter 3 and the time needed for the creation of degenerate exciton gas in the centre of the trap is found to be shorter than their lifetime.

Let us note here that another possibility for the appearance of a superfluid phase in 2D systems is that of Berezinskii-Kosterlitz-Thouless (BKT) transition [55, 56] where the correlations between particles at long distances exhibit a power-law decay. In all cases considered throughout this thesis either the temperature for a fixed density is too high or the density at a given temperature is too low for such a transition to take place.

In the case of a two-dimensional gas of non-interacting bosons the chemical potential is given by [21]

$$\mu_{2D} = k_B T \ln(1 - e^{-T_0/T}).$$ (1.24)

with the transition boundary from classical to quantum statistics defined by the degeneracy temperature T_0

$$T_0 = \frac{2\pi}{g} \frac{\hbar^2}{k_B M_x} n_{2D}.$$ (1.25)

In this case the equilibrium Bose-Einstein distribution can be rewritten as

$$N_{E_k} = \frac{1 - e^{-T_0/T}}{e^{E_k/k_B T} + e^{-T_0/T} - 1},$$ (1.26)

and therefore the occupation number of the ground state is

$$N_{E=0} = e^{T_0/T} - 1.$$ (1.27)

Equation (1.27) provides a convenient expression for determining the occupancy of excitons in the ground state mode in terms of the quantum degeneracy temperature which is density-dependent and therefore can be externally adjusted by the intensity of the laser excitation.

1.5   EXCITON CREATION

Excitons can form either by absorption of energy below the bandgap E_g or by creation of free electron-hole pairs which then relax by phonon emission and give rise to bound excitonic states. The former case is referred to as *resonant* creation whereas the latter as *non-resonant* creation. In this thesis only excitons created non-resonantly are treated as in all cases the laser excitation generates a significant amount of free e-h pairs with energies well above the bandgap. This is not the case in resonant exciton creation [57] where after the generation of direct excitons the carriers tunnel through the barrier to the energetically more favourable states of indirect excitons.

When excitons are created non-resonantly their excess energy E_i exceeds the energy splitting between the direct and indirect excitons, which is about 20 meV. The formation of an exciton from a free electron and a free hole at high temperatures takes place on a few ps time scale by longitudinal optical (LO) phonon emission while at temperatures below $E_i/k_B \sim 200$ K, longitudinal acoustic (LA) phonon emission is

the most important relaxation mechanism [58]. In the literature there is a wide spread
of the exciton formation time mainly due to the sensitivity in particular experimental
conditions. In GaAs/AlGaAs QWs structures the formation time varies from a few
tens of ps at high carrier concentrations [59–62] to several hundreds of ps when the
carrier concentration is low [58, 63–66]. The influence of temperature was also found
to be important on the exciton formation time, as at low temperatures excitons tend
to form faster [67].

The scattering of excitons by LA-phonons is described in the following Section as the
main mechanism towards the exciton thermalisation.

1.6   THERMALISATION OF INDIRECT EXCITONS

The creation of high energy electron-hole pairs through absorption of excess energy,
typically via optical excitation, is followed by fast carrier relaxation, exciton formation
and eventually recombination giving rise to the observed photoluminescence. Excitons
are formed rapidly 10 ps after the generation of free carriers and thermalise through
exciton-exciton, exciton-phonon and exciton-free carrier scattering in the order of 100
ps. At low temperatures the exciton–LA-phonon scattering dominates the cooling
process giving a characteristic sub-nanosecond relaxation time. However, since the
LO-phonons have a fixed energy ($\hbar\omega_{LO} = 36\,\mathrm{meV}$ in GaAs) they only participate in
the cooling of high energy excitons.

Excitons with energy below $M_x v_S^2/2$ (where M_x is the exciton mass and v_S is the
sound velocity in the crystal) cannot emit a phonon to relax down in energy while
conserving both energy and momentum. The physical reason for this, is that below
this value the loss of energy of the exciton reducing its momentum by an infinitesimal
amount, does not suffice to create a phonon with positive momentum. In other words,
when $\hbar^2 K^2/2M_x < M_x v_S^2/2$ the group velocity of excitons is less than that of phonons.
For the same reason excitons with energy close to zero can only absorb phonons with
energy greater than or equal to $2M_x v_S^2$.

For a two-dimensional system of bosons above the condensation temperature, ther-
mal equilibrium is reached within a few scattering times as thermodynamic critical
slowing down occurs, i.e., the relaxation time becomes longer as the temperature is
lowered. This indicates that a Boltzmann kinetic equation can be used to describe the

relaxation of two-dimensional excitons interacting with a three-dimensional acoustic phonon bath: since all microscopic degrees of freedom are involved at any given time, an arbitrary distribution evolves to a quasi-equilibrium state within a timescale given by the scattering time. The state with energy $E = 0$ couples to a continuum of states with $E \geq E_0 = 2M_x v_S^2$ rather than to E_0 only.

The phonon-assisted thermalisation kinetics of QW excitons is described in terms of relaxational thermodynamics [68, 69] and is used to study how Bose-Einstein statistics affect the thermalisation and photoluminescence of quasi-2D excitons. This approach assumes a hierarchy of interactions: exciton–exciton scattering has to be much stronger than the scattering of excitons with LA-phonons. The concentration of excitons, n_{2D}, should exceed some critical value for the system to be able to establish a quasi-equilibrium temperature, T, and the thermalisation of the excitons occurs through a series of quasi-equilibrium thermodynamic states. For GaAs QWs, this critical concentration is $n_{2D}^c \sim 1\text{-}3 \times 10^9 \,\text{cm}^{-2}$ [68].

In this Section the thermalisation of excitons in a QW at low densities interacting only via LA-phonon emission or absorption is analysed by means of a Boltzmann-Uhlenbeck or Quantum Boltzmann Equation (QBE). Under the assumption of in-plane momentum conservation the QBE reads

$$
\begin{aligned}
\frac{\partial}{\partial t} N_{k_\parallel} &= -\frac{2\pi}{\hbar} \sum_q |v(q)|^2 \left\{ \left[N_{k_\parallel}(1 + n_q^{\text{ph}})(1 + N_{k_\parallel - q_\parallel}) - (1 + N_{k_\parallel})n_q^{\text{ph}} N_{k_\parallel - q_\parallel} \right] \right. \\
&\quad \times \delta(E_{k_\parallel} - E_{k_\parallel - q_\parallel} - \hbar q v_S) + \left[N_{k_\parallel} n_q^{\text{ph}}(1 + N_{k_\parallel + q_\parallel}) \right. \\
&\quad \left. \left. - (1 + N_{k_\parallel})(1 + n_q^{\text{ph}}) N_{k_\parallel + q_\parallel} \right] \delta(E_{k_\parallel} - E_{k_\parallel + q_\parallel} + \hbar q v_S) \right\},
\end{aligned}
\tag{1.28}
$$

where $N_{k_\parallel}$ and n_q^{ph} are the occupation numbers of exciton in-plane mode $k_\parallel$ and phonon bulk mode $q = \{q_\parallel, q_z\}$, respectively, and $q_\parallel$ is the in-plane projection of q. The phonon energy is given by $E_{\text{ph}} = \hbar q v_S$. The terms in the first and second square brackets on the right-hand-side of Eq. (1.28) describe Stokes and anti-Stokes scattering processes, respectively, from mode $k_\parallel$. The matrix element is given by [70]

$$
v(q) = \sqrt{\frac{\hbar q}{2\rho v_S V}} \, D \, F_z\left(\frac{q_z L_z}{2}\right),
\tag{1.29}
$$

where D is the deformation potential, v_S is the phonon velocity in the crystal, ρ is the crystal density, V is the volume and L_z is the thickness of a quantum well. For

an infinitely deep, square quantum well, the form factor is [71]

$$F_z(x) = \frac{\sin x}{x} \frac{e^{ix}}{1 - \frac{x^2}{\pi^2}},$$ (1.30)

and describes the relaxation of momentum conservation in the z-direction. It is assumed that the quantum well width, L_z, is so small that only the ground state of the well needs to be considered, and therefore Eq. (1.30) refers to the ground state only.

Using Eq. (1.28) we can derive an equation which provides a unified description of the thermalisation process and will be used in calculations of the exciton effective temperature throughout this thesis. Allowing only excitons in the ground state with zero in-plane wavevector, $\boldsymbol{k}_{\|} = 0$, the QBE takes the form

$$
\begin{aligned}
\frac{\partial}{\partial t} N_{\boldsymbol{k}_{\|}=0} &= \frac{2\pi}{\hbar} \sum_{\boldsymbol{q}} |v(q)|^2 \left[N_{\boldsymbol{k}_{\|}=0} n_q^{\mathrm{ph}} (1 + N_{\boldsymbol{q}_{\|}}) - (1 + N_{\boldsymbol{k}_{\|}=0})(1 + n_q^{\mathrm{ph}}) N_{\boldsymbol{q}_{\|}} \right] \\
&\quad \times \delta(\hbar q v_{\mathrm{S}} - E_{\boldsymbol{k}_{\|}+\boldsymbol{q}_{\|}}) \\
&= -\frac{2\pi}{\hbar} \frac{\hbar q}{2\rho v_{\mathrm{S}} V} D^2 \sum_{\boldsymbol{q}} \left| F_z\left(\frac{q_z L_z}{2} \right) \right|^2 \\
&\quad \times \left[N_{\boldsymbol{k}_{\|}=0} n_q^{\mathrm{ph}} (1 + N_{\boldsymbol{q}_{\|}}) - (1 + N_{\boldsymbol{k}_{\|}=0})(1 + n_q^{\mathrm{ph}}) N_{\boldsymbol{q}_{\|}} \right] \delta(\hbar q v_{\mathrm{S}} - E_{\boldsymbol{k}_{\|}+\boldsymbol{q}_{\|}}).
\end{aligned}
$$ (1.31)

A transformation to the energy basis is straightforward [72, 73] and yields

$$\frac{\partial}{\partial t} N_{\varepsilon_k=0} = \frac{2\pi}{\tau_{\mathrm{sc}}} \int_1^\infty \mathrm{d}\varepsilon \; \varepsilon \sqrt{\frac{\varepsilon}{\varepsilon-1}} \; F_z^2 \left(a\sqrt{\varepsilon(\varepsilon-1)} \right) [N_\varepsilon(1+n_\varepsilon) - N_{\varepsilon_k=0}(n_\varepsilon - N_\varepsilon)],$$ (1.32)

where $n_\varepsilon \equiv n_E = n_q^{\mathrm{ph}}$, $N_\varepsilon \equiv N_E = N_{\boldsymbol{q}_{\|}}$ and $N_{\varepsilon_k=0} \equiv N_{E_k=0} = N_{\boldsymbol{k}_{\|}=0}$ in terms of the dimensionless energies of a phonon $\varepsilon = E/E_0$ and an exciton $\varepsilon_k = E_k/E_0$. Here, the distribution of the phonons is given by the Planck formula:

$$n_\varepsilon^{\mathrm{ph}} = \frac{1}{e^{\varepsilon E_0/k_{\mathrm{B}} T_{\mathrm{b}}} - 1}.$$ (1.33)

The scattering time τ_{sc} is defined as

$$\tau_{\mathrm{sc}} = \frac{\pi^2 \hbar^4 \rho}{D^2 M_{\mathrm{x}}^3 v_{\mathrm{S}}},$$ (1.34)

and typical values for GaAs QWs as described in Section 1.11 are: $\tau_{\mathrm{sc}} = 215\,\mathrm{ns}$ (for

$D = 6.5\,\text{eV}$), $\tau_{\text{sc}} = 98\,\text{ns}$ (for $D = 9.6\,\text{eV}$) and $\tau_{\text{sc}} = 38\,\text{ns}$ (for $D = 15.5\,\text{eV}$). The dimensionless constant a is given by

$$a = \frac{L_z M_x v_{\text{S}}}{\hbar}, \qquad (1.35)$$

and $a = 0.055$ if $M_x = 0.215 m_0$ and $L_z = 8\,\text{nm}$.

When $\varepsilon_k = 0$, the occupation number is given by $N_{\varepsilon_k=0} = e^{T_0/T} - 1$ (Eq. 1.27) and direct differentiation with respect to time yields

$$\frac{\partial}{\partial t} T = -\frac{T^2}{T_0} e^{-T_0/T} \frac{\partial}{\partial t} N_{\varepsilon_k=0}, \qquad (1.36)$$

or by substitution of Eq. (1.32)

$$\begin{aligned}
\frac{\partial}{\partial t} T &= -\frac{2\pi}{\tau_{\text{sc}}} \left(\frac{T^2}{T_0}\right)(1 - e^{-T_0/T}) \int_1^\infty d\varepsilon\, \varepsilon \sqrt{\frac{\varepsilon}{\varepsilon - 1}}\, \left| F_z\left(a\sqrt{\varepsilon(\varepsilon - 1)}\right)\right|^2 \\
&\quad \times \left(\frac{e^{\varepsilon E_0/k_B T_b} - e^{\varepsilon E_0/k_B T}}{e^{\varepsilon E_0/k_B T} + e^{-T_0/T} - 1}\right) \left(\frac{1}{e^{\varepsilon E_0/k_B T_b} - 1}\right).
\end{aligned} \qquad (1.37)$$

This equation describes how the – initially hot – excitons, thermalise via phonon emission from their initial temperature $T_i = T(t = 0)$ to the temperature of the lattice, T_b. Let us note that although our treatment was restricted to the case of thermalisation of a bosonic gas of particles, similar treatment yields a corresponding expression for the cooling process of fermions. However, the different statistics influences dramatically the effective temperature as the Pauli blocking does not allow the fermionic gas to reach the lattice temperature as fast as in the case of bosons. This will be discussed in detail in Chapter 2.

1.7 EXCITON PHOTOLUMINESCENCE

Excitons in quantum wells can only emit light from the low-energy states lying inside the photon cone due to breaking of the translational invariance of the QW and the corresponding relaxation of momentum conservation along the growth direction [74–77]. Figure 1.3 depicts the exciton and photon dispersion relations where it is shown that the *radiative zone* of quantum well excitons is defined as $k_\parallel \leq k_\gamma = (\sqrt{\varepsilon_b}/c)\omega_0$, *i.e.*, refers to excitons with centre-of-mass in-plane wavevector less than the crossover

of the photon and exciton dispersions. Here, $\hbar\omega_0$ is the photon energy, ε_b the background dielectric constant and c is the speed of light. The total radiative decay of a gas of quasi-equilibrium BE distributed QW excitons is [68]

$$\Gamma_{\text{opt}} = \frac{1}{\tau_{\text{opt}}} = \frac{\Gamma_0}{2} \frac{E_\gamma}{k_B T_0} \int_0^1 \frac{(1 + z^2)\mathrm{d}z}{A e^{-z^2 E_\gamma / k_B T} - 1}, \tag{1.38}$$

where A is given by

$$A = e^{E_\gamma / k_B T} / (1 - e^{-T_0/T}), \tag{1.39}$$

and $E_\gamma = \hbar^2 k_\gamma^2 / 2 M_x$. For GaAs QWs with $M_x = 0.215\, m_0$, $E_\gamma \simeq 141\,\mu\text{eV}$.
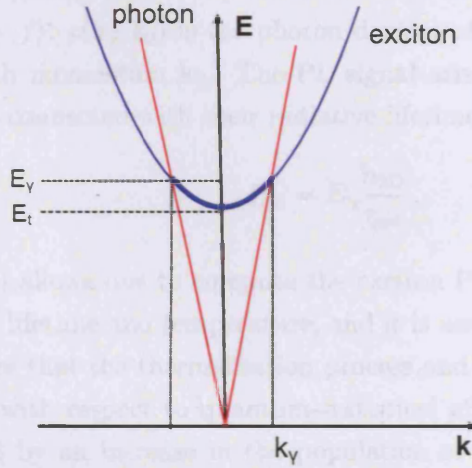
Figure 1.3: A plot of the photon and exciton dispersion relations, represented by the red and blue lines, respectively. The bold part of the exciton dispersion line shows the radiative zone of QW excitons. The crossover between photon and exciton dispersions occurs at k_γ which corresponds to an energy E_γ very close to E_t the exciton energy at $k = 0$. Hence, only the low-energy excitonic states contribute to the emitted PL signal.

The radiative rate $\Gamma_0 = \Gamma_T(k_\parallel = 0) = \Gamma_L(k_\parallel = 0)$ for the ground state mode $k_\parallel = 0$ determines the intrinsic radiative lifetime τ_R of QW excitons, which is $\tau_R = 1/\Gamma_0$. The subscripts L and T correspond to transverse (T-polarised) and longitudinal (L-polarised) dipole-active QW excitons, respectively. The optical decay time of highly-degenerate QW excitons is given by $\tau_{\text{opt}}(T \to 0) = 2\tau_R$ [68], since half of the excitons are dipole-inactive. A more detailed analysis of excitons' radiative lifetime is given in Section 4.4.1 where the issue of optical coherence is studied.

At low temperatures where $T_{\mathrm{b}} \ll E_{\gamma}/k_{\mathrm{B}}$, τ_{opt} saturates and approaches $2\tau_{\mathrm{R}}$ [3, 78, 79]. The radiative recombination of QW excitons affects the effective temperature of the system and therefore it is taken into account when thermalisation is discussed. For all practical purposes throughout this thesis we use $15 < \tau_{\mathrm{R}} < 60$ ns, in accordance with the applied voltage $1.2 < V_{\mathrm{g}} < 1.6$ V.

The intensity of the light emitted when excitons decay, *i.e.*, the photoluminescence intensity, can be calculated using Fermi's Golden Rule as,

$$I_{\mathrm{PL}}(\mathbf{k}_{\|}) \propto N_{\mathbf{k}_{\|}} \rho(\mathbf{k}_{\|}, k_0) \langle f | \mathbf{k}_{\|} \hat{\mathbf{p}} | i \rangle |^2, \tag{1.40}$$

where k_0 is the photon wavevector for a transition from an initial electronic state $|i\rangle$ to a final state $|f\rangle$, $\rho(\mathbf{k}_{\|}, k_0)$ is the photon density of states and $N_{\mathbf{k}_{\|}}$ is the number of excitons with momentum $\mathbf{k}_{\|}$. The PL signal arises from the radiative decay of excitons and is connected with their radiative lifetime via [68]

$$I_{\mathrm{PL}} = E_{\gamma} \frac{n_{\mathrm{2D}}}{\tau_{\mathrm{opt}}}. \tag{1.41}$$

Equation (1.41) allows one to compute the exciton PL intensity given their concentration, optical lifetime and temperature, and it is used in all numerical calculations. Let us note here that the thermalisation process and radiative decay, work in opposite directions with respect to quantum-statistical effects. Cooling of QW excitons is accompanied by an increase in the population of low-energy states while in the meantime τ_{opt} decreases and the optical decay accelerates, resulting in a decrease of T_0.

1.8   EXCITON TRANSPORT

In this thesis the expansion of the exciton gas in the QW plane is always assumed to be diffusive, due to high gradients in the concentration at the position of the laser excitation, and also affected by the local potential fluctuations which are either intrinsic or created by the dipole-dipole interactions between excitons. Starting from the semiclassical Boltzmann equation we shall thus eventually arrive at a macroscopic classical drift-diffusion equation. A generalisation of the drift-diffusion equation in the case of a quantum gas is straightforward as described in Appendix A. This relies on the idea that the quantum statistical effects can be incorporated in the relationship

between the mobility and the diffusion coefficient.

THE SEMICLASSICAL BOLTZMANN EQUATION

At a semiclassical level the kinetics of a system of particles under the influence of an external field $\mathbf{E}$ is governed by the Boltzmann transport equation for the particle distribution function $f(\mathbf{r}, \mathbf{k}, t)$

$$\frac{\partial f}{\partial t} + v_g f + \frac{1}{\hbar} \mathbf{E} \nabla_{\mathbf{k}} f = \left(\frac{\partial f}{\partial t} \right)_{\text{coll}}, \tag{1.42}$$

where $v_g = \hbar^{-1} \nabla_{\mathbf{k}} \varepsilon_k$ is the group velocity. The collision integral $(\partial f / \partial t)_{\text{coll}}$ includes in principle all scattering processes such as phonon, impurity, particle-particle scattering, generation and recombination processes. The Boltzmann equation relies on the assumptions that: (i) the distribution function varies little over the de Broglie wavelength, (ii) the carrier density is sufficiently low that only binary collisions occur, (iii) the time between successive collisions is much longer than the duration of a collision and (iv) the density gradients over the range of the interparticle potential are small.

HYDRODYNAMIC BALANCE EQUATIONS

At the hydrodynamic level of description the detailed kinetics in momentum space is averaged-over and only slow macroscopic quantities such as the carrier density

$$n(\mathbf{r}, t) = \int f(\mathbf{r}, \mathbf{k}, t) d\mathbf{k}, \tag{1.43}$$

the mean momentum per particle

$$p(\mathbf{r}, t) = \langle \hbar \mathbf{k} \rangle, \tag{1.44}$$

and the mean energy per particle

$$u_n(\mathbf{r}, t) = \langle \varepsilon(\mathbf{k}) \rangle, \tag{1.45}$$

are considered as dynamic variables. Here, the brackets denote the semiclassical ensemble average

$$\langle A \rangle = n^{-1} \int A(\mathbf{k}) f(\mathbf{r}, \mathbf{k}, t) d\mathbf{k} \,. \tag{1.46}$$

The resulting hydrodynamic balance equations have the form of continuity equations for the particle, mean momentum and energy density and can be obtained by multiplying the Boltzmann equation (1.42) by appropriate powers of $\mathbf{k}$ and integrating over the first Brillouin zone. If one neglects spatial variations in energy, one obtains the following closed set of hydrodynamic equations

$$\frac{\partial n}{\partial t} + \nabla (n\mathbf{v}) = \varphi(n, u_n) \,, \tag{1.47}$$

$$\frac{\partial \mathbf{p}}{\partial t} + (\mathbf{v}\nabla)\mathbf{p} - \mathbf{E} = -\frac{\mathbf{p}}{\tau_{\mathrm{m}}} \,, \tag{1.48}$$

$$\frac{\partial u_n}{\partial t} + (\mathbf{v}\nabla)u_n - \mathbf{v}\mathbf{E} = -\frac{u_n - u_0}{\tau_{\mathrm{e}}} \,, \tag{1.49}$$

where τ_{e} and τ_{m} are the energy and momentum relaxation time, respectively, $u_0 = (3/2)k_{\mathrm{B}}T$ and $\mathbf{v}$ is the mean group velocity.

CLASSICAL DRIFT-DIFFUSION THEORY

If momentum and energy relaxation occur faster than all other processes, $\mathbf{p}$ and u_n can be eliminated adiabatically and the particle densities remain as the only dynamic variables on this slow time scale. Transport may then be described within classical drift-diffusion theory. In this case the above set of hydrodynamic equations reduces to the usual drift-diffusion equation for the current density

$$\mathbf{j} = n \, \mu_{\mathrm{x}} \, \mathbf{E} + D_{\mathrm{x}} \nabla \, n \,. \tag{1.50}$$

Equation (1.50) if combined with the continuity equation

$$\frac{\partial n}{\partial t} + \nabla \mathbf{j} = 0 \,, \tag{1.51}$$

yields a drift-diffusion equation for the particle transport along the QW plane

$$\frac{\partial n}{\partial t} = \nabla \left[D_{\mathrm{x}} \nabla n + \mu_{\mathrm{x}} \, n \nabla U \right] \,, \tag{1.52}$$

where U denotes the total potential created by the external field and the variations in the QW width. This equation in its quantum generalised form is used throughout this thesis to model both free and bound carrier transport as described in detail in the next two Chapters. Apart from the assumptions for the use of Boltzmann equation, which all hold in the case of indirect excitons in QWs, there exist many references in the literature which justify the diffusive character of exciton transport. These are briefly discussed in the following subsection.

DIFFUSION OF EXCITONS IN QUANTUM WELLS

The diffusivity of *electrons* in QWs has been studied extensively the last two decades [80–84], and in recent years, so has the diffusivity of QW *excitons* [85–93]. Most of the experiments have dealt with the determination of the diffusion coefficient which would allow for accurate knowledge of the excitons' transport properties. However, the variety of results reported implies that exciton diffusion in QWs depends strongly on the experimental conditions and in particular on the temperature, the excitation power and the quality of the studied samples. At temperatures $2.5 < T < 15K$ a diffusion coefficient as low as $D_x \sim 4\,cm^2/s$ has been reported [85], while time-resolved imaging in multiple quantum wells (MQWs) has revealed a variation in effective diffusivity from ~ 50 to $300\,cm^2/s$ initially to less than $100\,cm^2/s$ after $4\,ns$ [86] and was attributed to the high carrier temperature generated by large excess energies. In different studies in GaAs/AlGaAs MQWs the diffusion coefficient was found to be in the range of $1\,cm^2/s \lesssim D_x \lesssim 15\,cm^2/s$ for a concentration of $n_{2D} \sim 10^{10}\,cm^{-2}$ and lattice temperature, $T_b = 5\,K$ [94]. Recently, measurements of the diffusion coefficient of *indirect excitons* in CQW structures were performed, by using time-resolved optical imaging [92] and it was shown that the excitons experienced a strong "pressure" due to dipole-dipole repulsive interaction, which caused a drift motion. The distribution of the excitons at different times after the excitation pulse, allowed for determining the variance of the distribution at each stage. In order to observe only the motion in the diffusive regime, the variance at long time delays was used, to measure the diffusion coefficient. For well widths of $8\,nm$ and an applied electric field of $7\,V/\mu m$ the diffusion constant was found to be $D_x \sim 0.25\,cm^2/s$. A different model including drift and diffusion effects has been proposed by Ivanov to explain the transport of dipole-oriented QW excitons in CQWs [95].

1.9 QUANTUM WELL DISORDER

In quantum wells there is an intrinsic built-in potential due to variations in the barrier thickness and alloy fluctuations. This *interface roughness* also referred to as *QW disorder* influences both the optical and transport properties of excitons. The effects of disorder in QWs has been studied both experimentally and theoretically [81, 82, 91, 96–102].

The observation of a PL peak on the low-energy side of the heavy hole free exciton in InGaAs/GaAs QWs at low temperatures, was attributed to an exciton bound to potential fluctuations due to QW disorder [96, 97]. Interface roughness was reported to be the dominant scattering mechanism for electrons [81] as well as for excitons [98] in thin QWs with well thickness $L_z < 6\,\mathrm{nm}$, where electron mobilities $\propto L^6$.

In time-of-flight studies a diffusion coefficient of $D_x \sim 15\,\mathrm{cm^2/s}$ was obtained for direct excitons in an 8 nm-thick QW, with $T = 64\,\mathrm{K}$ and optical lifetime $\tau_{\mathrm{opt}} \sim 2.35\,\mathrm{ns}$ [99]. Low-temperature mobilities were found to be mainly determined by interface roughness scattering. This was also confirmed in Ref. [100], where it was shown that in a typical QW sample in which the excitonic diffusion is limited by interface roughness, the diffusivity increases exponentially with increasing QW width.

Recently it was proven that at relatively high concentrations, indirect excitons in CQWs can effectively screen the disorder potential, due to their dipole-dipole repulsive interaction [95]. Excitons tend to fill the local minima of the intrinsic potential and avoid its maxima, flattening in this way the potential relief of the QW. This screening of long-range correlated disorder results in an increase of the diffusion coefficient.

1.10 EXPERIMENTS

As there is at present huge scientific interest in the properties of indirect excitons in coupled quantum wells, many experiments are conducted by different research groups. For the purposes of this thesis whenever our theoretical results are compared with experimental data the structure described in detail in Ref. [103] is used. In this Section the main features of this structure are discussed and the numerical values of the parameters used in the simulations are given.

EXPERIMENTAL DETAILS

In most of the experiments simulated in this thesis, electron-hole pairs are created in quantum wells under applied electric field by illumination of a tightly focused laser and subsequently form indirect excitons in timescales of ps. The lattice is kept at helium temperatures ($\sim 1\,\mathrm{K}$) whereas the photogenerated free or bound carriers are initially hot ($\sim 200\,\mathrm{K}$). After their creation excitons and free electron-hole pairs move in the quantum well plane due to drift and diffusion forces produced by particle interaction and gradients in the concentration, respectively, while at the same time cool down via LA-phonon emission. The thermalised excitons eventually recombine and emit light which is collected by a CCD camera.

The experiments being conducted are either time-resolved which study the evolution of the exciton gas after the source is switched off or spatially-resolved where the transport of excitons away from the excitation spot is studied under continuous excitation. In the case of excitons confined by an external field the evolution of the system both in time and space is of interest, a situation which is described in detail in Chapter 3. Regardless the design of each particular experiment the main quantities measured are the intensity and energy of the PL signal. In the experiments discussed in this thesis the PL signal is collected only from a small angle α from the z-axis to ensure that only low-energy excitons are detected. However, as we shall see in Chapter 4 this fact has dramatic consequences when coherence effects are studied.

Since indirect excitons are aligned dipoles, at high densities they repel each other via dipole-dipole interaction which causes a blue-shift in the energy of the exciton. For a wide range of concentrations ($10^9 < n_{2\mathrm{D}} < 10^{12}\,\mathrm{cm}^{-2}$) the blue-shift was measured to be proportional to the concentration [104] a fact predicted by analytical calculations as well [105]. In the experiments by Butov *et al.* [106] a plate capacitor formula was used to infer the concentration from the shift of the exciton line. This rough estimation proved to be sufficient for the explanation of most of the experimental results. However, when coherence effects are considered, a more formal approach is in order as we discuss in Section 4.3.

1.11   SAMPLE STRUCTURE AND RELEVANT
PARAMETERS

The GaAs/AlGaAs CQW sample studied in experiments consists of two 8 nm GaAs
wells separated by a 4 nm $Al_{0.33}Ga_{0.67}As$ barrier with an overall n^+–i–n^+ structure.
The active region is embedded in layers of $Al_{0.33}Ga_{0.67}As$, 200 nm thick surrounded
by heavily n-doped GaAs electrode layers which have an excess number of electrons
$\sim 5 \times 10^{17}$ cm^{-3}. These top and bottom layers are 105 and 305 nm thick, respectively.
An Au/Pd/Ge alloy was deposited on these layers to form ohmic contacts. Under the
bottom layer there is a 20 nm superlattice (AlAs/GaAs), a much thicker buffer layer
(800 nm) and a substrate layer (GaAs). Forward bias is defined as electron flow from
the bottom contact through the wells and the barriers to the top contact. Figure 1.4
depicts a cartoon of the processed mesa.
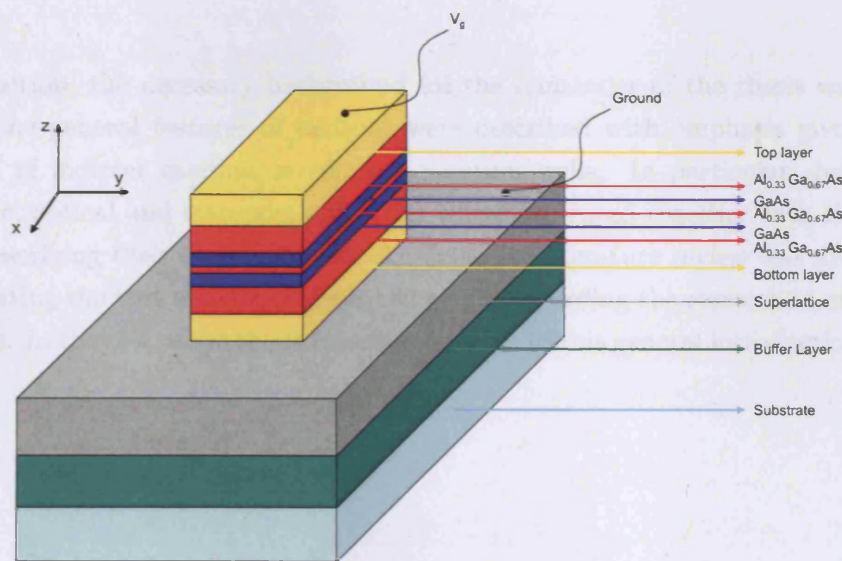
Figure 1.4: A schematic diagram of the structure. The active region of the quantum
well is shown by the alternating GaAs (blue) and AlGaAs (red) layers embedded
between the n-doped (yellow) electrode layers.

Below we enlist the most important numerical parameters used throughout this thesis
as they are deduced from the experiments or calculated in the literature.

The well width is $L_z = 8$ nm and the distance between the electron and hole layers

is $d_z = 11.5\,\text{nm}$ [95, 103] slightly different from $12\,\text{nm}$, the distance between the QW centres. The effective mass of indirect excitons, using a parabolic band approximation, is $M_x = 0.215\,m_0$ [95, 107] where m_0 is the free electron mass and the spin degeneracy factor is $g = 4$ [68]. The radiative lifetime of ground state excitons τ_R depends on the applied voltage in the z-direction and lies in the range of $6.75\,\text{ns} < \tau_R < 31.50\,\text{ns}$.

Regarding the deformation potential, D, there is a wide range of values in the literature, from ~ 6.5 to $15.5\,\text{eV}$ [70, 108, 109]. In all numerical calculations throughout this thesis a value of $D = 6.5\,\text{eV}$ was used. The dielectric constant for GaAs is $\varepsilon_b = 12.9$ [110] and the crystal density $\rho = 5.3\,\text{g/cm}^3$ [111, 112]. The velocity of sound in the crystal is $v_S = 3.7 \times 10^5\,\text{cm/s}$ [113] corresponding to $E_0/k_B = 2M_x v_S^2 = 0.38$ K.

1.12 SUMMARY

In this introduction, the necessary background for the remainder of the thesis was established. The general features of excitons were described with emphasis given on the system of indirect excitons in coupled quantum wells. In particular their thermodynamic, optical and transport properties where presented together with the basic model describing their thermalisation. An extensive literature review was also provided indicating the vast amount of published results regarding the research in excitonic systems. In the rest of the thesis several references to this general introduction are made.

2 EXCITON RINGS FORMATION

One of the most common situations in experiments is that where a laser beam creates free electron-hole pairs in a semiconductor heterostructure which bind very rapidly to form excitons. As the pumping is continuous, at every moment all three species – namely electrons, holes and excitons – are present and they can move in the quantum well plane. In this Chapter the exciton formation and transport is described in the presence of an electron-hole plasma. In particular, the appearance of photoluminescence (PL) rings around quantum well localities is identified with the binding of electrons and holes in the interface of two regions where each species is dominant. The study is performed by means of two coupled drift-diffusion equations for the in-plane carrier transport, a Poisson equation for the charge accumulated in the coupled QWs and a thermalisation equation for electrically- and photo-injected carriers.

2.1 EXPERIMENTAL OBSERVATIONS: PL PATTERNS

When a semiconductor structure is illuminated by a laser, valence band electrons absorb the photons from the laser beam and are promoted either to the free conduction band states or form excitons after binding with the holes in the valence band. In experiments a tightly focused laser with a Gaussian intensity profile induces the interband transitions in a quantum well creating free and bound electron-hole pairs. After their creation excitons, electrons and holes move along the QW plane and are scattered with each other and by the lattice vibrations, *i.e.*, phonons, reducing their energy and therefore their effective temperature. Since the study of exciton transport is of major importance in this kind of experiments, the external parameters can be

tuned so as to minimise the effect of free carriers.

In three recent works [1, 114, 115] astonishing PL patterns were reported in macro-
scopically large distance away from a cylindrically symmetric excitation spot. In
particular, for the series of experiments reported in Ref. [1], the PL spectra exhibit
two concentric annular rings separated by a dark region with randomly distributed
bright localised spots. The inner ring is small with a radius of approximately 30 μm
while the external ring can be very large in size with a radius exceeding 100 μm. Al-
though in Ref. [114] only the external ring is reported, its radius could be as large as
500 μm and its existence was verified even in experiments with single quantum wells
where only direct excitons exist [116].
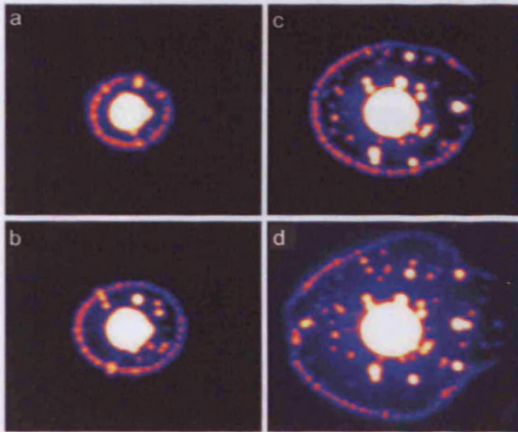
Figure 2.1: Spatial patterns of the indi-
rect exciton PL intensity with increas-
ing excitation power. The colour rep-
resents the intensity of the PL signal
with white corresponding to the maxi-
mum PL signal then yellow, red, pur-
ple and blue represent decreasing inten-
sities and black represents no PL signal.
The experimental parameters are: lattice
temperature, T_b = 1.8 K, gate voltage,
V_g = 1.22 V, and the excitation powers,
P_{ex}, (a) 290 μW, (b) 390 μW, (c) 690 μW
and (d) 1030 μW. The area of view is
530 × 440 μm. Taken from Ref. [1].

As can be seen in Fig. (2.1) the most striking feature of the external ring is its frag-
mentation in a periodic array of beads of high PL intensity when the temperature is
lowered. This low temperature phenomenon was initially attributed to the appear-
ance of spontaneous coherence but it was later explained as a symmetry breaking
instability similar to a Turing instability in reaction-diffusion systems [117]. Despite
the fact that the repulsive interaction between indirect excitons is against any spon-
taneous pattern formation, in the proposed model an increase in the stimulated e-h
binding rate due to local fluctuation in exciton density, causes neighbouring carriers
to stream towards the point of the fluctuation providing a mechanism of positive feed-
back [118]. In a different approach, it is suggested that the attractive Van der Waals
interaction between indirect excitons dominates over the dipole-dipole repulsion at
short distances and condensed phases of excitonic islands emerge, similar to the for-
mation of electron-hole droplets in bulk semiconductors [119–121]. However, taking
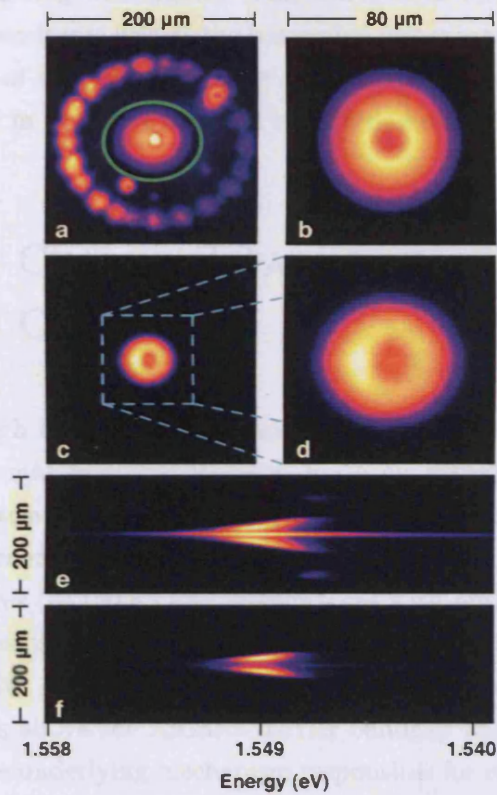
Figure 2.2: PL patterns of the indirect excitons in the $x - y$ plane, as seen in the experiment [(a), (c) and (d)], and calculated by the theoretical model [(b)]. The PL signal is imaged in $E - x$ coordinates in (e) and (f). For high excitation power the external PL ring is also seen in (a) and (e). White represents the highest intensity, then yellow, red, purple and blue represent decreasing intensities and black represents no PL signal. The excitation powers used were: $P_{ex} = 250\,\mu W$ [(a) and (e)] and $75\,\mu W$ [(b), (c), (d) and (f)] and the bath temperature was $T_b = 1.5\,K$. Taken from Ref. [2].

into account that the appearance of fragmentation is very sensitive to the applied electric field and, according to electrical characterisation of the structure, coincides with the region of negative differential resistance (NDR) [3], one is led to assume that the positive feedback needed for pattern formation is provided by local accumulation of free carriers.

The observation of the inner PL ring was possible due to advanced experimental techniques, used to remove the low energy bulk emission which otherwise would dominate the spectrum near to the excitation spot. Excitons are created non-resonantly and close to the optically-pumped area their temperature ($\sim 5\,K$) exceeds that of the lattice (~ 1–$2\,K$) and, as a result, their optical decay is suppressed. As they travel away from the excitation spot they cool down due to phonon emission and become optically active giving rise to a local increase of the PL signal [2]. The internal ring is therefore a generic feature of PL from excitons, direct or indirect, that are excited non-resonantly in high quality QWs [72]. Note that in these studies, subbarrier excitation was used and therefore no excess free carriers were photogenerated and the

external ring was absent. This was a clear indication that although the inner ring was of excitonic origin, the outermost was created due to free carrier imbalance. This idea is of crucial importance towards the understanding of the localised PL centres studied in this Chapter, and we will describe it in detail in the next Section.

2.2   CHARGE SEPARATION OF A 2D ELECTRON-HOLE GAS

Although early interpretations of the external ring related its appearance with the long sought excitonic BEC, it was soon realised that it was unlikely that excitons would travel in such large distances within their lifetime and thus they must have been generated at the ring position. Moreover, its persistence up to very high temperatures (~ 100 K) and in structures with only short-lived direct excitons excluded any possibility of exciton transport from the excitation spot to the position of the ring [122, 123]. The observation that the external ring formed only when photo-excitation energies above the AlGaAs barrier bandgap energy were used, led to the conclusion that the underlying mechanism responsible for its formation was an optically-induced in-plane separation of oppositely charged plasmas [116, 124-128].

It is well known that in modulation doped structures, optical excitation with energy above the barrier can lead to depletion of electrons [129]. An off-resonance laser excitation violates the overall charge neutrality in the sample due to the different collection efficiency in the QW between electrons and holes [130]. In the absence of any photoexcitation a 2D electron gas is present in the QW originating from the modulation doping of the sample, and its density depends on the leakage current. Illumination by a laser results in the creation of hot electrons and holes which are consequently trapped in the QW. However, since the heavier holes have much smaller drift velocity [110] and shorter phonon scattering time [131] than the electrons, their trapping rate is larger and an excess of holes ends up trapped in the QW which recombine with the 2D electron gas and deplete it. Therefore, a hole-rich area forms in the vicinity of the excitation spot surrounded by an electron sea. The ambipolar diffusion of oppositely charged carriers forms a sharp boundary hundreds of micrometers away from the excitation spot. As a carrier crosses into a minority region, it binds rapidly with an opposite carrier to form an exciton creating a sharp luminescence ring between the hole-rich region and the outer electron-rich area. An increase in the

excitation power leads to a stronger depletion of electrons around the central spot and thus a larger number of holes which pushes further the boundary and increases the ring radius.

2.3 LOCALISED PL CENTRES

As mentioned above, inside the area defined by the external ring several randomly distributed PL centres (PLCs) appear, and their number increases with increasing applied voltage. Experiments with a defocused laser excitation where a large area was illuminated [3, 124] have revealed a novel striking effect: around the PLCs small rings appear which mirror the behaviour of the outer ring [3, 124]. However, the rings shrink with increasing excitation power, indicating that the electron-hole contrast in these localities is inverted: they constitute sources of hot electrons embedded in the hole-rich inner area.

These electron sources were identified with transverse current filaments crossing the QW structure. In these points an electrical breakdown occurs and the resulting filaments inject hot electrons in the QW plane. Accumulation of a dense electron gas has been reported around these filaments [132, 133] and formation of rings with radii of tens of micrometers was recorded. Unlike attractive trapping potentials, the current filaments create locally a very strong repulsive effective potential which acts as an *anti-trap* for indirect excitons. The PLCs are characterised by (i) a fixed in-plane position, (ii) an annular structure of the spatially resolved photoluminescence signal and (iii) a Gaussian shape of the blue shift of the PL line [3, 132, 133]. In this Chapter a theoretical model is developed in order to model the PLCs' features.

UNDERLYING PHYSICAL PICTURE

The PLCs originate from the current filaments crossing the coupled QWs [124, 128]. Thus, in the vicinity of these defects, charge accumulates as a part of electrons from the filament are captured in the wells and a repulsive potential for electrons and indirect excitons is created. The drift force resulting from this potential induces the in-plane electron transport away from the centre of the filament. However, the photogenerated holes undergo an attraction from the negatively charged area around the

filament and move towards it. As the holes encounter the outwards moving electrons they bind to form excitons which then decay and give rise to the PL signal. The repulsive potential around the filament acts as an *anti-trap* for the dense electron gas, as well as for the secondary created indirect excitons. Note that although trapping of excitons has already been studied in various works [134–139], the influence of an anti-trapping, repulsive potential has not been previously considered. Excitons around the filament are scarce, due to an effective heating by the transverse filament current, and only at a distance of approximately 10 μm from the PLCs an exciton cloud effectively forms. Far from this cloud the excitonic gas becomes dilute again, due to a small concentration of electrons. The local increase of the excitonic energy originates from the anti-trapping character of the in-plane potential around the filament.

2.4   TRANSPORT EQUATIONS OF THE ELECTRON-HOLE PLASMA

The above discussion dictates the development of a theoretical model to describe the formation of exciton rings around the current filaments. Several similar models have been applied to describe the formation of the external ring as a dynamic p-n junction [116, 124–128] in terms of coupled diffusion equations for the two different fermionic plasmas. However, in the vicinity of the source, an effective repulsive potential is created for electrons, as the negative charge builds up around it. The accumulation of charge results in in-plane diffusion and drift of the electrons. In our approach this repulsive potential is taken into account explicitly and this inclusion is proved to be crucial for the explanation of the experimental PL patterns. The electrically-induced charge, trapped by the coupled QWs, creates a potential U_{Coulomb} which influences the transport of carriers and the formation of excitons. The potential of accumulated electrons is determined by solving the 3D Poisson equation, and the bare input potential is modelled by $U_{\text{bare}} = \alpha_0/(r^2 + r_0^2)$, where α_0 and r_0 are free parameters which are inferred from the experiment. For numerical calculations we have used $\alpha_0 = 1.2$ meVμm^2 and $r_0 = 2$ μm. However, the overall repulsive character of the effective potential is not strongly affected by the bare potential, as shown in Fig. 2.3. The effective potential is the sum of these two contributions, $U_{\text{eff}} = U_{\text{bare}} + U_{\text{Coulomb}}$.
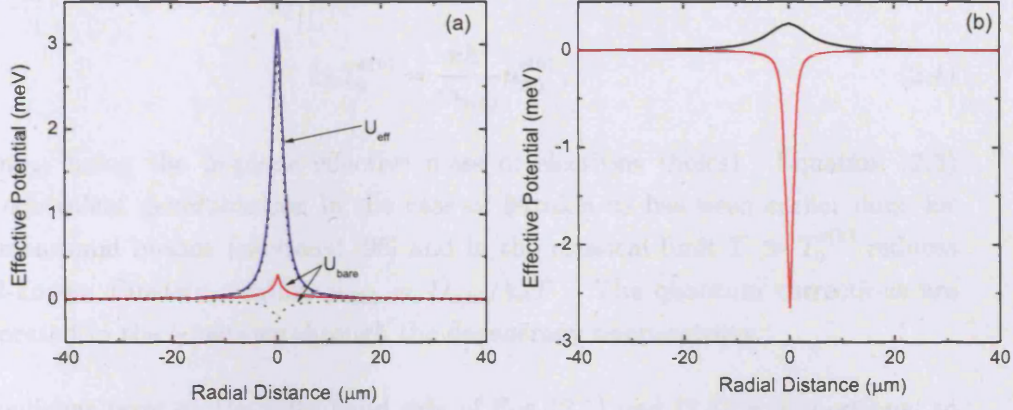
Figure 2.3: (a) The anti-trap profile is plotted as a function of the radial distance from the filament centre for repulsive (solid line) and attractive (dotted line) bare potentials. The corresponding bare potentials are also shown. The parameters used are $\alpha_0 = \pm 1.2$ meV μm^2 and $r_0 = 2$ μm. (b) In the presence of a very deep attractive bare potential (red line) the effective potential (black line) remains repulsive although it becomes less steep and broader. The parameters used for the bare potential are $\alpha_0 = -2.75$ meV μm^2 and $r_0 = 1$ μm.

Around the filament the electron density is high and steep gradients in the concentration exist. Under the influence of both drift and diffusion forces, the electronic gas expands in the QW plane. The system of coupled drift-diffusion equations for the oppositely charged free carriers reads [140]:

$$\frac{\partial n_{2D}^e}{\partial t} = \nabla_{2D} \left[D_e \nabla_{2D} n_{2D}^e + \mu_e n_{2D}^e \nabla_{2D} U_{eff}^e \right] - \gamma n_{2D}^e n_{2D}^h + \Lambda^e + \Lambda_0^e , \tag{2.1}$$

$$\frac{\partial n_{2D}^h}{\partial t} = \nabla_{2D} \left[D_h \nabla_{2D} n_{2D}^h + \mu_h n_{2D}^h \nabla U_{eff}^h \right] - \gamma n_{2D}^e n_{2D}^h + \Lambda^h , \tag{2.2}$$

where $\nabla_{2D} = e_x \partial/\partial x + e_y \partial/\partial y$ denotes the two-dimensional derivative. In Eqs. (2.1)–(2.2), $D_{e(h)}$ and $n_{2D}^{e(h)}$ are the diffusion coefficient and two-dimensional concentration of electrons (holes), respectively and are related with the corresponding mobilities via a generalised Einstein relation (see Appendix A)

$$\mu_{e(h)} = \frac{D_{e(h)}}{k_B T_0^{e(h)}} \left(1 - e^{-T_0^{e(h)}/T} \right) , \tag{2.3}$$

where T is the effective temperature of QW carriers calculated in Section 2.6, and

$T_0^{e(h)}$ is the electron (hole) degeneracy temperature defined by

$$k_B T_0^{e(h)} = \frac{\pi \hbar^2}{m_{e(h)}} n_{2D}^{e(h)} , \qquad (2.4)$$

with $m_{e(h)}$ being the in-plane effective mass of electrons (holes). Equation (2.3) is the equivalent generalisation in the case of fermion as has been earlier done for two-dimensional bosons (excitons) [95] and in the classical limit $T \gg T_0^{e(h)}$ reduces to well-known Einstein relation $\mu_{e(h)} = D_{e(h)}/k_B T$. The quantum corrections are incorporated in the equations through the degeneracy temperatures.

The nonlinear term on the right-hand side of Eqs. (2.1) and (2.2) is proportional to the product of the electron and hole concentrations and describes the radiative recombination of bound and unbound electron-hole pairs. The capture coefficient γ corresponds to a time of a few picoseconds and has been calculated within a microscopic approach (see Appendix B)

The effective potential that the carriers undergo is different for each species since electrons are dominant. Namely one has to solve the 3D Poisson equation

$$\nabla_{3D}^2 U_{\text{Coulomb}} = -\frac{e^2 n_{2D}^e}{\varepsilon_b} , \qquad (2.5)$$

where e is the free electron charge, ε_b the background dielectric constant and $\nabla_{3D} = \nabla_{2D} + e_z \partial/\partial z$ (the z-axis is normal to the structure). Note that although the transport is quasi-two-dimensional, the Poisson equation has to be solved in three dimensions as electrons outside the QW plane influence the in-plane potential. The resulting effective potential is the sum of two contributions for electrons

$$U_{\text{eff}}^e = U_{\text{bare}} + U_{\text{Coulomb}} , \qquad (2.6)$$

whereas for holes

$$U_{\text{eff}}^h = u_0 n_{2D}^e , \qquad (2.7)$$

and the amplitude of the dipole-dipole interaction u_0, can be well-approximated by $u_0 = 2\pi(e^2/\varepsilon_b)d$, with d the separation between the electron and hole layers [105].

The generation rates of electrons and holes, due to the optical pump, are given by Λ^h and Λ^e respectively, whereas the rate Λ_0^e refers to electrons from the filament which are captured in the wells. For numerical simulations we take $\Lambda^h = \Lambda^e$ and neglect

diffusion of holes since under a defocused excitation the photogenerated carriers are scarce.

Equations (2.1) and (2.2) together with (2.6) and (2.7) define the in-plane carrier transport and are solved numerically in order to model the experimental data. The only input fitting parameter used in numerical simulations is the carrier generation rate which is inferred from the electric current measurements [3]. Once the in-plane densities of free carriers are calculated, one is interested in determining the exciton concentration at the position of the rings. In order to achieve that, a quantum mass action law is introduced in the next Section.

2.5 QUANTUM MASS ACTION LAW

The system of electrons, holes and excitons is in equilibrium with each other and with the crystal lattice in all parameters apart from the total number of excitons and e-h pairs which is determined by the external excitation source. Nevertheless, since the exciton thermalisation time is much less than its lifetime the establishment of a quasi-equilibrium distribution function in the exciton band can be assumed. The coherent pairing of electrons and holes can be described on the basis of the e-h Hamiltonian:

$$
\begin{aligned}
H &= \sum_{\mathbf{k}}(\varepsilon_{\mathbf{k}}^e - \mu_e)a_{\mathbf{k},\sigma}^\dagger a_{\mathbf{k}} + \sum_{\mathbf{k}}(\varepsilon_{\mathbf{k}}^h - \mu_h)b_{\mathbf{k}}^\dagger b_{\mathbf{k}} \\
&+ \frac{1}{2V}\sum_{\mathbf{k},\mathbf{p},\mathbf{q}} v_{\mathbf{q}}[a_{\mathbf{k}}^\dagger a_{\mathbf{p}}^\dagger a_{\mathbf{p}+\mathbf{q}}a_{\mathbf{k}-\mathbf{q}} + b_{\mathbf{k}}^\dagger b_{\mathbf{p}}^\dagger b_{\mathbf{p}+\mathbf{q}}b_{\mathbf{k}-\mathbf{q}} \\
&- 2a_{\mathbf{k}}^\dagger b_{\mathbf{p}}^\dagger b_{\mathbf{k}+\mathbf{q}}a_{\mathbf{p}-\mathbf{q}}] ,
\end{aligned}
\tag{2.8}
$$

where $v_{\mathbf{q}}$ is the Fourier transform of the Coulomb interaction of an electron and a hole in a continuous medium with dielectric constant ε_{b}, given by

$$
v_{\mathbf{q}} = \frac{2\pi e^2}{\varepsilon_{\mathrm{b}}q} ,
\tag{2.9}
$$

and the Fermi operators $a_{\mathbf{k}}^\dagger, a_{\mathbf{k}}(b_{\mathbf{k}}^\dagger, b_{\mathbf{k}})$ describe the creation and annihilation of electrons (holes), respectively.

If enough electrons and holes are excited the Coulomb attraction between particles may be weakened, a phenomenon known as *screening*. The effect of screening on

an exciton has been considered in terms of a Stern-Howard potential [141] for the electron-hole interaction. Numerical calculations [142, 143] have shown that as the density of the electron-hole pairs — and therefore the screening — increases, the bound states of the Stern-Howard potential disappear. It is thus reasonable to assume that in the vicinity of a current filament electrons are the dominant particles and excitons form only far from it.

Considering the exciton concentration far away from the position of the rings to be low, the contribution of bound states to screening is small and the Coulomb interaction can be replaced by a potential which is statically screened due to the free charged particles [141, 144, 145]

$$v_{\mathbf{q}} = \frac{2\pi e^2}{\varepsilon_b} \frac{1}{q + q_s}, \qquad (2.10)$$

with the two-dimensional Debye screening parameter given by

$$q_s = \frac{2}{a_0\mu}[m_e(1 - e^{-T_0^e/T}) + m_h(1 - e^{-T_0^h/T})], \qquad (2.11)$$

where a_0 is the effective 2D exciton Bohr radius and μ the reduced mass. Moreover we consider all corrections due to the mean field interaction to be restricted to Pauli blocking and all fermions – free and bound – to contribute to the phase space occupation. The consequence of these two effects is that the exciton binding energy has to be renormalised in the presence of an electron-hole plasma. For our exploratory calculations the simplification of quasi-equilibrium distribution for all particles was used as the drift-diffusion equations were solved in steady state.

The number of electrons and holes in the corresponding bands is determined by the choice of the experimental conditions. Their quasi-equilibrium states can be characterised by introducing two different chemical potentials μ_e for electrons and μ_h for holes. Here, the energy and the chemical potential for the electrons are measured relative to the bottom of the conduction band and for the holes from the top of the valence band. In the case of thermodynamic equilibrium only one common chemical potential exists, and the chemical reaction

$$e + h \rightleftharpoons x, \qquad (2.12)$$
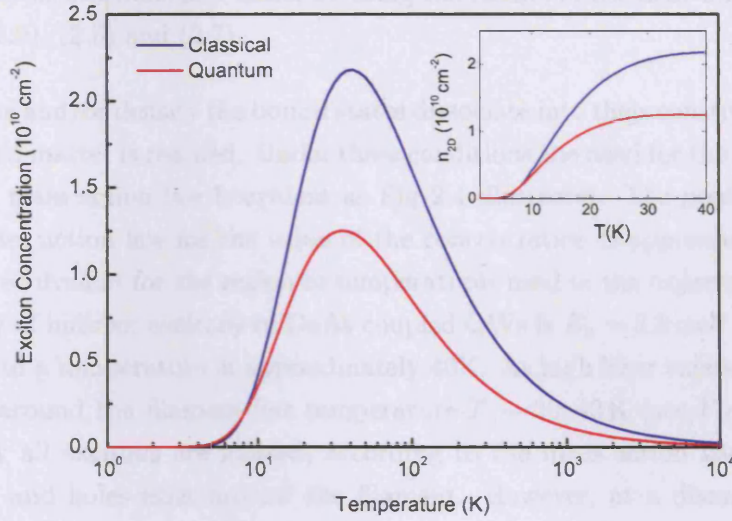
Figure 2.4: The concentration of excitons calculated with the quantum mass action law is compared with the corresponding classical expression as a function of temperature. Although the two curves coincide for extremely high or very low temperatures in the region relevant to the experiments the discrepancy is evident. Note the logarithmic scale in the temperature axis. Inset: The same plots shown in linear scales in the region of temperatures consistent with the experimental conditions. The quantum prediction is almost half of the corresponding classical.

implies a relation between the chemical potentials

$$\mu_x = \mu_e + \mu_h \ . \tag{2.13}$$

Direct substitution of the expressions for the two-dimensional chemical potentials yields a quantum mass action law for the excitonic concentration:

$$n_{2D}^x = \frac{4}{\lambda_T^2} \ln[e^{-E_b/k_B T}(e^{T_0^e/T} - 1)(e^{T_0^h/T} - 1)] \ , \tag{2.14}$$

where E_b is the exciton binding energy and $\lambda_T = [(2\pi\hbar^2)/(M_x k_B T)]^{1/2}$ is the thermal wavelength of excitons. In the classical limit, Eq. (2.14) reduces to the well-known Saha formula [145]:

$$n_{2D}^x = \frac{\lambda_T^2 M_x^2}{m_e m_h} \ n_{2D}^e \ n_{2D}^h \ e^{-E_b/k_B T} \ . \tag{2.15}$$

Equation (2.14) describes the coexistence of free carriers and excitons and allows us to calculate the concentration of excitons, which are secondary particles originating

from the binding of free electrons and holes, by using the results of the drift-diffusion model, Eqs. (2.1),(2.2), (2.6) and (2.7).

At high temperature and/or density the bound states dissociate into their constituents and a plasma state of matter is reached. Under these conditions the need for the quantum version of the mass action law is evident as Fig. 2.4 illustrates. The prediction of the quantum mass action law for the value of the concentration is approximately half of its classical equivalent for the region of temperatures used in the experiments. The binding energy of indirect excitons in GaAs coupled QWs is $E_b = 3.5\,\text{meV}$ [122], which corresponds to a temperature of approximately 40K. At high laser excitations, the electronic gas around the filament has temperature $T \sim 20\text{--}40\,\text{K}$ (see Fig. 2.6). In this case, nearly all excitons are ionised, according to the mass action law, and only free electrons and holes exist around the filament. However, at a distance of $10\,\mu\text{m}$ electrons reach the lattice temperature and an excitonic PL ring appears. The variation of temperature with the radial distance from the source centre is described in the following Section.

2.6 ELECTRON THERMALISATION

Electrically- or photo-injected QW carriers are hot and cool down to the lattice temperature via LA-phonon emission. Thermalisation of the particles injected in the coupled QWs is dominated by electrons, because around the filament $n_{2D}^e \gg n_{2D}^h, n_{2D}^x$. The underlying physical picture is that of relaxational thermodynamics [68] where the electron-electron scattering is assumed to be more efficient than the interaction of electrons with bulk LA-phonons. In this case, which refers to $n_{2D}^e \gtrsim 10^9 \text{cm}^{-2}$, the thermalisation occurs through the quasi-equilibrium thermodynamic states, characterised by an effective electron temperature T and concentration n_{2D}^e [69]. In our approach the confinement of phonons is neglected. This is a good approximation since the acoustic branches overlap in energy leading to phonon modes which are propagative throughout the structure and therefore bulk-like [70]. Similarly to the procedure described in Section 1.6, the starting point for the thermalisation equation

of electrons is the Boltzmann-Uhlenbeck equation:

$$
\frac{\partial}{\partial t} N_{\mathbf{k}} = -\frac{2\pi}{\hbar} \sum_{\mathbf{q}} |v_q|^2 \left\{ [N_{\mathbf{k}}^{e}(1 + n_{\mathbf{q}})(1 - N_{\mathbf{k-q}}^{e}) - (1 - N_{\mathbf{k}}^{e}) n_{\mathbf{q}} N_{\mathbf{k-q}}^{e}] \right.
$$
$$
\times \delta(E_{\mathbf{k}} - E_{\mathbf{k-q}} - \hbar q v_{\mathrm{s}}) + [N_{\mathbf{k}}^{e} n_{\mathbf{q}}(1 - N_{\mathbf{k+q}}^{e})
$$
$$
\left. -(1 - N_{\mathbf{k}}^{e})(1 + n_{\mathbf{q}}) N_{\mathbf{k+q}}^{e}] \times \delta(E_{\mathbf{k}} - E_{\mathbf{k+q}} + \hbar q v_{\mathrm{s}}) \right\} , \tag{2.16}
$$

where $N_{\mathbf{k}}^{e}$ and $n_{\mathbf{q}}$ are the occupation numbers of electrons and phonons, respectively, and v_{s} is the sound velocity associated with LA-phonons. Considering only electrons in the ground state mode $\mathbf{k} = 0$, Stokes scattering is not allowed and equation (2.16) reduces to:

$$
\frac{\partial}{\partial t} N_{\mathbf{k}=0} = \frac{2\pi}{\hbar} \sum_{\mathbf{q}} |v_q|^2 \left\{ [N_{\mathbf{q}}^{e}(1 - N_{\mathbf{k}=0}^{e})(1 + n_{\mathbf{q}}) - N_{\mathbf{k}=0}^{e} n_{\mathbf{q}}(1 - N_{\mathbf{q}}^{e})] \right.
$$
$$
\left. \times \delta(\hbar q v_{\mathrm{s}} - E_{\mathbf{k+q}}) \right\} , \tag{2.17}
$$

where the matrix element of the interaction is given by Eq. 1.29 also repeated here

$$
v_q \equiv v(q) = \sqrt{\frac{\hbar q}{2\rho v_{\mathrm{s}} V}} \, D_{\mathrm{dp}} F_z \left(\frac{q_z L_z}{2} \right) , \tag{2.18}
$$

D_{dp} is the deformation potential for electrons, ρ is the crystal density, and the form-factor was defined in Eq. 1.30.

For the ground state mode the occupation number is given by $N_{E=0}^{e} = 1 - e^{-T_0^{e}/T}$. The corresponding equation for the temperature evolution written in the energy basis reads

$$
\left(\frac{\partial T}{\partial t} \right)_{2D} = -\frac{2\pi}{\tau_{\mathrm{sc}}} \frac{T^2}{T_0^{e}} \left(e^{T_0^{e}/T} - 1 \right) \int_1^{\infty} d\varepsilon \varepsilon \sqrt{\frac{\varepsilon}{\varepsilon - 1}} |F_z(\alpha \sqrt{\varepsilon(\varepsilon - 1)})|^2
$$
$$
\times \left(\frac{e^{\varepsilon E_0/k_{\mathrm{B}} T_{\mathrm{b}}} - e^{\varepsilon E_0/k_{\mathrm{B}} T}}{e^{\varepsilon E_0/k_{\mathrm{B}} T_{\mathrm{b}}} + e^{T_0^{e}/T} - 1} \right) \left(\frac{1}{e^{\varepsilon E_0/k_{\mathrm{B}} T_{\mathrm{b}}} - 1} \right) + S_{\mathrm{pump}} , \tag{2.19}
$$

where $\tau_{\mathrm{sc}} = (\pi^2 \hbar^4 \rho / D_{\mathrm{dp}}^2 m_e^3 v_{\mathrm{s}})$ is the characteristic scattering time and $E_0 = 2 m_e v_{\mathrm{s}}^2$ is a characteristic thermalisation energy. Equation (2.19) describes thermalisation dynamics of electrons from the initial effective temperature $T_{\mathrm{i}} = T$ to the bath temperature T_{b}. The effective cooling of electrons in the presence of a bath of thermal bulk phonons is due to the relaxation of momentum conservation in the z-direction, which results in the coupling of the ground state mode $\mathbf{k} = 0$ to a continuum of states
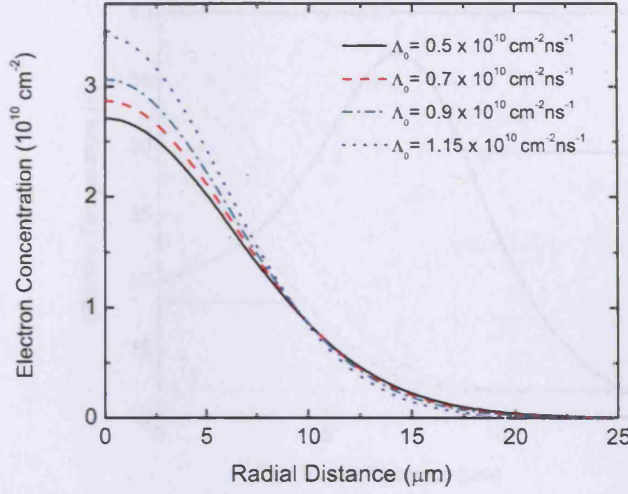
Figure 2.5: The concentration of electrons as a function of the radial distance from the filament centre for four different generation rates as indicated. Within a distance of $10\mu m$ all four curves coincide as the electrically injected carriers dominate over their photogenerated counterparts.

$E \geq E_0$ rather than the single energy state $E = E_0$ [68, 69]. Notice that in comparison with Eq. (1.37) apart from the different degeneracy temperature the prefactor $(e^{T_0^*/T} - 1)$ results in a slowing down of the thermalisation process, reflecting the fermionic nature of electrons. The extra term S_{pump} is added to include the heating of electrons by the current filament and laser pulse and is equal to

$$S_{\mathrm{pump}} = \frac{(E_{\mathrm{i}} - k_{\mathrm{B}}TI_2)\Lambda_{\mathrm{T}_0}}{2k_{\mathrm{B}}TI_1 - k_{\mathrm{B}}T_0I_2} \; , \tag{2.20}$$

where $I_1 = \int_0^\infty dz[z/(Ae^z + 1)]$, $I_2 = (e^{T_0^*/T})/(e^{T_0^*/T} - 1)^2 \int_0^\infty dz[(e^z z)/(Ae^z + 1)^2]$, and $A = 1/(e^{T_0^*/T} - 1)$. The generation rate of electrons is given by Λ_{T_0}, and their initial injected energy per particle is $E_{\mathrm{i}} = k_{\mathrm{B}}T_{\mathrm{i}}$. Figure 2.6 shows how electrons reach the lattice temperature at approximately $10\mu m$ away from the filament centre for three different generation rates Λ_0. The heating of the electron gas close to the filament increases with increasing generation rate. However, away from the heating source and as the temperature approaches the cryostat temperature of the lattice, the exciton concentration peaks, indicating the binding of electrically injected electrons with optically generated holes. These excitons constitute a gas of degenerate bosons which eventually recombine producing excitonic rings of photoluminescence. Utilisation of
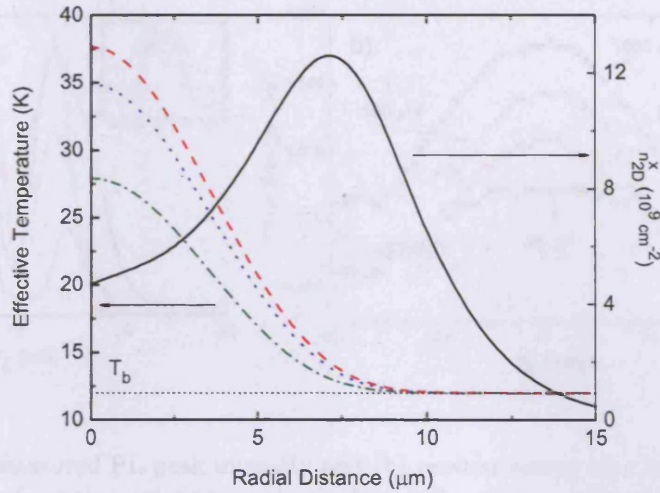
Figure 2.6: The effective temperature as a function of the radial distance from the anti-trap centre, for three different generation rates. The electronic gas is heated by the electric current and photo-current and reaches the bath temperature $12\,\mathrm{K}$ in a distance of about $10\,\mu\mathrm{m}$. The concentration of secondary excitons, n_{2D}^{x}, calculated with Eq. 2.14 is shown by the solid line for the highest generation rate. As the temperature drops with increasing $r_{\parallel}$, the exciton concentration reaches a maximum. The corresponding generation rates used in the simulations are $\Lambda_0 = 0.7, 0.9$ and $1.15 \times 10^{10}\,\mathrm{cm}^{-2}\ \mathrm{ns}^{-1}$ for the green, blue and red lines respectively.

the theoretical model described above allows one to compare in detail its predictions with the experiment and the results are presented in the next Section.

2.7   RESULTS AND COMPARISON WITH EXPERIMENTS

By applying the transport Eqs. (2.1)–(2.2) together with the quantum mass action law (2.14) and the thermalisation equation (2.19) the validity of the theoretical model was tested by direct comparison with the experimental data. In the experiments, a defocused uniform HeNe laser spot of diameter ~ 600–$700\ \mu\mathrm{m}$ was used and the spatially resolved photoluminescence from indirect excitons was collected [3]. According to the experimental data, the PL peak intensity profile exhibits a central dip surrounded by two maxima, indicating a ring structure for the exciton distribution. The ring appears at around $10\mu\mathrm{m}$ from the anti-trap centre, and the ring formation is not
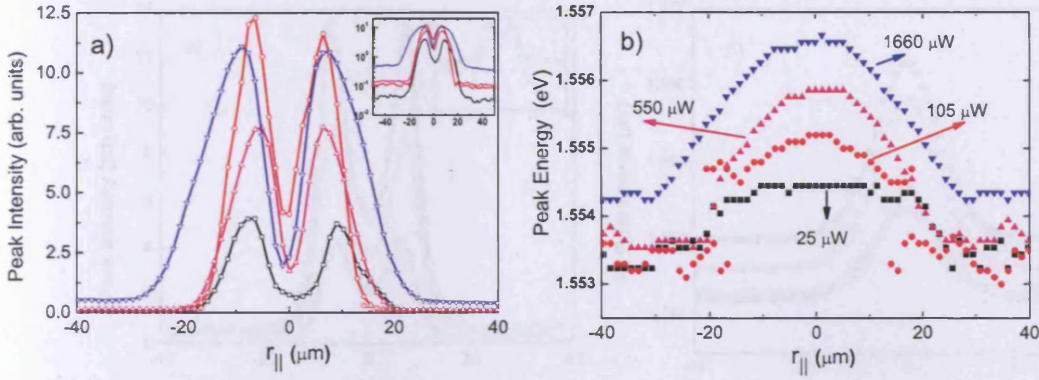
Figure 2.7: (a) The measured PL peak intensity and (b) exciton energy as a function of the radial distance from the anti-trap centre, for four different laser powers $P_{\text{laser}} = 25, 105, 550$ and 1660μW (solid, dashed, dotted and dash-dotted lines, respectively). In the inset of (a) the PL intensity is plotted in a logarithmic scale. A ring structure appears around the anti-trap center before the PL peak intensity reaches a background value. Taken from Ref. [3]

affected by the laser power. This is consistent with the theory which allows only well-thermalised electrons to form excitons and then recombine. The PL signal, which is attributed only to the ground-state excitons, is given by

$$I_{\text{PL}} = I_{\text{PL}}(r_{\|}) \sim N^{\text{x}}_{E=0} \frac{1}{\tau_{\text{R}}} \simeq \frac{T_0}{T} \frac{1}{\tau_{\text{R}}} \; , \tag{2.21}$$

where $N^{\text{x}}_{E=0} = e^{T_0/T} - 1$ is the occupation number of the ground-state mode, τ_{R} is the intrinsic radiative lifetime of indirect excitons and T_0 is the exciton degeneracy temperature. The concentration of excitons n^{x}_{2D}, calculated with the mass action law (2.14), is plotted in Fig. 2.6 against the in-plane radial distance $r_{\|}$. Because for $r_{\|} = 0$ the effective temperature $k_{\text{B}}T \sim E_{\text{b}}$, the excitons are partly ionized. This explains the non-monotonous behaviour of $n^{\text{x}}_{\text{2D}} = n^{\text{x}}_{\text{2D}}(r_{\|})$. In Fig. 2.8(b) the spatial profile $I_{\text{PL}} = I_{\text{PL}}(r_{\|})$ is shown. Away from the ring position the PL signal decreases towards a small background level which depends upon the concentration of photogenerated carriers.

The calculated energy shift δE_{x} of the PL line, depicted in Fig. 2.8(a) against the radial distance $r_{\|}$ for four different intensities of the laser beam, again reproduces quantitatively the experimental data of Fig. 2.7(a). The bell-like shape is due to the accumulation of electrons injected from the filament. The density of indirect
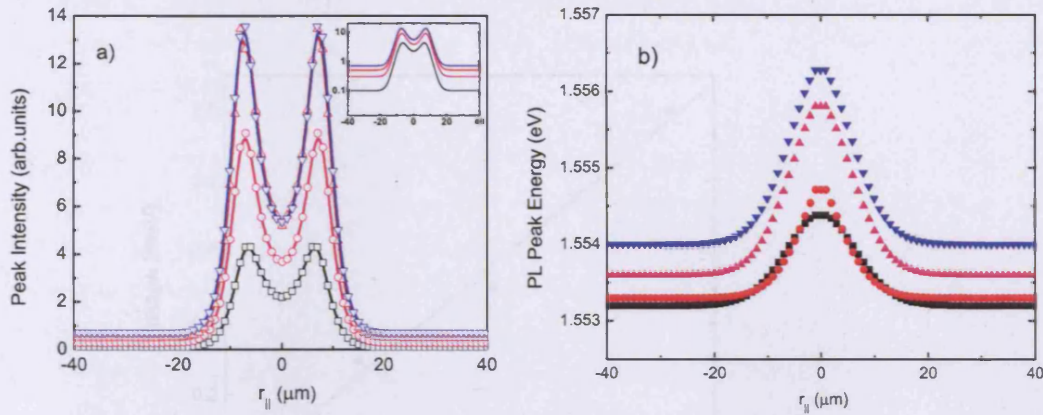
Figure 2.8: (a) The calculated PL peak intensity as a function of the radial distance from current filament centre for the same excitation powers as in Fig 2.7. Inset: The same plot in a logarithmic scale. (b) The calculated peak energy of excitonic photoluminescence as a function of the radial distance. The electron gas is hot near the anti-trap center and its energy becomes constant away from it. The blue shift of the PL line with increasing laser power is evident.

excitons can be estimated from the energy shift and vice versa by using the plate capacitor formula $\delta E_{\mathrm{x}} = 2\pi n_{\mathrm{2D}}^{\mathrm{e}} e^2 d / \varepsilon_{\mathrm{b}}$, where d is the separation between electron and hole layers. Thus, the blue shift of the PL peak energy follows the change of the electron density $n_{\mathrm{2D}}^{\mathrm{e}} = n_{\mathrm{2D}}^{\mathrm{e}}(r_\parallel)$ around the centre of the filament. Away from the PLC the energy profile drops to a constant value which is higher for higher excitation powers. This background shift was initially attributed to a homogeneous background carrier distribution created under the uniform optical excitation. However, this is not consistent with the experimental results which show a very low concentration not capable to produce such a large energy shift.

A possible explanation for such a behaviour can be given in terms of device physics, considering the actual potential drop across the structure as $U_{\mathrm{CQW}} = U_{\mathrm{Appl}} - RI$. Here, U_{Appl} is the applied voltage, $I = I_{\mathrm{dark}} + I_{\mathrm{pc}}$ is the total electric current across the structure (I_{dark} is the "dark" current and I_{pc} is the photocurrent), and R is the passive resistance of the whole electric circuit. With increasing optical intensity the photocurrent I_{pc} increases causing decrease of the actual potential drop U_{CQW}. The photoinduced change of U_{CQW} results in the change (blue shift) of the position of the energy E_{x}. Figure 2.9 shows the experimentally observed background shift $\delta E_{\mathrm{x}}^{(0)}$ [3]. The linear behaviour of $\delta E_{\mathrm{x}}^{(0)} = \delta U_{\mathrm{CQW}}$, which corresponds to Ohm's law
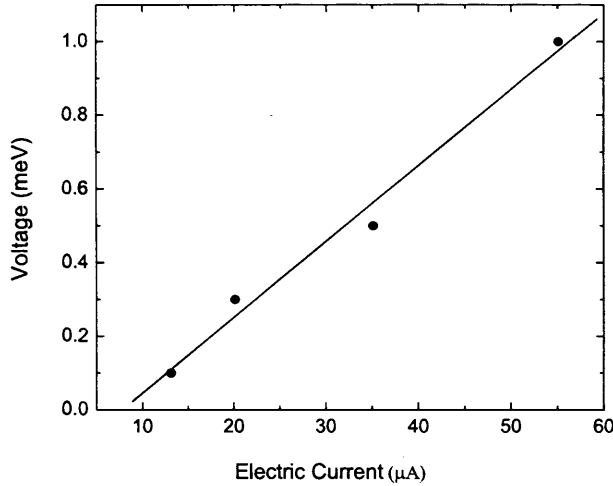
Figure 2.9: The voltage drop across the structure against the electric current. The blue shift scales linearly with the photocurrent as it is shown by the solid line which is a fit to the measured points. The effective Ohmic resistance, calculated as the gradient of the curve, is $R = 800\text{k}\Omega$ in agreement with the experimental observations.

with $R = 800\,\text{k}\Omega$, is clearly seen. Note that the inferred value of the resistance R is consistent with $R \sim 10^4 - 10^5\,\Omega$ measured in [3]. This linear dependence of the I-V characteristics excludes any nonlinear phenomena due to feedback current at the position of the PLCs. However, the external ring formation coincides with a region of NDR in the I-V curves, indicating a nonlinear effect which could provide the essential effective attractive interaction for the explanation of the ring fragmentation.

2.8 SUMMARY

In this Chapter we have studied the PL patterns of indirect excitons from localised centres in double quantum well structures. The localised bright spots were attributed to defects in the nanostructure, where transverse current filaments cross the wells. The repulsive potential created in the vicinity of these anti-traps affects the in-plane carrier transport, which is simulated through the drift-diffusion model of Eqs. (2.1), (2.2), (2.6) and (2.7). The charge density is calculated self-consistently using the

three-dimensional Poisson equation (2.5). After obtaining the electron and hole concentration one applies the quantum mass action law, Eq. (2.14), to calculate the exciton concentration.

The thermalisation kinetics is given by Eq. (2.19) and plays an important role in the explanation of the experimental data. The quantum-statistical corrections are included through the degeneracy temperatures. Application of this model to the experimental data reveals a quantitative agreement. In particular, the PL peak intensity exhibits a ring structure around the centre of the anti-trap while the energy position of the PL line reaches a maximum at $r_\parallel = 0$. However, both the PL peak energy and the PL intensity approach a constant value away from the anti-trap. The latter behaviour is attributed to the feedback current flowing through the QW structure.

3 DYNAMICS OF EXCITONS IN OPTICAL TRAPS

In this Chapter the kinetics of excitons in in-plane optical traps are studied and simulations consistent with the experimental observations are performed. Excitons are created in a ring through an annular excitation and move in the quantum well under drift and diffusion forces while at the same time cool down via LA-phonon emission. The kinetics of excitons is modelled in space and time through a drift-diffusion equation and a thermalisation equation for the effective temperature. It is shown that the characteristic timescales in the trap allow for the creation of a dense and cold exciton gas at its centre.

3.1 INTRODUCTION

Unlike a flux of atoms, excitons do not transport mass or charge but they do carry energy and momentum from one point of the lattice to another. An exciton after its creation is subject to forces inducing its motion and migrates to distant points where it eventually recombines and is detected through its photoluminescence (PL). Indirect excitons in quantum wells are very mobile and characterised by high values of diffusion coefficient and mobility. Therefore, the creation of an ensemble of quantum-degenerate excitons has been a real challenge for experimentalists over the past decades, mainly in connection with the appearance of Bose-Einstein condensation [79, 104, 114, 132, 146–148]. In order for this to be achieved excitons had to be confined in the quantum well plane.

TRAPPING OF INDIRECT EXCITONS

Several kinds of *traps* have been used during the last decades to confine excitons in two dimensions. Initially mechanical traps were created by pressing a pin against the QW structure creating in this way a harmonic potential where excitons accumulated [134, 149–151]. Electrostatic traps have also been considered [135, 152–154]. In one of these cases Rapaport *et al.* [152] applied a potential across a CQW with a small circular optically semitransparent gate where the bottom substrate was heavily doped so as to act as the ground electrode. Above a critical value of the electric field needed to overcome the dipole-dipole repulsion the excitons tended to collect in the region under the gate contact. However, the exciton concentration was limited by ionisation effects at the trap boundaries where the high electric field pulls the electron and hole apart, dissociating the excitons. This problem was overcome by Hammack *et al.* [135] by placing the CQW structure closer to the bottom gate minimising in this way the ionisation effects. The creation of a cold exciton gas in this case was achieved through an evaporative cooling technique as the most energetic particles escaped the trap and only quantum-degenerate excitons were collected.

Larionov *et al.* [19] created a lateral potential well by depositing a narrow strip of gold on the sample surface and observed accumulation of indirect excitons hundreds of micrometers away from the excitation spot. Formation of an excitonic condensate has also been predicted by Zhu *et al.* [155] in CQWs with specific variations in their widths. In fact intrinsic fluctuations of the random potential in QWs seemed to serve as natural traps for indirect excitons. Butov *et al.* [132] reported strong PL signal from such localities, a clear indication of collection of well-thermalised excitons. Localisation of indirect excitons in these potential minima has been proven to screen the QW disorder potential and create a flat landscape for the diffusion of excitons [95].

Early studies in a QW system with an interdigitated gate of small period have also shown exciton localisation [156] while another method for voltage-controlled exciton trapping was by means of lateral superlattices [157, 158]. The possibility of trapping via laser-induced interdiffusion [159] or magnetic fields [160] has also been reported.

Finally, a novel method applied was that of confinement by a laser. Such methods were developed in atomic systems [161–163] where micron-sized particles were trapped due to radiation pressure of a laser beam. Hammack *et al.* [136] have used these ideas

to trap excitons formed by an annular-shaped laser profile. In the following subsection we describe in detail the principles optical trapping.
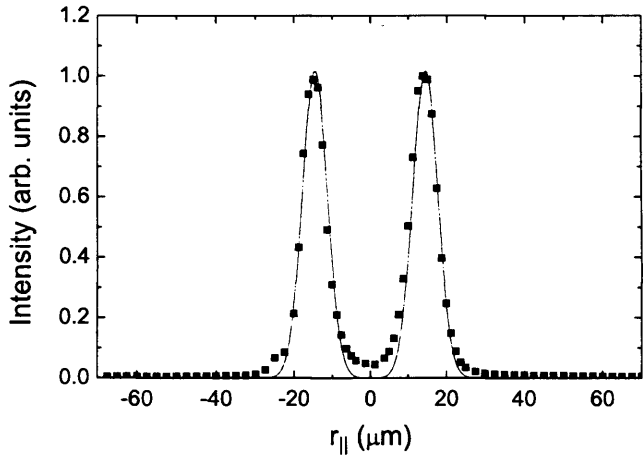
Figure 3.1: The laser intensity profile used for the creation of the optical trap. Indirect excitons are formed at a distance of $R = 15\,\mu m$ from the trap centre. The experimental points are fitted by the continuous line.

OPTICAL TRAPPING

Optical trapping offers the unique advantage of precise and fast control of the trapping potential in a non-invasive manner. The dipolar character of indirect excitons is exploited in order to form a potential trap with the energy minimum at its centre when excitons are created in a ring-shaped spot. Their mutual dipole repulsion increases the energy at the excitation spot creating a barrier for excitons trapped inside the ring and preventing them from escaping. This local increase in energy is manifested in experiments as a blue shift with increasing density and for $n_{2D} = 10^{10}\,cm^{-2}$ is approximated by $U_{trap} = E_{shift} = u_0 n_{2D} \simeq 1.6\,meV$. Figure 3.1 shows the laser intensity profile used in the experiments to create the optical trap with a minimum at its centre.

The laser-induced exciton trapping can be controlled *in situ* by varying the laser intensity in space and time. In addition, excitons collected at the trap centre are essentially thermalised with effective temperature close to that of the lattice since they are far from the hot excitation ring. The combination of indirect excitons' long radiative lifetime together with their fast expansion due to drift and diffusion forces, allows for accumulation of a dense and cold exciton gas at the trap centre. Before
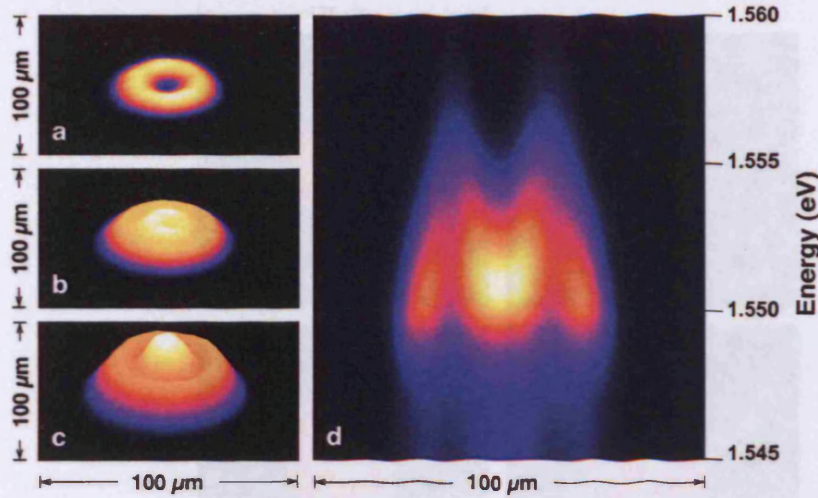
Figure 3.2: Experimental plots of the PL intensity from excitons created by a ring-shaped laser excitation, (a)-(c) in the $x-y$ plane and (d) in the $E-x$ plane. The excitation powers are $P_{ex} = 10, 35, 100$ and $75\,\mu W$ for (a), (b), (c) and (d), respectively, and the lattice temperature is $T_b = 1.4\,K$. Taken from Ref. [136]

presenting the kinetics of indirect excitons in the optically-induced trap it is useful to obtain an insight in the details of the experiment.

3.2 EXPERIMENTAL RESULTS

In the experiments the spatial x-y PL pattern is acquired by a CCD camera after removal of the low energy bulk emission through spectral selection. In Fig. 3.2 the exciton PL is plotted both in the x-y and E-x plane revealing a laser excitation ring with diameter of $30\mu m$ and ring thickness which follows a Gaussian profile with FWHM$= 2\sigma \simeq 10\mu m$. The excitons are photogenerated using rectangular excitation pulses with $500\,ns$ duration, edge sharpness $\leq 1\,ns$ and repetition frequency 1 MHz emitted by a pulsed semiconductor laser diode at 635nm. This allows the exciton gas to reach equilibrium during the laser pulse while between pulses complete decay of the exciton PL is achieved. The applied gate voltage, $V_g = 1.2\,V$ results in a ground state radiative lifetime of $2\tau_R = 50\,ns$. The exciton density profile was estimated from the measured exciton energy profiles in E-x coordinates using the relation between the
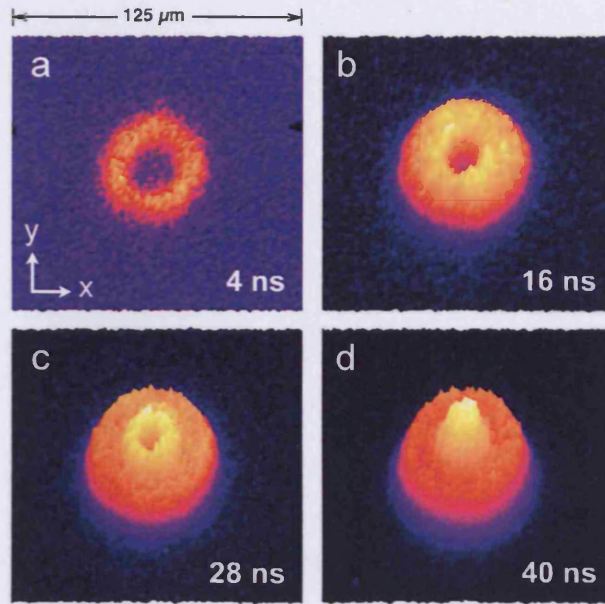
Figure 3.3: Time resolved images of laser-induced trapping of excitons collected by a photogated CCD. (a)-(d) x-y plots of the PL intensity from indirect excitons collected at delays of 4, 16, 28, and 40 ns relative to the start of 535 nm pulsed laser diode excitation in a 30 μm diameter ring on the CQW sample. The time-integration window for each image is 4 ns and the experimental parameters used are: average excitation power P_{ex} =75 μW, bath temperature $T_b = 1.4$ K and gate voltage $V_g = 1.2$ V

energy and density of the indirect excitons $\delta E = 4\pi e^2 n_{2D} d/\varepsilon_b$, where $d = 11.5$ nm for the studied sample [2]. The power of the laser was $P_{ex} = 75\,\mu$W and all experiments were performed at $T_b = 1.4$ K. Spectral filtering and time-gated imaging where combined to allow the direct visualisation of the exciton emission in spatial coordinates as a function of delay time with 4 ns time-resolution and 2 μm spatial resolution.

The kinetics presented in Fig. 3.3 demonstrate that the exciton pattern reaches a stationary state and therefore the collection of degenerate excitons in the trap centre is completed within 40 ns, *i.e.*, in a timescale comparable to the exciton lifetime. This is favourable for studies of confined degenerate gases. Furthermore, for the excitation power used in the experiments, the density of excitons at the trap centre reaches $\sim 1.4 \times 10^{10}$ cm^{-2} within 40 ns. The result after the passage of 40 ns is a dense and, as shown below, cold gas, essentially at the lattice temperature, within an area of 100μm^2 around the trap centre.

3.3   THEORETICAL MODEL

The theoretical model developed to simulate the kinetics of indirect excitons in an optical trap consists of a quantum diffusion equation which describes the exciton transport and an equation for the evolution of the exciton effective temperature in the trap. The optical lifetime of excitons is given by Eq. (1.38) and is also included in numerical simulations, as it affects both the temperature and the transport properties of excitons. The simultaneous solution of the system of these three coupled nonlinear equations is achieved by means of a finite difference numerical method. Apart from an astonishing agreement between theory and experiment the model is able to predict the evolution of the diffusion coefficient and the effective exciton temperature in the course of the trap loading.

3.3.1   QUANTUM DIFFUSION OF INDIRECT EXCITONS

The diffusive character of the exciton transport in QWs has been identified both in low temperature experiments and theoretical calculations. A *quantum diffusion equation* has been derived in Ref. [95] in order to describe the exciton motion under the concentration gradients and the dipole-dipole repulsion in a realistic disordered QW plane.

The quantum diffusion equation is highly nonlinear and has the form

$$\frac{\partial}{\partial t} n_{2D} = \nabla \left[D_x \nabla n_{2D} \;+\; \mu_x n_{2D} \nabla \left(u_0 n_{2D} + U_{QW} \right) \right] - \Gamma_{opt} n_{2D} + \Lambda . \qquad (3.1)$$

Let us describe in detail each term of this equation as it will be the main tool towards the understanding and simulation of the experimental observations.

The particle mobility, μ_x, is determined by the diffusion coefficient of the excitons, D_x, and given by a modified version of the Einstein relation for quasi-2D bosons:

$$\mu_x = \frac{D_x}{k_B T_0} (e^{T_0/T} - 1) . \qquad (3.2)$$

In the classical limit $T \gg T_0$ this equation reduces to the usual Einstein relation, $\mu_x = D_x/k_B T$ whereas in the quantum limit $T \leq T_0$ it gives a strong n_{2D}-dependent increase of the exciton mobility. This effect originates directly from the bosonic

character of the excitons and reflects the well-known property of boson scattering to be stimulated by the presence of already occupied states. A simple derivation of the modified Einstein relation is given in Appendix A where a gas of fermions is also considered. In the case of fermions, the particles tend to avoid each other and the result of increasing concentration is an effective phase space filling and consequently a reduced mobility in terms of D_x.

The intrinsic QW interface roughness caused by variations in the QW width and alloy fluctuations is included through the disorder potential U_{QW} and the mean-field repulsion due to the dipolar character of indirect excitons through $u_0 n_{2D}$. The sum of these two terms results in an effective potential seen by the excitons, which induces a drift force.

The last two terms describe the radiative decay and generation rates of excitons, respectively. The term $\Gamma_{opt} n_{2D}$ removes excitons at each time step and is proportional to the concentration which is determined self-consistently with Γ_{opt} given by Eq. (1.38) repeated here for clarity

$$\Gamma_{opt} = \frac{1}{\tau_{opt}} = \frac{\Gamma_0}{2} \frac{E_\gamma}{k_B T_0} \int_0^1 \frac{(1 + z^2) dz}{A e^{-z^2 E_\gamma / k_B T} - 1} . \qquad (3.3)$$

Excitons are created by a laser pulse which has a Gaussian shape in space and it is the sum of two Heaviside functions in time namely

$$\Lambda = \Lambda(r_\parallel, t) = \Lambda_0 \, e^{-(r_\parallel - R)^2 / 2\sigma^2} [\Theta(t) - \Theta(t - \tau)] . \qquad (3.4)$$

Here R is the radius of the ring excitation, 2σ its width, τ is the pulse duration and Λ_0 is the number of excitons per cm^2 generated at each ns.

The quantum diffusion equation (3.1) is based on quantum Boltzmann equation, i.e., is valid for temperatures *above* the critical temperature T_c for a transition to a collective state.

3.3.2 THERMALISATION KINETICS

The cooling of initially energetic excitons via LA-phonon emission has been described in Section 1.6 in terms of Eq. (1.37) also repeated here for clarity

$$
\left(\frac{\partial T}{\partial t}\right)_{2D} = -\frac{2\pi}{\tau_{sc}}\left(\frac{T^2}{T_0}\right)(1 - e^{-T_0/T})\int_1^\infty d\varepsilon\, \varepsilon\sqrt{\frac{\varepsilon}{\varepsilon - 1}}\left|F_z\left(a\sqrt{\varepsilon(\varepsilon - 1)}\right)\right|^2
$$
$$
\times \left(\frac{e^{\varepsilon E_0/k_B T_b} - e^{\varepsilon E_0/k_B T}}{e^{\varepsilon E_0/k_B T} + e^{-T_0/T} - 1}\right)\left(\frac{1}{e^{\varepsilon E_0/k_B T_b} - 1}\right). \tag{3.5}
$$

Apart from the scattering with phonons the exciton temperature is affected by the rate at which they recombine. In high quality QWs quasi-2D excitons can only emit bulk photons as long as their momentum lies inside the photon cone $k(\omega) = (\sqrt{\varepsilon_b}\omega)/c$, i.e., from the low-energy radiative modes. Consequently the decay rate of excitons depends on the energy they carry and can have either a cooling or a heating effect on the rest of the system depending on how large is the energy of the emitted photons in comparison with the average exciton energy. Faster decay rates of the low-energy excitons result in a net heating of the remaining excitons in the system.

This effect of *recombination heating or cooling* refers to relatively low temperatures $k_B T \ll E_\gamma \sim 1K$ when most excitons' momentum is located within the photon cone whereas at high temperatures $k_B T \gg E_\gamma \sim 1K$, only a net heating of the system occurs. Inclusion of this effect in the thermalisation equation for the effective exciton temperature is done by adding an extra term which describes the rate of change of the exciton temperature due to their decay

$$
S_{opt} = \frac{(k_B T I_2 \Gamma_{opt}) T_0}{2k_B T I_1 - k_B T_0 I_2}, \tag{3.6}
$$

where I_1 is

$$
I_1 = (1 - e^{-T_0/T})\int_0^\infty \frac{z\,dz}{e^z + e^{-T_0/T} - 1}, \tag{3.7}
$$

and I_2 is given by

$$
I_2 = e^{-T_0/T}\int_0^\infty \frac{ze^z\,dz}{(e^z + e^{-T_0/T} - 1)^2}. \tag{3.8}
$$

The final heating mechanism is the laser itself. In nonresonant exciton creation the energy injected by a focused laser excitation can be as high as $E_i/k_B \sim 200\,K$. For the purposes of numerical simulations we consider that the laser creates the excitons

monoenergetically, so their initial energy E_i is constant. The heating of the excitons by the pump source is incorporated in the thermalisation kinetics through

$$S_{\text{pump}} = \frac{(E_i - k_B T I_2) \Lambda_{T_0}}{2 k_B T I_1 - k_B T_0 I_2},$$
(3.9)

where I_1 and I_2 are given by Eqs. (3.7) and (3.8), respectively. S_{pump} is the rate at which the exciton temperature changes due to the pump, and is always positive, $i.e.$, the laser has a net heating effect.

The term Λ_{T_0} is given by

$$\Lambda_{T_0} = \frac{T_0}{n_{2D}} \Lambda(t),$$
(3.10)

where $\Lambda(t)$ is the exciton creation rate per cm^2 defined as

$$\Lambda(t) = \Lambda_0 [\Theta(t) - \Theta(t - \tau)].$$
(3.11)

The resulting equation including all possible heating mechanisms reads

$$\frac{\partial T}{\partial t} = \left(\frac{\partial T}{\partial t} \right)_{n_{2D}} + S_{\text{pump}} + S_{\text{opt}}.$$
(3.12)

3.3.3 DIFFUSION COEFFICIENT: THERMIONIC MODEL

In order to achieve a better agreement between theory and experiment the diffusion coefficient was adjusted to increase as a high concentration of excitons builds up and the QW disorder potential is flattened. The effective n_{2D}-dependent screening of the disorder potential $U_{\text{QW}} = U_{\text{rand}}(r_\|)$ by dipole-dipole interacting indirect excitons is crucial for the drastic decrease of the time needed to fill up the optically-induced trap. The thermionic model, derived from Eq. (3.1) for a long-range correlated disorder potential, yields the effective diffusion coefficient:

$$D_x = D_x^{(0)} \exp \left[- \frac{U^{(0)}}{k_B T + u_0 n_{2D}} \right],$$
(3.13)

where $U^{(0)} = 2 \langle |U_{\text{rand}}(r_\|) - \langle U_{\text{rand}}(r_\|) \rangle| \rangle$ and $D_x^{(0)}$ is the in-plane diffusion coefficient in the absence of QW disorder [95].

The system of coupled Eqs. (3.1), (3.3) and (3.12) has been previously used to describe the optical trapping of excitons in the steady state [72, 136]. In this Chapter the

dynamics of the laser trapping is modelled by solving the system of three equations in space and time domains.

3.4 THEORETICAL RESULTS

Equations (3.1), (3.3) and (3.12) are solved numerically with the optical excitation being positioned at $R = 15 \, \mu m$, and the ring thickness has a Gaussian shape with $\sigma = 5 \, \mu m$ (FWHM = $2\sqrt{2 \ln 2} \sigma = 11.7 \, \mu m$). As has been shown in earlier works [136] where the stationary solutions of Eq. (3.1) were studied, at low excitation powers, $P_{ex} \sim 10 \, \mu W$ the PL profile is similar to the excitation profile. However, as P_{ex} increases a strong PL signal is detected at the centre of the excitation ring, indicating the presence of a cold and dense gas of excitons. In the simulations the excitation power of $P_{ex} = 75 \, \mu W$ corresponds to an exciton generation rate of $\Lambda_0 = 1.1 \times 10^9 \, cm^{-2} ns^{-1}$. The initial injected energy at this excitation power as inferred from the experiment is $E_i/k_B = 100 \, K$ and the lattice temperature is kept to $T_b = 1.4 \, K$.

The ring-shaped laser induces an annular trap with a radius slightly different to the radius of the laser ring. The trap boundary, R_{tr}, is defined as the location where $n_{2D} = n_{2D}^{max}$ right after the pulse is switched on, since the trap is created by the exciton concentration distribution, $n_{2D}(r_\parallel)$. The trap radius is $R_{tr} \simeq 11 \, \mu m$ and the laser ring radius $R = 15 \, \mu m$, therefore $R_{tr} < R$.

The numerical simulations were performed by using control parameters consistent with those found in previous studies [136, 164] of similar structures: $u_0 = 1.6 \times 10^{-10} \, meVcm^2$, $U^{(0)} = 1.2 \, meV$, $D_x^{(0)} = 35 \, cm^2/s$, $m = 0.215 \, m_0$ (m_0 is the free electron mass), $E_x = 1.55 \, eV$, and the deformation potential of exciton – LA-phonon interaction $D_{dp} = 6.5 \, eV$.

The first series of simulations are performed in the presence of the excitation pulse and the evolution of the exciton density, PL intensity, diffusion coefficient and occupation number is recorded with temporal resolution of 4 ns as shown in Fig. 3.4. Right after the pulse is switched on, a high concentration of excitons is found along the ring perimeter but within approximately 40 ns the excitons are collected in the trap centre reaching a concentration of $\sim 1.4 \times 10^{10} \, cm^{-2}$. At the same time the PL intensity from the trap centre increases indicating that the low-energy excitons have accumulated there which is consisted with a macroscopically large occupation number of $N_{E=0} \simeq 1$

Figure 3.4: The temporal evolution of (a) the exciton density, (b) PL intensity, (c) diffusion coefficient and (d) ground state occupation number during the pulse, calculated with the theoretical model.

at the trap centre. Hence, even without any assumption of transition to a superfluid phase the non-classical values of the ground state occupancy indicate the build up of a quantum degenerate gas. Note that the ground state occupation number would be much higher should the laser intensity was higher or the lattice temperature was lower. However, in that case the appearance of spontaneously developed coherence –a signature of BEC– should be considered and our description of the exciton transport with Eq. (3.1) would cease to be valid. These considerations are a subject of ongoing research both from an experimental and a theoretical point of view.

Within the pulse duration the system in the trap centre reaches a steady state with a well-defined temperature which coincides with the lattice temperature. In the second series of simulations the stationary state parameters are used as an input for the evolution of the system after the laser excitation is removed. As the confining potential of the optical trap disappears the exciton gas expands in the QW plane. Moreover, the major source of heating, *i.e.*, the laser, is absent and consequently more excitons start to occupy the low-energy states giving rise to a drastic increase of the PL signal.
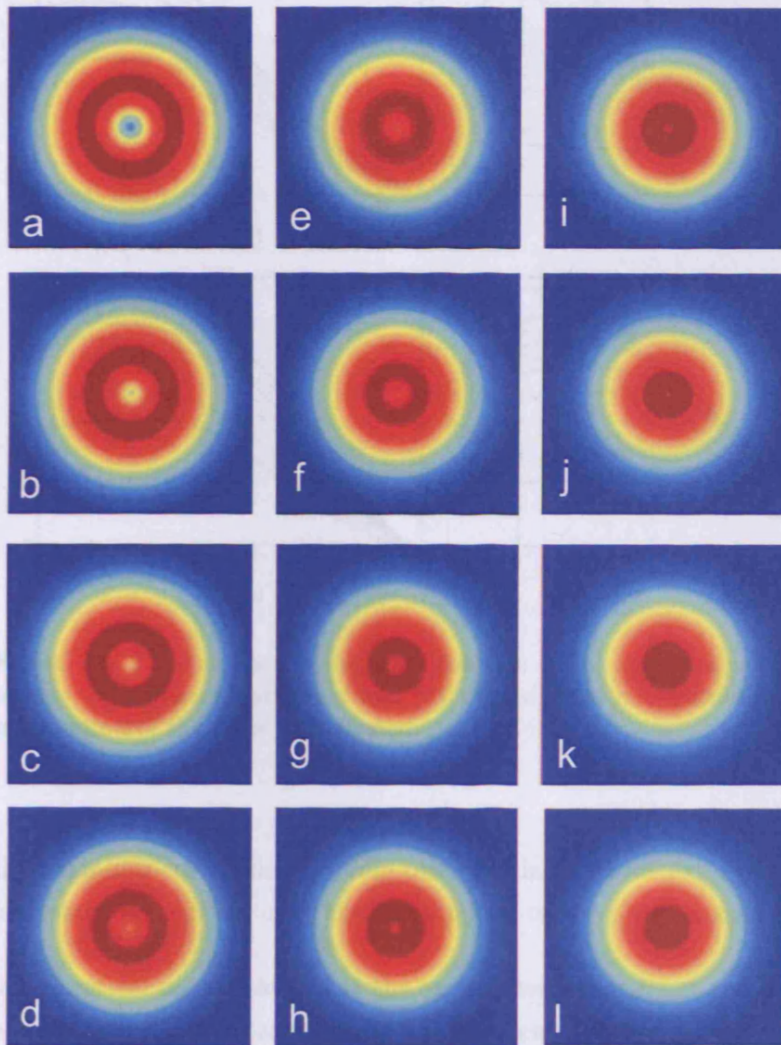
Figure 3.5: Temporal evolution of the calculated exciton concentration in the optical trap after the laser pulse is switched on. Each figure (a)-(l) represents a snapshot of the exciton density in the x-y plane every 4 ns. The trap centre is loaded with a dense exciton gas within 40 ns. The laser excitation profile has a $30\,\mu$m diameter and all the parameters are chosen to fit the experimental conditions. The maximum density is shown by the red colour, then magenta, yellow and green represent decreasing densities and blue corresponds to the background concentration.

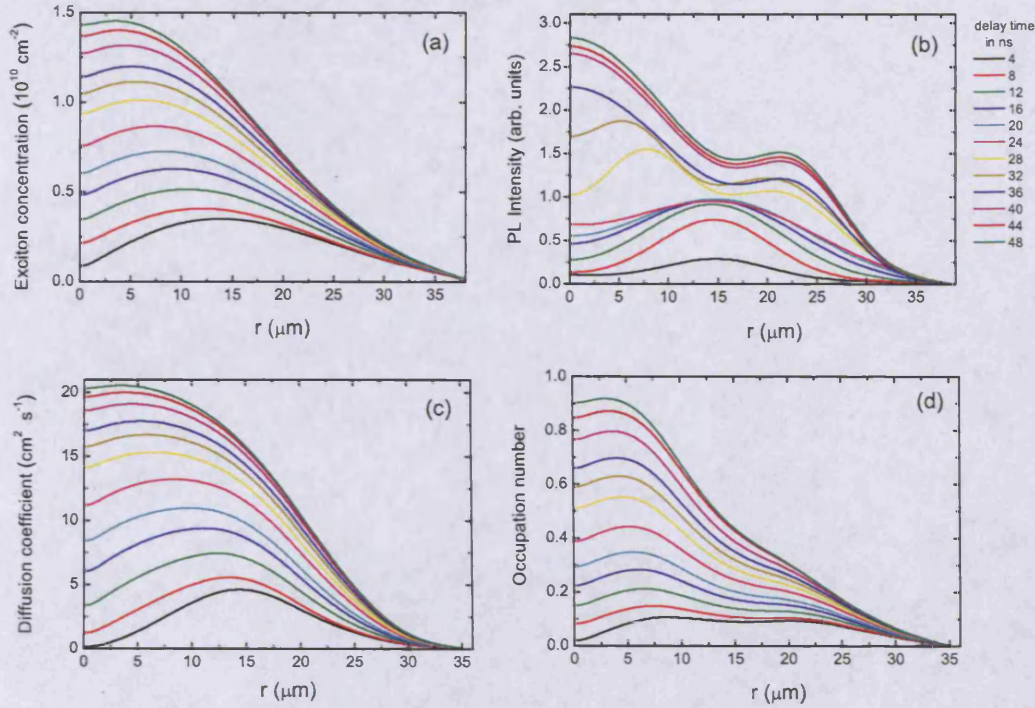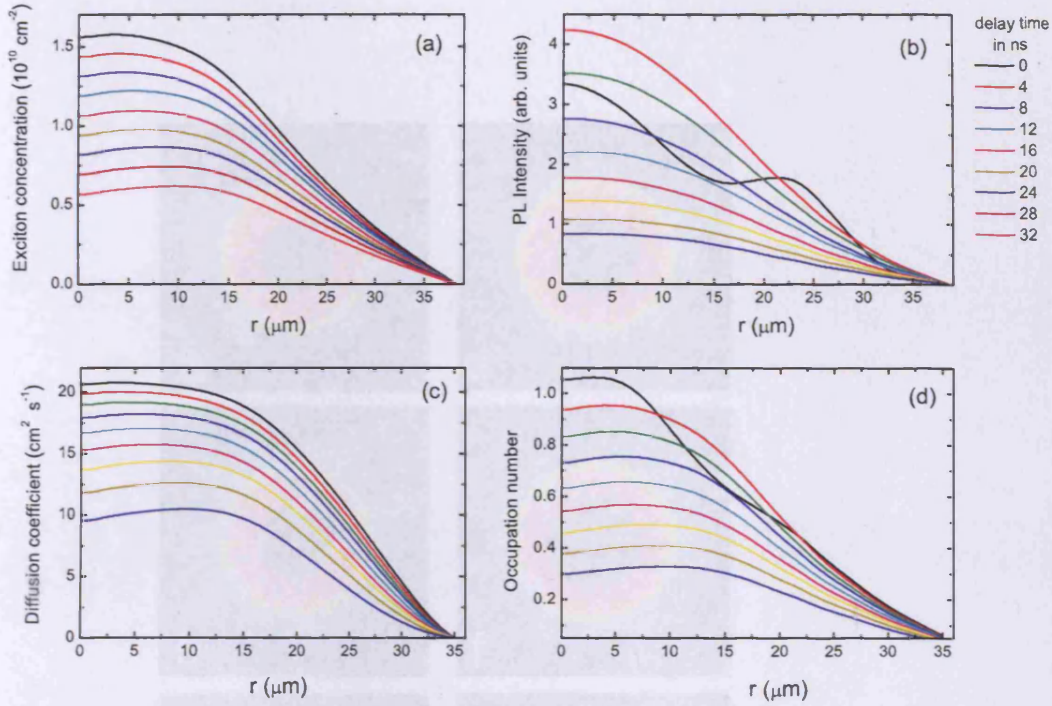Figure 3.6: The calculated temporal evolution of (a) the exciton density, (b) PL intensity, (c) diffusion coefficient and (d) ground state occupation number, relative to termination of the pulse as indicated.

This is reminiscent of the *PL jump* observed in previous experiments. The temporal evolution of the system after the termination of the pulse is shown in Fig. 3.6.

The theoretical results show that the exciton temperature at the trap centre is indeed the same as the lattice temperature T_b. The temperature is maximum at the position of the excitation at $t = 0$ but as time passes and the moving particles transfer energy away from the ring, it decreases. A small heating effect seen outside the excitation ring could be due to absorption of the laser energy from the crystal lattice which results in a temperature slightly higher than the cryostat temperature of 1.4 K. The evolution of temperature at each spatial point with the passage of time is shown in Fig. 3.8 where is evident that the main heating mechanism is the laser pulse: after the pulse is switched off, the system thermalises to the lattice temperature within hundreds of ps. In the following Section, the theoretical predictions are compared with the experimental observations.
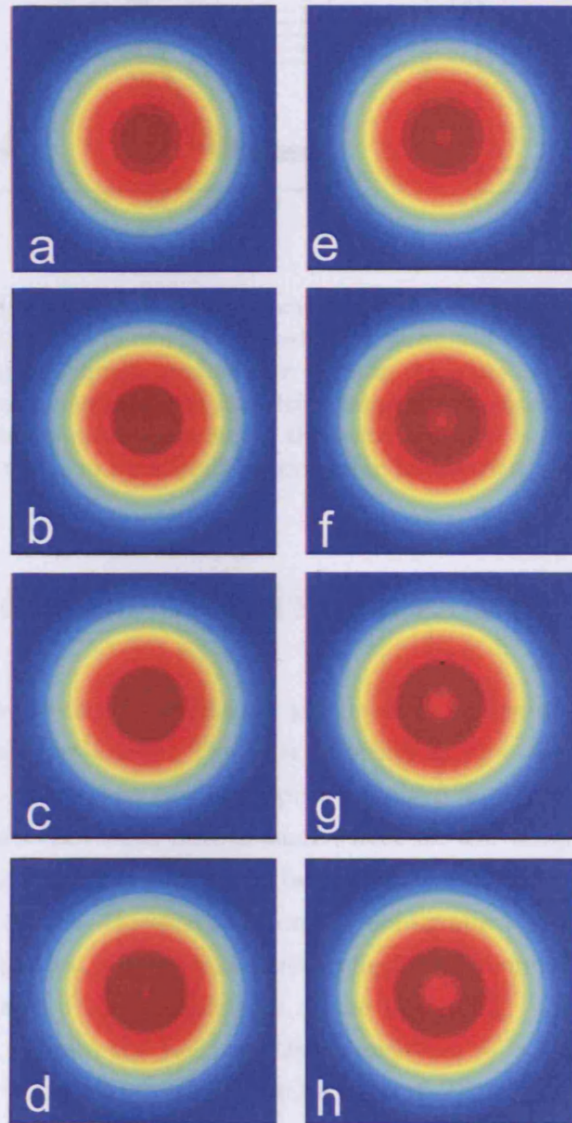
Figure 3.7: Calculated concentration of excitons after the termination of the pulse. The experimental parameters are the same as those during the pulse, the temporal resolution is 4 ns and the colour legend is the same as in Fig. 3.5.
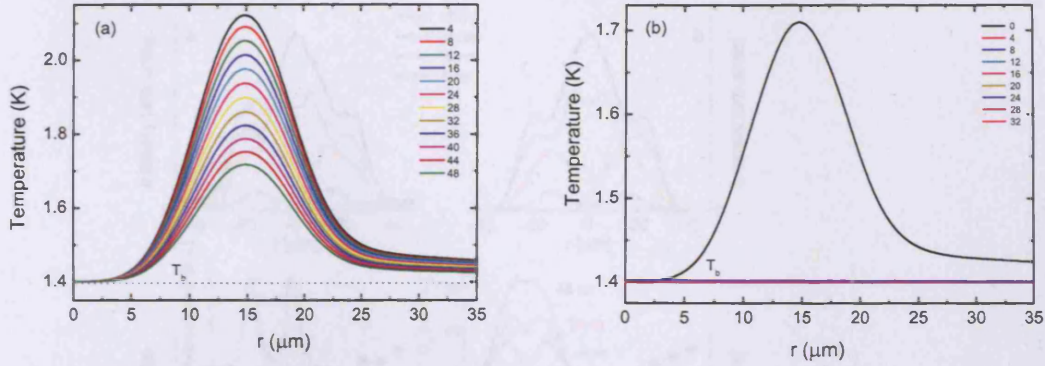
Figure 3.8: The effective exciton temperature as a function of the radial coordinate for successive time steps of 4 ns, (a) during the pulse and (b) after its termination. At the position of the circular excitation $r = 15\mu m$ the temperature is maximum but at the trap centre it coincides with the lattice temperature. Excitons at the trap centre reach the bath temperature even during the pulse and after it switched of they all excitons share the common bath temperature within hundreds of ps.

3.5   COMPARISON WITH EXPERIMENTS

In the experiment, the excitation profile does not coincide exactly with that used in numerical simulations. The laser intensity at $r_\parallel = 0$, although extremely low, is not equal to zero, but can be approximately 5 % of the maximum intensity. It is possible that this could have a small effect on the temperature of the excitons at the centre of the trap: they could be slightly hotter than the predicted values in the theoretical results. However, a stronger cooling effect is expected at lower T_b due to the recombination heating and cooling effect, and therefore, the exciton temperature would be around the temperature of the lattice T_b. This means that at lower T_b ($T_b \lesssim 1\,\mathrm{K}$), despite the fact that the intensity at $r_\parallel = 0$ is not zero in experiments, the exciton temperature would still be close to T_b.

The experimental data were compared to the theoretical calculations of the exciton kinetics and the control parameters were chosen to fit the experimental conditions. As can be seen in Fig. 3.9 the measured and calculated kinetics of the exciton spatial patterns are in excellent agreement. The PL intensity at the centre of the trap increases towards a maximum within 40 ns, the time needed for the loading of the trap with the degenerate exciton gas. During the pulse the PL signal increases both at the position of the excitation and the trap centre and saturates within 50 ns as is
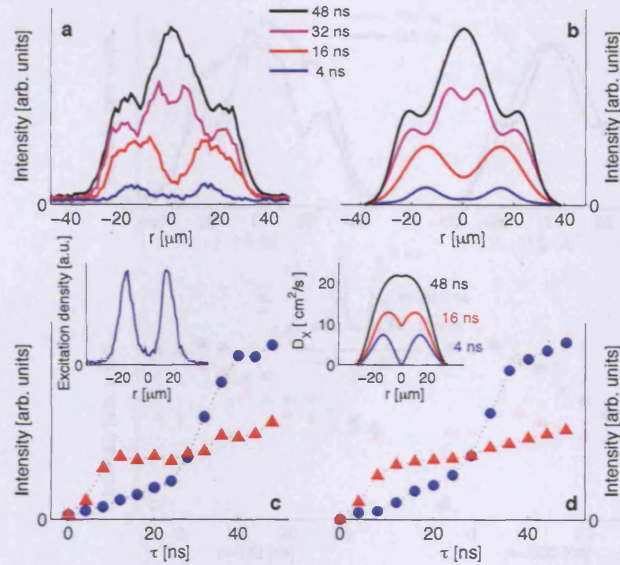
Figure 3.9: Kinetics of the indirect exciton PL profile following the onset of the ring-shaped laser excitation pulse. The measured (a) and calculated (b) cross-sections of the indirect exciton PL across the diameter of the laser excitation ring as a function of time. The measured (c) and calculated (d) indirect exciton PL intensity at the ring centre (blue triangles) and in the area of the laser excitation ring (red circles) as a function of time. The time-integration window for each profile (a,b) and point (c,d) is 4 ns. $\tau = 0$ and $\tau = 500$ ns correspond to the onset and termination of the rectangular laser excitation pulse, respectively. Left inset: The ring-shaped laser excitation profile. Right inset: The calculated radial dependence of the exciton diffusion coefficient for different time delays.

depicted in Figs. 3.9 (c) and 3.9 (d). The temporal evolution of the diffusion coefficient is also shown in the inset and can be understood in the grounds of screening of disorder with increasing exciton density. The maximum value of the diffusion coefficient at the end of 50 ns coincides with that previously calculated in steady state simulations [2].

Additional important information was obtained by measuring the indirect exciton kinetics in the optically-induced trap after the trap removal by switching off the laser excitation pulse. When the laser pulse is switched off, a jump in the exciton PL is observed in the region of laser excitation. As shown in previous studies, only the low-energy excitons with the energy $E < E_0 = E_g^2 \varepsilon_b/(2mc)$, in the so-called radiative zone, are optically active [75, 165]. The PL-jump is caused by the increase
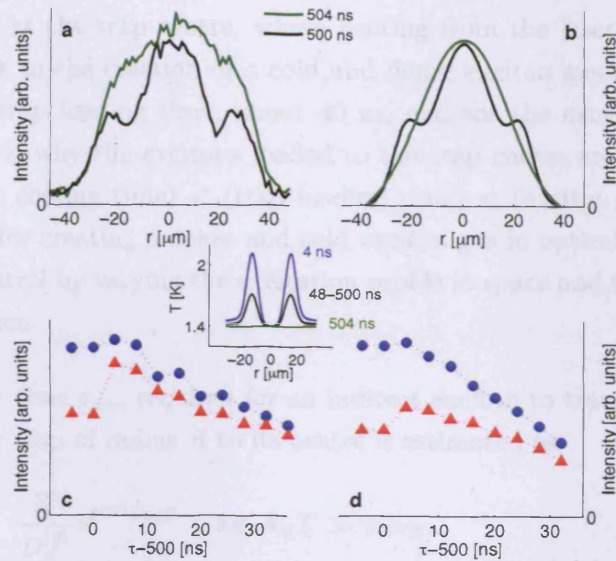
Figure 3.10: Same as in Fig. 3.9 but following the termination of the ring-shaped laser excitation pulse. $\tau = 0$ and $\tau = 500$ ns correspond to the onset and termination of the rectangular laser excitation pulse, respectively. Inset: The calculated temperature across the ring diameter in the beginning of the laser excitation pulse at $\tau = 4$ ns (blue), in the stationary regime achieved during the 500 ns-long excitation pulse about 40 ns after its start $\tau = 48$ to 500 ns (black) and 4 ns after the termination of the laser excitation pulse at $\tau = 504$ (green).

of the radiative zone occupation due to the cooling of the high-energy dark excitons after switching off the laser excitation [107]. The time-resolved imaging experiments presented in Fig. 3.10 show that the PL-jump is observed only in the region of laser excitation, where the excitons are heated by the laser. The excitons in this region rapidly cool down to the lattice temperature, within 4 ns after switching off the laser excitation (see inset in Fig. 3.10) much faster than the exciton lifetime which is about 50 ns.

More importantly, the data show that there is no PL-jump at the trap centre (Fig. 3.10). This proves that the excitons at the trap centre are cold, essentially at the lattice temperature, even during the excitation pulse. The indirect excitons photogenerated at the laser excitation ring travel to the trap centre due to drift and diffusion. They can travel over long distances before optical recombination due to their long lifetimes.

The data (Fig. 3.10) show that during this travel, the excitons thermalise to the crystal lattice temperature at the trap centre, where heating from the laser excitation is negligible. This leads to the creation of a cold and dense exciton gas at the trap centre. The observed trap loading time, about 40 ns, exceeds the exciton cooling time, < 4 ns, and this is why the excitons loaded to the trap centre are cold. The time hierarchy (exciton cooling time) < (trap loading time) < (exciton lifetime in the trap) is favourable for creating a dense and cold exciton gas in optically-induced traps and its in-situ control by varying the excitation profile in space and time before the exciton recombination.

By using Eq. (3.13), the time τ_{trav} required for an indirect exciton to travel from the boundary of an annular trap of radius R to its centre is estimated as

$$\tau_{\mathrm{trav}}^{(1)} = \frac{R^2}{D_{\mathrm{x}}^{(0)}} e^{U^{(0)}/k_{\mathrm{B}}T} \quad \text{for } k_{\mathrm{B}}T \gg u_0 n_{\mathrm{2D}}, \tag{3.14}$$

$$\tau_{\mathrm{trav}}^{(2)} = \frac{R^2}{D_{\mathrm{x}}^{(0)}} \frac{k_{\mathrm{B}}T}{u_0 n_{\mathrm{2D}}^{(0)}} e^{U^{(0)}/(u_0 n_{\mathrm{2D}}^{(0)})} \quad \text{for } k_{\mathrm{B}}T \ll u_0 n_{\mathrm{2D}}, \tag{3.15}$$

where $n_{\mathrm{2D}}^{(0)}$ is the density of photoexcited indirect excitons at the boundary of the trap, and the low-density limit ($n_{\mathrm{2D}} < 10^9\,\mathrm{cm}^{-2}$) refers to the unscreened disorder potential, while the high-density limit ($n_{\mathrm{2D}} \geq 10^{10}\,\mathrm{cm}^{-2}$) deals with effective mean-field screening of $U_{\mathrm{rand}}(\mathbf{r}_{\parallel})$. In the low-density limit, the excitons are essentially localised by disorder, the diffusion coefficient is small, $D_{\mathrm{x}} = D_{\mathrm{x}}^{(0)} \exp[-U^{(0)}/(k_{\mathrm{B}}T)] \sim 0.1\,\mathrm{cm}^2/\mathrm{s}$, and the in-plane transport of excitons out of the excitation spot cannot be seen because in this case $\tau_{\mathrm{trav}}^{(1)} \gg \tau_{\mathrm{opt}}$. In contrast, for $k_{\mathrm{B}}T \ll u_0 n_{\mathrm{2D}}$ the diffusion coefficient is large, $D_{\mathrm{x}} = D_{\mathrm{x}}^{(0)} \exp[-U^{(0)}/(u_0 n_{\mathrm{2D}})] \sim 10\,\mathrm{cm}^2/\mathrm{s}$, giving rise to the drastic decrease of the characteristic travel time τ_{trav}. According to Eqs. (3.14)-(3.15), $\tau_{\mathrm{trav}}^{(2)} = \beta \tau_{\mathrm{trav}}^{(1)} \ll \tau_{\mathrm{trav}}^{(1)}$ with the dimensionless smallness parameter $\beta \sim 10^{-3} - 10^{-5}$ (for $T \sim 1\,\mathrm{K}$, $U_0 \sim 1\,\mathrm{meV}$, and $n_{\mathrm{2D}} \sim 10^{10}\,\mathrm{cm}^{-2}$). The transition from localised to delocalised indirect excitons is indeed observed with increasing density [1, 2, 136].

The calculated change of the exciton diffusion coefficient, due to screening of CQW disorder, is shown in the right inset of Fig. 3.9. A drastic increase of D_{x} with increasing n_{2D} is consistent with the above estimates. For the experiments studied in this Section, evaluations with Eq. (3.15) yield $\tau_{\mathrm{trav}}^{(2)} \simeq 4.6\,\mathrm{ns}$ against $\tau_{\mathrm{opt}} \simeq 50\,\mathrm{ns}$, i.e., the condition $\tau_{\mathrm{trav}}^{(2)} \ll \tau_{\mathrm{opt}}$ is clearly met.

3.6 NUMERICAL PROCEDURE

The solution of mathematical equations which model experimental situations is possible by methods of numerical analysis. Although the quest for analytical solutions of the quantum diffusion equation is an ongoing effort, inclusion of the equations for the thermalisation and optical decay forces us to develop numerical methods for the solution of the system of three coupled nonlinear equations. In this Section two methods used for the simulations presented in this and in the previous Chapter are described and suggestions for further improvement are discussed.

FINITE-DIFFERENCE SOLUTION: EXPLICIT METHOD

In all our previous simulations only solutions with cylindrical symmetry were investigated. This choice simplifies vastly the numerical effort needed and is justified by the symmetric patterns observed in the experiments. As a result the concentration is a function of the radial coordinate r and time t which implies a two-dimensional problem in terms of numerical procedure, namely with one spatial and one temporal variable. One can introduce the dimensionless variables $X = r/l$, $T = D_x t/l^2$ and $c = n_{2D}/n_0$ where l is the characteristic diffusion length, D_x is the diffusion coefficient and n_0 is some standard concentration such as the background value far from the excitation spot.

The transport of excitons in the quantum well plane with the passage of time is equivalent to determining the value of the concentration in a two-dimensional grid formed by the X and T variables. Let the range in X be divided into equal intervals δX and the time into intervals δT, so that the X-T region is covered by a grid of rectangles, as in Fig. 3.11, of sides $\delta X, \delta T$. The coordinates of a representative grid point (X, T) are $(i\delta X, j\delta T)$ where i and j are integers. We denote the value of c at the point $(i\delta X, j\delta T)$ by $c_{i,j}$ with corresponding values at neighbouring points labelled as in Fig. 3.11. By using Taylor's expansion in the T direction but keeping X constant, we can write

$$c_{i,j+1} = c_{i,j} + \delta T \left(\frac{\partial c}{\partial T} \right)_{i,j} + \frac{1}{2}(\delta T)^2 \left(\frac{\partial^2 c}{\partial T^2} \right)_{i,j} + \dots, \qquad (3.16)$$

from which follows that the derivative with respect to time is

$$\left(\frac{\partial c}{\partial T}\right)_{i,j} = \frac{c_{i,j+1} - c_{i,j}}{\delta T} + O(\delta T),\tag{3.17}$$

where $O(\delta T)$ signifies that the leading term to have been neglected is of the order of δT. Similarly, by applying Taylor's series in the X direction the second spatial derivative reads

$$\left(\frac{\partial^2 c}{\partial X^2}\right)_{i,j} = \frac{c_{i+1,j} - 2c_{i,j} + c_{i-1,j}}{(\delta X)^2} + O(\delta X)^2.\tag{3.18}$$

If for the moment we neglect the drift terms and consider pure diffusion the equation that has to be solved numerically has the form

$$\left(\frac{\partial c}{\partial T}\right) = \left(\frac{\partial^2 c}{\partial X^2}\right).\tag{3.19}$$

By substituting Eqs. (3.17) and (3.18) into Eq. (3.19) and rearranging, we obtain

$$c_{i,j+1} = c_{i,j} + r(c_{i-1,j} - 2c_{i,j} + c_{i+1,j}),\tag{3.20}$$

where $r = \delta T/(\delta X)^2$.

With reference to Fig. 3.11, we can use Eq. (3.20) with a fixed value of r to calculate the values of c at all points along successive time rows of the grid provided we are given some initial starting values at $T = 0$ and some conditions on the boundaries $X = 0, X = 1$. A formula such as Eq. (3.20), which enables one unknown variable to be expressed directly in terms of known values, is called an *explicit finite-difference formula*. It has been shown [166] that the value $r = 1/2$ is critical so that instabilities develop for values of r larger than this. The stability condition could therefore be expressed as $r \leq 1/2$, a fact which imposes severe limitations on the value of δT for a given δX. This forces us to take a large number of small time steps during the iterative procedure used to reach a solution. Generalisation of the above discussion in order to include the drift term is straightforward and consists of expressing the first order spatial derivatives as

$$\left(\frac{\partial c}{\partial X}\right)_{i,j} = \frac{c_{i+1,j} - c_{i,j}}{\delta X} + O(\delta X)\tag{3.21}$$

and substituting in the drift-diffusion equation.
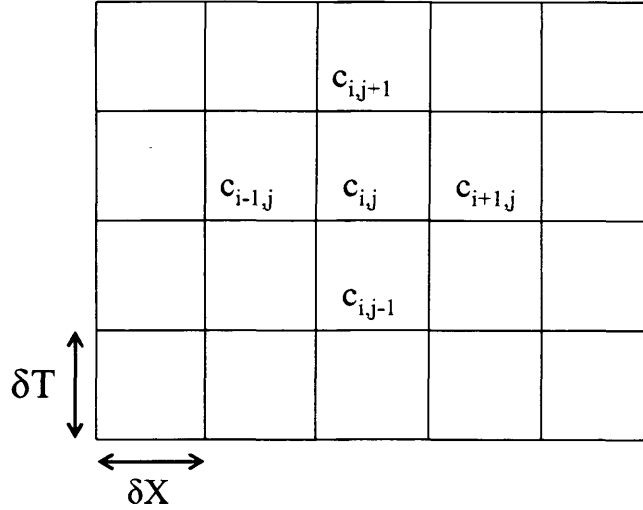
Figure 3.11: The two-dimensional grid used in numerical calculations, comprises one spatial and one temporal dimension. The value of the concentration is calculated at each grid point and corresponds to the concentration at each point in space every time step.

CRANK-NICOLSON IMPLICIT METHOD

An alternative method which is widely used in diffusion problems is the so called Crank-Nicolson method [167]. The main idea is to substitute $\partial^2 c / \partial X^2$ by the mean of its finite-difference representations on the jth and $(j + 1)$th time rows so that Eq. (3.19) can be approximated by

$$\frac{c_{i,j+1} - c_{i,j}}{\delta T} = \frac{c_{i+1,j} - 2c_{i,j+c_{i-1,j}}}{(\delta X)^2} + \frac{c_{i+1,j+1} - 2c_{i,j+1} + c_{i-1,j+1}}{(\delta T)^2}, \qquad (3.22)$$

which can be rearranged as

$$-rc_{i-1,j+1} + (2 + 2r)c_{i,j+1} - rc_{i+1,j+1} = rc_{i-1,j} + (2 - 2r)c_{i,j} + rc_{i+1,j}. \qquad (3.23)$$

The three unknown values on the time level $j+1$ can be determined through the three known values of c on the jth level. Assuming that there are N internal points in the grid along each time row, for $j = 0$ and $i = 1, 2, ..., N$, Eq. (3.23) gives for each time step a system of N simultaneous equations for the N unknown variables in terms of the known initial values and the boundary values at $i = 0$ and $i = N + 1$. Similarly

a new set of $N \times N$ equations has to be solved in the next time step in terms of the values calculated in the previous step. Such a computational scheme where a solution of a set of simultaneous equations is needed at each time step is called an *implicit method*. Note that despite the fact that an increased amount of computational labour is involved at each time step, no limitations on the values of r are assumed. This is a strong advantage which allows us to consider larger and hence fewer time steps.

TWO-DIMENSIONAL DIFFUSION: ALTERNATING DIRECTION IMPLICIT METHODS

The methods described above can easily be extended to two spatial dimensions. The corresponding form of Eq. (3.19) over a rectangular region $0 \leq x \leq a, 0 \leq y \leq b$ is

$$\left(\frac{\partial c}{\partial T}\right) = D_x \left(\frac{\partial^2 c}{\partial x^2} + \frac{\partial^2 c}{\partial y^2}\right). \tag{3.24}$$

The region where diffusion occurs has to be covered with a rectangular space grid at each time step with coordinates

$$x = i\delta x, \quad y = j\delta y, \quad t = n\delta t, \tag{3.25}$$

where i, j, n are positive integers and the values of c at each grid point are denoted by $c_{i,j,n}$. The explicit finite-difference method applied to Eq. (3.24) yields

$$\begin{aligned}
\frac{c_{i,j,n+1} - c_{i,j,n}}{\delta t} &= \frac{D_x}{(\delta x)^2}(c_{i-1,j,n} - 2c_{i,j,n} + c_{i+1,j,n}) \\
&+ \frac{D_x}{(\delta y)^2}(c_{i,j-1,n} - 2c_{i,j,n} + c_{i,j+1,n}),
\end{aligned} \tag{3.26}$$

with an extremely severe stability criterion expressed as

$$D_x \left[\frac{1}{(\delta x)^2} + \frac{1}{(\delta y)^2}\right] \delta t \leq \frac{1}{2}, \tag{3.27}$$

and imposing the use of very small time steps δt. On the contrary no such limitation exist in the case of the Crank-Nicolson method which now reads

$$\frac{c_{i,j,n+1} - c_{i,j,n}}{\delta t} = \frac{1}{2} D_x \left\{\left(\frac{\partial^2 c}{\partial x^2} + \frac{\partial^2 c}{\partial y^2}\right)_{i,j,n} + \left(\frac{\partial^2 c}{\partial x^2} + \frac{\partial^2 c}{\partial y^2}\right)_{i,j,n+1}\right\}, \tag{3.28}$$

and requires the solution of $(N-1)(M-1)$ simultaneous algebraic equations for each time step δt, where $N\delta x = a$ and $M\delta y = b$. In general, the values of c at five grid points have to be determined and this can be achieved by direct elimination using an iterative procedure.

A method which offers considerably improved efficiency is the *alternating direction implicit method* (ADI method). Its essential feature is to replace only one second-order spatial derivative by an implicit difference approximation leaving the other to be treated explicitly. By applying this idea to each of the $(N-1)$ points along a grid line parallel to the x-direction one obtains $(N-1)$ simultaneous equations, each one containing only three unknowns, which have to be solved $(M-1)$ times. Obviously this is much easier than the solution of the $(N-1)(M-1)$ simultaneous equations needed in an implicit method. Consequently, the solution is advanced from the $(n+1)$th to the $(n+2)$th step by interchanging the treatment of the second-order derivatives.

Both explicit and implicit methods were tested towards the solution of the nonlinear diffusion equation and the latter turned to be more stable and efficient corresponding to the amount of computational work they required. As mentioned above only cylindrically symmetric solutions were considered and therefore two independent variables were adequate for the description of transport along the quantum well plane. However, if one is interested in describing the fragmentation of the external ring in terms of Eq. (3.1), one has to use the most sophisticated ADI method and treat the two spatial dimensions independently. Although this is beyond the scope of the present work, it offers an interesting challenge for future use of the nonlinear diffusion equation in order to interpret and describe the intriguing and so far unexplained pattern formation observed in the experiments.

3.7 SUMMARY

In this Chapter, the spatial and spectral kinetics of excitons in the optically-induced trap were simulated numerically in order to reproduce the experimental observations. The results demonstrate a rapid loading of the trap by cold excitons on a timescale less than the exciton lifetime and prove the feasibility of accumulating a dense and cold exciton gas in optically-induced traps.

4 SPATIAL COHERENCE OF QUANTUM WELL EXCITONS

4.1 INTRODUCTION

Coherence is an essential intrinsic property of quantum mechanical particles. A particle is called coherent if it propagates like a wave packet with well-defined phases for its spectral components. Such particles have the ability to produce interference patterns. Constructive interference leads to macroscopic coherence of an ensemble of particles. The coherence of such an ensemble is destroyed by phase-relaxing processes of its individual members.

For a system in a condensed phase all particles are considered to be in the same quantum state and they are described by a common wavefunction and therefore share a common phase, *i.e.*, they are coherent. Excitonic coherence is spatially limited due to interactions within the exciton ensemble and its coupling to the environment. Typically, excitons are detected by their luminescence which is expected to inherit any coherence properties the exciton system may have. As a result, the large coherence lengths observed recently in experiments with quantum well excitons [168, 169] and microcavity polaritons [170, 171] are attributed to the appearance of a condensed phase and therefore build up of spontaneous coherence.

In the remainder of this chapter the spatial coherence in a system of excitons is investigated in terms of first-order correlation functions and analytic expressions for the coherence function are derived. It is argued that spatial coherence is inherent in

systems obeying Bose statistics due to their tendency to cluster together and does not necessarily require the existence of a BEC. In particular, in the experiments the PL signal is collected only from a small angle which corresponds to a narrow region in the k-space and therefore the coherence is rather imposed than measured.

CORRELATION FUNCTIONS

Let us consider excitons as a non-interacting gas of bosons with Hamiltonian

$$\hat{H} = \sum_{\mathbf{k}_\|} \varepsilon_{k_\|} \hat{B}^\dagger_{\mathbf{k}_\|} \hat{B}_{\mathbf{k}_\|} \quad ; \qquad \varepsilon_{k_\|} = \frac{\hbar^2 k_\|^2}{2M_\mathrm{x}} . \tag{4.1}$$

For simplicity, we describe the excitons in terms of a general bosonic field $\hat{\Psi}(\mathbf{r})$ which obeys the usual commutation relations

$$[\hat{\Psi}(\mathbf{r}_\|), \hat{\Psi}^\dagger(\mathbf{r}'_\|)] = \delta(\mathbf{r}_\| - \mathbf{r}'_\|) , \tag{4.2}$$

$$[\hat{\Psi}(\mathbf{r}_\|), \hat{\Psi}(\mathbf{r}'_\|)] = [\hat{\Psi}^\dagger(\mathbf{r}_\|), \hat{\Psi}^\dagger(\mathbf{r}'_\|)] = 0 , \tag{4.3}$$

where $\mathbf{r}_\|$ and $\mathbf{r}'_\|$ are the spatial coordinates of the excitons in the QW plane. To avoid overloading of the nomenclature we set $\mathbf{r}_\| = \mathbf{r}$ and $\mathbf{r}'_\| = \mathbf{r}'$ henceforth as well as $\mathbf{k}_\| = \mathbf{k}$, i.e., all vectors are understood to be two-dimensional since the excitons are confined to move along the quantum well plane.

If we choose plane waves as the basis, the creation and annihilation operators of the quantum field read

$$\hat{\Psi}^\dagger(\mathbf{r}) = \frac{1}{\sqrt{S}} \sum_k e^{-i\mathbf{k}\mathbf{r}} B^\dagger_\mathbf{k} , \tag{4.4}$$

$$\hat{\Psi}(\mathbf{r}') = \frac{1}{\sqrt{S}} \sum_k e^{i\mathbf{k}\mathbf{r}'} B_\mathbf{k} , \tag{4.5}$$

The first order correlation function is equivalent to the reduced one-particle density matrix which in the grand canonical ensemble is [21]

$$\hat{\rho} = \frac{1}{Z_\mathrm{G}} e^{-\beta(\hat{H} - \mu \hat{N})} , \tag{4.6}$$

where $\beta = 1/k_\mathrm{B}T$ is the Boltzmann factor, μ is the chemical potential ($\mu < 0$ for bosons) and Z_G is the grand canonical partition function. The translational invariance

of $\hat{\rho}$ implies that

$$\langle B_{\mathbf{k}}^{\dagger} B_{\mathbf{k}'} \rangle = Tr[\hat{\rho} \hat{B}_{\mathbf{k}}^{\dagger} \hat{B}_{\mathbf{k}'}] = \langle n_{\mathbf{k}} \delta_{\mathbf{kk}'} \rangle . \qquad (4.7)$$

One can then calculate the *first order correlation function* $G^{(1)}(\mathbf{r}, \mathbf{r}')$ of the system as

$$
\begin{aligned}
G^{(1)}(\mathbf{r}, \mathbf{r}') &= \langle \hat{\Psi}^{\dagger}(\mathbf{r}) \hat{\Psi}(\mathbf{r}') \rangle \\
&= Tr[\hat{\rho} \hat{\Psi}^{\dagger}(\mathbf{r}) \hat{\Psi}(\mathbf{r}')] \\
&= \frac{1}{S} \sum_{\mathbf{k}} e^{-i\mathbf{k}(\mathbf{r}-\mathbf{r}')} \langle B_{\mathbf{k}}^{\dagger} B_{\mathbf{k}'} \rangle .
\end{aligned}
\qquad (4.8)
$$

As we are interested in spatial coherence only, we consider the correlation function at equal times. Alternatively, the first-order correlation can be expressed in terms of the Wigner function

$$W(\mathbf{p}, \mathbf{r}) = \frac{1}{(2\pi\hbar)^2} \int d\mathbf{r}' e^{-i\mathbf{p}\mathbf{r}'/\hbar} \left\langle \hat{\Psi}^{\dagger}\left(\mathbf{r} - \frac{\mathbf{r}'}{2}\right) \hat{\Psi}\left(\mathbf{r} + \frac{\mathbf{r}'}{2}\right) \right\rangle \qquad (4.9)$$

which is the quantum-mechanical equivalent of a probability distribution in phase space. However, the Wigner function does not satisfy all the properties of a conventional probability distribution; for example it can become negative for states which have no classical analogue. Regions where the Wigner function takes negative values cannot extend to sizes larger than a few $\hbar$, as a consequence of the uncertainty principle which does not allow precise location within phase-space regions smaller than $\hbar$. Negative values of the Wigner function are related with quantum mechanical interference. The connection between the quantum-mechanical correlation function and statistical mechanics is illustrated by the Fourier transform relation

$$G^{(1)}(\mathbf{r}, \mathbf{r}') = \int d\mathbf{p}\, e^{-i\mathbf{p}(\mathbf{r}-\mathbf{r}')/\hbar} W\left(\mathbf{p}, \frac{\mathbf{r} + \mathbf{r}'}{2}\right) . \qquad (4.10)$$

In what follows the correlation function is calculated using Eq. (4.8) and is independently checked with application of Eq. (4.10). In order to achieve an absolute agreement between the two different approaches the local density approximation is applied.

COHERENCE FUNCTION

In order to define a local measure of coherence we introduce correlation functions which are normalised to attain unit modulus in the case of perfect coherence. In this

sense, the degree of first order coherence is expressed by

$$g^{(1)}(\mathbf{r}, \mathbf{r}') = \frac{G^{(1)}(\mathbf{r}, \mathbf{r}')}{\sqrt{G^{(1)}(\mathbf{r}, \mathbf{r})}\sqrt{G^{(1)}(\mathbf{r}', \mathbf{r}')}} \,. \tag{4.11}$$

$g^{(1)}$ characterises local fluctuations of the phase of the complex field amplitude and is related to the contrast in an interference experiment [172, 173]. In the following we examine both classical and quantum statistics for the mean value of the number operator $\langle B_{\mathbf{k}}^{\dagger} B_{\mathbf{k}} \rangle$.

CLASSICAL GAS

As a starting point, let us consider a 2D gas of particles obeying the Maxwell-Boltzmann (MB) distribution. This will serve as a reference point for further analysis. Substituting the MB distribution function into Eq. (4.8) and transforming the sum over $\mathbf{k}$ into an integral over the entire area in momentum space, one obtains

$$g_C^{(1)}(R) = e^{-\pi R^2 / \lambda_T^2} \,, \tag{4.12}$$

where R is the distance between the excitons under study, $R = |\mathbf{r} - \mathbf{r}'|$, and λ_T is the thermal de Broglie wavelength:

$$\lambda_T^2 = \frac{2\pi\hbar^2}{M_x k_B T} \,. \tag{4.13}$$

Thus, for a classical gas the coherence function has the form of a Gaussian and the correlations decay on a lengthscale given by the thermal wavelength. The coherence length defined in this way increases with decreasing temperature as Fig. 4.1 (a) illustrates.

QUANTUM GAS

Continuing in the same simple framework, i.e., the non-interacting case, let us now use the Bose-Einstein distribution to account for a degenerate gas of Bose particles above the critical temperature for BEC. Note that in our analysis the thermodynamic limit is considered where BEC cannot be realised at finite temperatures. In this case

the mean number of particles in the state with wavevector $\mathbf{k}$ is :

$$\langle B_{\mathbf{k}}^{\dagger} B_{\mathbf{k}} \rangle = \frac{z}{e^{\lambda^2 k^2} - z} , \qquad (4.14)$$

where $z = e^{\beta \mu}$ is the fugacity and $\lambda^2 = \lambda_T^2/4\pi$. For isotropically distributed QW excitons the first-order coherence function takes the form:

$$g^{(1)}(R) = \frac{1}{2\pi n_{2D}} \int_0^\infty J_0(kR) \, n_k \, k \, dk , \qquad (4.15)$$

where $R = |\mathbf{r} - \mathbf{r}'|$, n_{2D} is the concentration of particles, $n_{\mathbf{k}} = \langle B_{\mathbf{k}}^{\dagger} B_{\mathbf{k}} \rangle$ is the occupation number, and J_0 is the zeroth-order Bessel function of the first kind [174]. Using the expression for the chemical potential of a 2D gas of bosons

$$\mu_{2D} = k_B T \ln(1 - e^{-T_0/T}) , \qquad (4.16)$$

the occupation number can be rewritten as

$$\langle B_{\mathbf{k}}^{\dagger} B_{\mathbf{k}} \rangle = \frac{1 - e^{-T_0/T}}{e^{\lambda^2 k^2} + e^{-T_0/T} - 1} , \qquad (4.17)$$

i.e., in terms of the degeneracy temperature T_0, which is concentration dependent and therefore can be controlled by the external source in an actual experiment. The coherence function of a quantum degenerate Bose gas becomes in this case

$$g_Q^{(1)}(R) = \frac{2T}{T_0}(1 - e^{-T_0/T})\lambda^2 I(R) , \qquad (4.18)$$

where the integral is given by

$$I(R) = \int_0^\infty J_0(kR) \, n_k \, k \, dk \qquad (4.19)$$

and can be evaluated by expanding the occupation number in an infinite series according to:

$$\frac{x}{1 + \alpha x} = \sum_{n=0}^{\infty} (-1)^n \alpha^n x^{n+1} , \quad x \leq 1 , \qquad (4.20)$$

with $x = e^{-\lambda^2 k^2}$ and $\alpha = e^{-T_0/T} - 1$. Thus the integral becomes:

$$I(R) = \int_0^\infty \sum_{n=0}^{\infty} (-1)^n (e^{-T_0/T} - 1)^n e^{-(n+1)\lambda^2 k^2} k \, J_0(kR) \, dk . \qquad (4.21)$$

Exchanging the order of summation and integration the integral can be calculated analytically [174] and the final result is :

$$g_Q^{(1)}(R) = \frac{T}{T_0} \sum_{n=1}^{\infty} \frac{(1 - e^{-T_0/T})^n}{n} e^{-\pi R^2/n\lambda_T^2} , \qquad (4.22)$$

or in a more compact form

$$g_Q^{(1)}(R) = \frac{T}{T_0} g_1(z, g_C^{(1)}(R)) , \qquad (4.23)$$

where the generalised Bose function [175] was introduced

$$g_\alpha(x, y) = \sum_{k=1}^{\infty} \frac{x^k y^{1/k}}{k^\alpha} . \qquad (4.24)$$

It is already evident that for a gas which obeys quantum statistics, coherence is maintained for longer distances as the Bose function decays slower than a Gaussian. However, the degree of correlation does not depend only on temperature but also on the density of the excitons through T_0. This means that apart from the thermal fluctuations the exciton gas is influenced by the quantum fluctuations as well. Fig. 4.1(b) shows the effect of temperature on the coherence function where – similar to the classical case – an increase of the coherence length is expected at low bath temperatures. The asymptotic behaviour of $g^{(1)}$ is of major importance in the study of the coherence of the system and is analysed in detail in the following Section.

4.2 ASYMPTOTIC BEHAVIOUR OF THE COHERENCE FUNCTION

CLASSICAL LIMIT $T \gg T_0$

When the temperature is well-above the quantum degeneracy temperature, i.e., when the exciton density is sufficiently low, the coherence function approaches the Gaussian of the classical gas and the coherence length will be given by the de Broglie wavelength. Indeed if in Eq. (4.22) one keeps only the term for $n = 1$ and writes the exponential
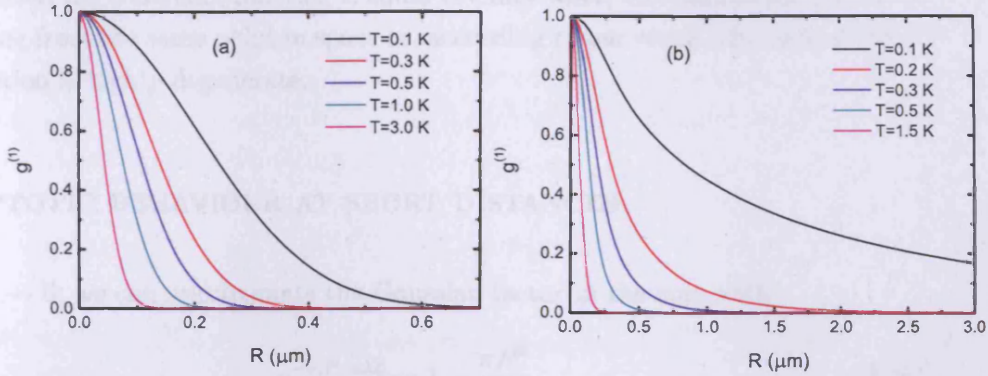
Figure 4.1: The first-order spatial coherence function as a function of the spatial separation for (a) MB and (b) BE distributed excitons. The increase of the coherence length with decreasing temperature is evident. For classical statistics the lengthscale of correlations is set by the de Broglie wavelength and exhibits a Gaussian decay, whereas in the case of quantum statistics coherence is preserved for longer distances and decays exponentially.

as $e^{-T_0/T} \simeq 1 - T_0/T$ one obtains:

$$g_Q^{(1)}(R) = \frac{T}{T_0}(1 - 1 + \frac{T_0}{T})e^{-\pi R^2/\lambda_T^2} = g_C^{(1)}(R). \qquad (4.25)$$

As one would expect, in the limit of high temperatures the quantum expression reproduces the classical result. Let us note however that apart from the temperature, what characterises the classical limit is the sum index n since when T is high and therefore λ_T is small, the contribution of terms with $n \neq 1$ is negligible.

QUANTUM LIMIT $T \ll T_0$

In the opposite limit when $T \to 0$ the exponential approaches unity and the coherence function takes the form

$$g_Q^{(1)}(R) = \frac{T}{T_0}\sum_{n=1}^{\infty}\frac{(1 - e^{-T_0/T})^n}{n} = \frac{T}{T_0}\frac{T_0}{T} = 1, \qquad (4.26)$$

where we have used

$$\sum_{n=1}^{\infty}\frac{x^n}{n} = -\ln(1 - x). \qquad (4.27)$$

By definition the coherence function is equal to unity when we examine matter waves originating from the same point in space or, according to our result, the system under investigation is highly degenerate.

ASYMPTOTIC BEHAVIOUR AT SHORT DISTANCES

When $R \to 0$, we can approximate the Gaussian factor in the sum with

$$e^{-\pi R^2/n\lambda_T^2} = 1 - \frac{\pi R^2}{n\lambda_T^2} . \tag{4.28}$$

In this case the coherence function close to $R = 0$, $i.e.$, when the distance between the two excitons is very small, becomes:

$$g_Q^{(1)}(R) = 1 - \frac{T}{T_0}\frac{\pi R^2}{n\lambda_T^2}\mathrm{Li}_2(1 - e^{-T_0/T}) , \tag{4.29}$$

where the polylogarithm function is defined as:

$$\mathrm{Li}_\alpha(x) = \sum_{k=1}^{\infty} \frac{x^k}{k^\alpha} . \tag{4.30}$$

As a result when $R \ll \lambda_T$ the coherence function decays as

$$g_Q^{(1)}(R) \sim 1 - \frac{\pi R^2}{\lambda_T^2} , \tag{4.31}$$

which is consistent with the classical limit. Excitons with small spatial separation inherit the coherence properties of the laser beam which generates them and as a consequence they tend to be coherent with each other.

ASYMPTOTIC BEHAVIOUR AT LARGE DISTANCES

The previous results although trivial show that the general expression (4.22) reproduces the anticipated behaviour at various limits. However, it is less clear how very distant excitons are correlated. In this case, the value of the coherence function is of utmost importance for technological applications as it can provide one with information about the intrinsic limitations of coherence transfer in these systems. In order to analyse the coherence for large R we substitute the sum in

Eq. (4.22) with an integral, change variables according to $x = 1/n$ and set the upper limit of integration to be equal to infinity. This substitution is satisfied as long as $R \gtrsim R^{(q)} = \lambda_T \left[- (2/\pi) \ln(1 - e^{-T_0/T}) \right]^{1/2}$ since then the difference between successive terms in the sum is small and it can be transformed into an integral. In this limit the coherence function reduces to

$$g^{(1)}\left(R \gtrsim R^{(q)}\right) \simeq 2\frac{T}{T_0}K_0\left(\frac{R}{R_0}\right), \qquad (4.32)$$

where K_0 is the modified Bessel function of the second kind [176] and $R_0 = \lambda_T/[-4\pi \ln(1 - e^{-T_0/T})]^{1/2}$.

For $R \gg R_0 \gtrsim R^{(q)}$, Eq. (4.32) reduces further to the quantum limit:

$$g^{(1)} = g_q^{(1)}(R \gg R_0) = \sqrt{2\pi}\,\frac{T}{T_0}\sqrt{\frac{R_0}{R}}\,e^{-R/R_0}. \qquad (4.33)$$

The quantum corrections given by Eq. (4.33) refer to $R \gtrsim \lambda_T \sqrt{(2/\pi)\ln(T/T_0)} \gg \lambda_T$, and, therefore, to very small values of $g^{(1)}$. The latter conclusion is consistent with the $e^{-\pi R^2/n\lambda_T^2}$ – series on the r.h.s. of Eq. (4.22). For $T \lesssim T_0$, when Bose-Einstein statistics is well-developed, Eq. (4.33) is valid for distances larger than $\lambda_T \sqrt{(2/\pi)}\,e^{-T/2T_0} \ll \lambda_T$, so that $g^{(1)}$ is well-approximated by $g_q^{(1)}$ for any R.

Thus, with temperature T decreasing from $T \gg T_0$ to $T \lesssim T_0$, the first-order coherence function $g^{(1)}$ changes from the n_{2D}-independent Gaussian $g_C^{(1)}(R)$, to the n_{2D}-dependent exponentially decaying $g_q^{(1)}(R)$. The quantum statistical effects considerably increase the correlation length ξ_x, as illustrated in Fig. 4.1. For $T \lesssim T_0$ one has $\xi_x \sim r_0 \simeq [\lambda_T/(2\sqrt{\pi})]e^{T_0/2T}$, i.e., ξ_x increases exponentially with increasing density n_{2D}. This is due to large non-classical population of the low-energy states, in particular the ground-state mode $\mathbf{k} = 0$: $n_{k=0}^{BE} = e^{T_0/T} - 1$.

4.3 INCLUSION OF THE DIPOLE-DIPOLE INTERACTION

Our analysis so far was restricted to the general case of two-dimensional bosons. Indirect excitons can be considered as such only in the dilute limit $a_0^2 n_{2D} \ll 1$. As the concentration increases through laser excitation the interactions which come into play are expected to limit the coherence in the excitonic gas. Moreover, the composite

nature of excitons has to be taken into account when the system becomes dense enough. The interaction between indirect excitons changes with increasing density from the dipole-dipole repulsion of the aligned dipoles to Coulomb interaction between their constituents. In this Section we calculate within the self-consistent Hartree-Fock approximation the corrections to the exciton energy due to this repulsion and show analytically how this inclusion influences the spatial correlations. The main result is that the interaction induces an increase of the effective mass which now depends upon the parameters of the structure and the temperature. A direct consequence of this increase is that coherence is maintained for shorter distances than in the non-interacting case and therefore the coherence length decreases, remaining however larger than that of the classical gas.

GREEN'S FUNCTION

In interacting systems when many-body effects are taken into account, the natural generalisation of a correlation function is the Green's function between two operators. These propagators describe the evolution of a system from a given initial state through the interaction potential which induces scattering processes. The Hamiltonian of a two-dimensional system of interacting bosonic particles in the second quantisation formalism has the form

$$\hat{H} - \mu\hat{N} = \sum_{\mathbf{k}}(\varepsilon_{\mathbf{k}} - \mu)B_{\mathbf{k}}^{\dagger}B_{\mathbf{k}} + \frac{1}{2S}\sum_{\mathbf{k},\mathbf{k}',\mathbf{q}}v(\mathbf{q})B_{\mathbf{k}+\mathbf{q}}^{\dagger}B_{\mathbf{k}'-\mathbf{q}}^{\dagger}B_{\mathbf{k}'}B_{\mathbf{k}}, \qquad (4.34)$$

and the corresponding Green's function of two operators A and B is defined as

$$G_{A,B}(z) = \frac{1}{Z}\sum_{m,n}(e^{\beta E_m} - e^{\beta E_n})\frac{\langle m|A|n\rangle\langle n|B|m\rangle}{z - E_n - E_m}, \qquad (4.35)$$

where the orthonormal basis $|m,n\rangle$ is constructed by the eigenstates of the Hermitian operator $\hat{H} - \mu\hat{N}$, with corresponding energies $E_{m,n}$, Z is the partition function and z is in general a complex number which is chosen with respect to the particular type of the Green's function one wants to study. For the purposes of the present analysis we choose $z \to i\omega_l$ and the resulting thermal Green's function is related with the correlation function through

$$\langle BA \rangle = -\frac{1}{\beta}\sum_{l}e^{i\omega_l\eta}G_{A,B}(i\omega_l). \qquad (4.36)$$

Here, the summation is performed over the bosonic Matsubara frequencies $\omega_n = 2\pi n/\beta$ and then the limit $\eta \to 0+$ is taken.[1] Equation (4.36) can be considered as a form of the fluctuation-dissipation theorem: the correlation function describes the spontaneous quantum fluctuations of the system in thermal equilibrium with characteristic frequency ω, while the Green's function characterises the response of the system to an external perturbation. In the case of a system described by the Hamiltonian (4.34) the Green's function is calculated adopting a perturbative approach through the equation of motion written in the form:

$$G_\alpha(z) = G_\alpha^{(0)}(z) + G_\alpha^{(0)}(z)\Sigma_\alpha^{(0)}(z)G_\alpha(z)\,, \tag{4.37}$$

where $G_\alpha^{(0)}(z)$ is the Green's function of the corresponding non-interacting system

$$G_\alpha^{(0)}(z) = \frac{1}{z - \varepsilon_\alpha - \mu}\,, \tag{4.38}$$

and the *self-energy* $\Sigma_\alpha(z)$ includes all the corrections to the single-particle Green's function, *i.e.*, all the irreducible scattering processes. Thus the Green's function of the interacting system is specified by means of Dyson's equation

$$G_\alpha(z) = \frac{1}{z - (\varepsilon_\alpha - \mu) - \Sigma_\alpha(z)}\,. \tag{4.39}$$

In general, the calculation of a single-particle Green's function involves two-particle Green's function and therefore a decoupling approximation is in order. For the purposes of the present analysis the Hartree-Fock approximation is sufficient as we describe in the next subsection.

HARTREE-FOCK APPROXIMATION

In several physical systems the motion of single particles can be considered to take place in the average self-consistent field generated by all the other particles. This idea is behind the Hartree-Fock approximation which is characterised by a Dyson equation of the form

$$G(\mathbf{k}, i\omega_n) = \frac{1}{i\omega_n - \varepsilon_\mathbf{k} + \mu - \Sigma_{\mathrm{HF}}(\mathbf{k})} \tag{4.40}$$

---

[1]Note that the presence of the prefactor assures that the corresponding ω_n-sum converges.

with the self-energy given by

$$
\begin{aligned}
-\beta\Sigma_{HF}(\mathbf{k}, i\alpha) &= \sum_{\mathbf{q}, \eta} \left[-\frac{\beta v(\mathbf{q})}{S} \right] \left[-\frac{1}{\beta} G_\alpha^{(0)}(\mathbf{k} - \mathbf{q}, i\alpha - i\eta) \right] e^{i(\alpha - \eta)0^+} \\
&= -\frac{1}{S} \sum_{\mathbf{q}} v(\mathbf{q}) \frac{1}{\beta} \sum_{\alpha'} G_\alpha^{(0)}(\mathbf{k} - \mathbf{q}, i\alpha') e^{i\alpha'0^+},
\end{aligned}
\tag{4.41}
$$

where $\alpha' = \alpha - \eta$. The effect of the mean field potential is a renormalization of the single-particle energies according to

$$
\tilde{\varepsilon}_{\mathbf{k}} = \varepsilon_{\mathbf{k}} + \frac{1}{S} \sum_{\mathbf{k}'} \langle B\mathbf{k}'^\dagger B\mathbf{k}' \rangle [v(0) + v(|\mathbf{k} - \mathbf{k}'|)]
\tag{4.42}
$$

with corresponding Green's function

$$
G(k, i\omega_n) = \frac{1}{i\omega_n - \tilde{\varepsilon}_{\mathbf{k}} + \mu}.
\tag{4.43}
$$

In other words in the Hartree-Fock approximation a system of interacting particles behaves as a system of non-interacting quasi-particles with energy $\tilde{\varepsilon}_{\mathbf{k}}$ and infinite lifetime.

Note that an essential prerequisite for the choice of Hartree-Fock approximation for bosons is a high temperature value so as to avoid any condensation in the ground state mode. Indeed this assumption is included in our approach where the thermodynamic limit is considered and the system is two-dimensional. Furthermore, in all of our simulations the temperature is kept above the Berezinskii-Kosterlitz-Thouless (BKT) limit where superfluidity spontaneously develops.

DIPOLE INTERACTION POTENTIAL

Let us consider the case of an ideal double quantum well without impurities and neglect the effect of interface roughness. In such a structure indirect excitons are represented by identical dipoles free to move in the x-y plane and polarised along the z direction which coincides with the growth direction. The dominant interaction between these Bose particles is the dipole-dipole repulsion as long as the system is dilute, such that higher multipolar fields are weak. However, a more rigorous potential should include the interaction between the constituent electrons and holes, since their separation is finite. We can therefore exploit a phenomenological approach, where the

interaction becomes Coulomb-like at short distances, while preserving asymptotically a dipolar character. In this sense the interaction can be described by means of the potential [177]

$$v(r) = \frac{p^2}{r^3}\left(1 - e^{-r^2/d^2}\right),$$ (4.44)

with d being the distance where excitons start to feel each other's internal structure and p the magnitude of the dipole strength. A great advantage of this particular choice of potential is that it has a well-defined 2D Fourier transform, which can furthermore be calculated analytically:

$$v(q) = \frac{qp^2}{2\pi}\left\{\frac{qd\sqrt{\pi}}{4}e^{-q^2d^2/8}\left[I_1\left(\frac{q^2d^2}{8}\right) + \left(1 + \frac{4}{q^2d^2}\right)I_0\left(\frac{q^2d^2}{8}\right)\right] - 1\right\},$$ (4.45)

where I_n is the modified Bessel function of the first kind of nth order [176]. Equation (4.45) can be further simplified by taking the Taylor expansions of both Bessel functions and the exponential and keeping only the leading terms, i.e., imposing the condition $qd \ll 1$. This requirement is equivalent to the cancellation of the long-wavelength limit of the interaction potential which in turn is a consequence of the assumption of a *fixed* average dipole density. The physical meaning of this constraint is that the system of indirect excitons is characterised by charge neutrality and therefore a local increase – or decrease – of the dipole density results in an effective restoring force allowing one to define an average density. In view of these considerations the interaction potential in the momentum space becomes

$$v(q) = v_0\left(\frac{d^2}{8}q^2 - \frac{d}{\sqrt{\pi}}q + 1\right),$$ (4.46)

where $v_0 = v(q \to 0) = p^2/2d\sqrt{\pi}$, is the zeroth order term and in numerical calculations will be chosen to agree with the experimental results. The interaction brings about a change in the exciton energy and chemical potential. This change is calculated self-consistently within the Hartree-Fock scheme in the following Section.

4.3.1   SELF-CONSISTENT HARTREE-FOCK THEORY

In the self-consistent Hartree-Fock approximation we can calculate the correlation function using the exciton's Green's function given by the Dyson equation

$$G(\mathbf{k}, i\omega_n) = \frac{1}{i\omega_n - \varepsilon_{\mathbf{k}} + \mu - \Sigma_{\mathrm{SCHF}}(\mathbf{k}, i\omega_n)},$$ (4.47)

with the self-energy after the summation over the bosonic Matsubara frequencies
being

$$\Sigma_{\text{SCHF}}(\mathbf{k}, i\omega_n) = -\frac{1}{S} \sum_{\mathbf{k}'} v(\mathbf{k} - \mathbf{k}') \langle n_{\mathbf{k}'} \rangle_0 \,. \tag{4.48}$$

The occupation number has to be calculated self-consistently using

$$\langle n_{\mathbf{k}'} \rangle_0 = \frac{1}{e^{\beta(\tilde{\varepsilon}_{\mathbf{k}'} - \mu)} - 1} \,. \tag{4.49}$$

The self-energy consists of a part which depends quadratically on the wavevector and
a part which has no momentum dependence but is only a function of the density,
temperature and the parameters of the potential, namely

$$
\begin{aligned}
\Sigma_{\text{SCHF}}(k) &= v_0 n_{\text{2D}} + \frac{v_0}{16\pi} \left[\left(\frac{d^2}{2\lambda^2} \frac{T_0^*}{T} - \frac{d}{\lambda} \text{Li}_{1/2}(\text{F}) \right) k^2 \right. \\
&\quad + \left. \frac{1}{\lambda^2} \left(\frac{d^2}{2\lambda^2} \text{Li}_2(\text{F}) - \frac{2d}{\lambda} \text{Li}_{3/2}(\text{F}) + \frac{4T_0^*}{T} \right) \right]
\end{aligned}
\tag{4.50}
$$

where $T_0^* = (M_{\text{x}}/M_{\text{x}}^*)T_0$, $\text{F} = 1 - e^{T_0^*/T}$ and the polylogarithm function $\text{Li}_\alpha(x)$ was
used. This form of the self-energy implies that the effects of the interaction can be
incorporated in a renormalised effective mass and a shifted chemical potential. The
mean occupation number of the dipole-dipole interacting excitons takes the form

$$\langle B_{\mathbf{k}}^\dagger B_{\mathbf{k}} \rangle = -\frac{1}{\beta} \sum_n e^{i\omega_n \eta} \frac{1}{i\omega_n - \tilde{\varepsilon}_{\mathbf{k}} + \tilde{\mu}} \,, \tag{4.51}$$

where again the sum is over the bosonic Matsubara frequencies $\omega_n = 2\pi n/\beta$ with

$$\tilde{\varepsilon}_{\mathbf{k}} = \frac{\hbar^2 k^2}{2M_{\text{x}}^*} \tag{4.52}$$

and

$$\tilde{\mu} = \mu + \frac{v_0}{4\pi\lambda^2} \left[\frac{T_0^*}{T} + \frac{d}{\lambda} \left(\frac{d}{8\lambda} \text{Li}_2(\text{F}) - \text{Li}_{3/2}(\text{F}) \right) \right] \,. \tag{4.53}$$

The effective mass is determined as a single solution of the transcendental equation

$$\frac{1}{M_{\text{x}}^*} = \frac{1}{M_{\text{x}}} + \frac{v_0}{8\pi\hbar^2} \frac{d}{\lambda} \left[\frac{d}{2\lambda} \frac{T_0^*}{T} - \text{Li}_{1/2}(1 - e^{-T_0^*/T}) \right] \tag{4.54}$$

or

$$u + A\, u^{-1/2} \sqrt{T}\, \text{Li}_{1/2}(1 - e^{-Bu\ n_{\text{2D}}/T}) = 1 + C\, n_{\text{2D}} \,, \tag{4.55}$$
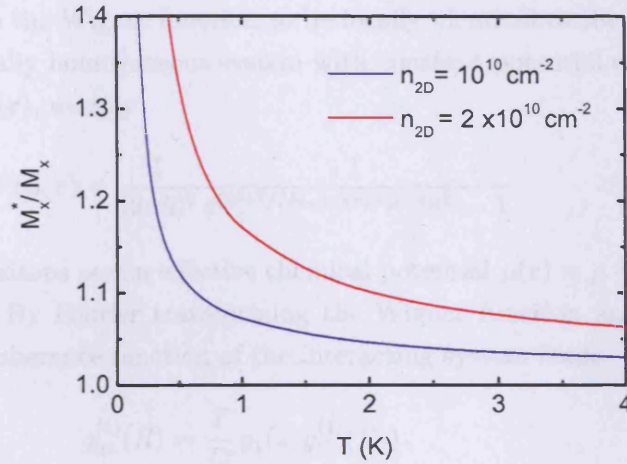
Figure 4.2: The change of the effective mass with decreasing temperature for two values of the concentration calculated within the Hartree-Fock approximation. At low temperatures where quantum effects are dominant the effective mass increases rapidly, influencing the spatial correlations which are limited.

where $u = M_x/M_x^*$, $\lambda^2 = \hbar^2/2M_x^* k_B T$ and A, B and C are numerical factors. Figure 4.2 shows the dependence of the renormalised effective mass on the temperature for two values of the concentration. At temperatures below $1\,\mathrm{K}$ there is a large increase of the mass which stems from its dependence on the thermal wavelength. As the system enters the quantum regime the dipole-dipole interaction alters excitons behaviour to that of much heavier particles. The effect of the concentration is also evident: higher values of the concentration result in reduction of the mean distance between particles and therefore a stronger interaction between them which again increases the effective mass. This effect may be an obstacle towards the achievement of BEC in a system of indirect excitons as it seems that in the region of a few K there is an increase of the effective mass requiring lower temperatures for the observation of collective phenomena. However, the Hartree-Fock approximation is no longer valid in the critical regime where one has to consider the macroscopic occupation of the ground state. Furthermore, the choice of the interaction potential was made in phenomenological grounds and reproduces only qualitatively the studied physical system.

The coherence function of the interacting system can be calculated in terms of the Wigner function which, as mentioned before, is employed in the local density approximation. This assumes the Wigner function to be locally identical to the momentum distribution of a spatially homogeneous system with constant potential energy equal to the local value of $v(\mathbf{r})$, namely

$$W(\mathbf{p}, \mathbf{r}) = \frac{1}{(2\pi\hbar)^2} \frac{1}{e^{(\hbar^2 k^2/2M_x + v(\mathbf{r}) - \mu)/k_B T} - 1} \tag{4.56}$$

In other words, the excitons see an effective chemical potential $\mu(\mathbf{r}) = \mu - v(\mathbf{r})$ which varies with position. By Fourier transforming the Wigner function and using the definition (4.11) the coherence function of the interacting system reads

$$g_{\text{int}}^{(1)}(R) = \frac{T}{T_0^*} g_1(z, g_C^{(1)}(R)). \tag{4.57}$$

Hence, it is evident that the influence of the interactions can be incorporated in a renormalisation of the effective mass and shifting of the effective chemical potential.

The main motivation for the inclusion of the interaction between indirect excitons was to explore its consequences on the correlations between the particles. The increase of the mass implies that correlations should decay faster as it would be natural for more massive particles. Indeed, as Fig. 4.4 shows, the coherence function for the interacting system lies between those for the classical and non-interacting cases in the temperature regime where the effective mass increases. For higher temperatures however all three curves nearly coincide. It is also noteworthy that although the distance where correlations are maintained is limited, the exponential asymptotic behaviour is preserved even when the particles interact. This is illustrated in Fig. 4.3 where both the exponential decay and the increase of the coherence function with decreasing temperature are clearly identified.

The corresponding coherence lengths for the two cases are presented in Fig. 4.5 as a function of temperature. Here the coherence length is defined as the distance where the coherence function drops to the half of its maximum, i.e., equals to 1/2. For realistic parameters the coherence length in the interacting case is less than half of the non-interacting one at low temperatures. As the temperature increases the two curves coincide in accordance with the coincidence of the coherence functions in Fig. 4.4 still remaining well below 1μm. However, the large increase of the coherence length observed in recent experiments in systems of indirect excitons and microcavity
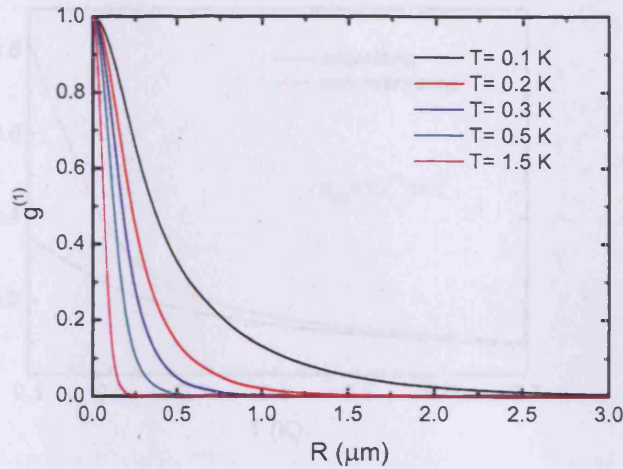
Figure 4.3: The first-order spatial coherence function $g^{(1)}$ for a bosonic exciton gas with dipole-dipole repulsion taken into account in the self-consistent Hartree-Fock approximation. The interactions induce an increase of the effective mass destroying coherence faster than in the non-interacting case. However, the increase of coherence length with decreasing temperature as well as the exponential decay at large spatial separations are maintained even in the interacting case.
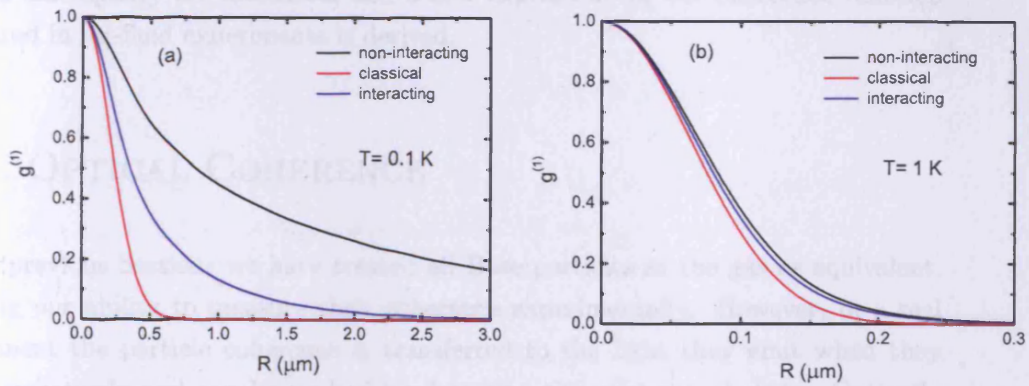
Figure 4.4: Comparison of the coherence function for a classical, non-interacting and dipole-dipole interacting Bose gas at (a) T=0.1 K and (b) T=1 K. At high temperatures the three coherence functions nearly coincide but as the temperature is lowered the quantum effects become important and the coherence length increases considerably.
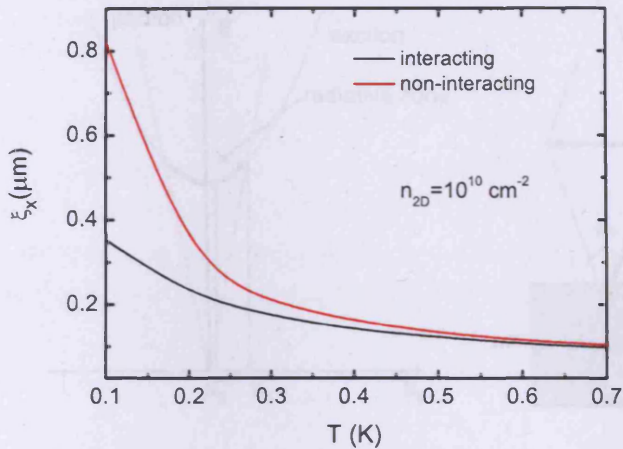
Figure 4.5: The coherence length increases with decreasing temperature. The effect is less pronounced in the case of interacting particles as scattering processes destroy the coherence of excitons. Although the two cases are indistinguishable at temperatures around $1\,\mathrm{K}$, the coherence length of interacting particles is half of that of non-interacting particles at temperature of hundreds of mK.

polaritons is far from the values calculated here. In the next Section the reasons for this discrepancy are discussed, and a new expression for the coherence function measured in far-field experiments is derived.

4.4 OPTICAL COHERENCE

In the previous Sections we have treated all Bose particles in the gas as equivalent, ignoring our ability to measure their coherence experimentally. However, in a real experiment the particle coherence is transferred to the light they emit when they decay radiatively and can be probed by detecting the coherent photons. Optically inactive states do not contribute to the emitted radiation and therefore they have to be excluded. Thus, only those excitons whose momentum lies inside the photon cone contribute to the detected signal. In addition, in far-field optical experiments with detection angle 2α the fraction of QW excitons which contribute to the optical signal is further reduced to a very narrow band in k-space. In order to include this effect

(a)

photon E   exciton

radiative zone

$k_\parallel^{(\alpha)}$ k_0 $k_\parallel$

(b)

detector

2α

$k^{(\alpha)}$

$k_\parallel^{(\alpha)}$

QW
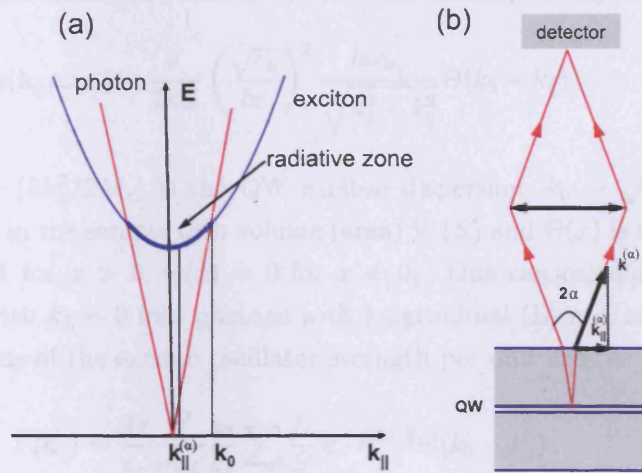
Figure 4.6: Schematic illustration of the $k_\parallel$-filtering effect. (a) The exciton and photon dispersions. Only low-energy QW excitons from the radiative zone $k_\parallel \leq k_0$ can emit outgoing bulk photons. (b) A far-field optical experiment with detection angle 2α: A small fraction of QW excitons with $k_\parallel \leq k_\parallel^{(\alpha)} = (k_0/\sqrt{\varepsilon_b})\sin\alpha$ contributes to the optical signal.

in the correlation functions the concept of $k_\parallel$-*filtering* is introduced and analysed. This modification has a huge impact on the measured coherence length as it is shown below.

4.4.1 RADIATIVE LIFETIME OF QW EXCITONS

In bulk crystals, due to conservation of the crystal momentum the interaction of free excitons with the electromagnetic field does not give rise to radiative decay of the excitons, but rather to hybrid stationary states called exciton polaritons. However, in quantum wells the breaking of translational invariance in the growth direction allows the coupling of free excitons with a continuum of photon states since conservation of the crystal momentum is suppressed. As a result radiative decay becomes possible for excitons lying below the crossing with the photon line, *i.e.*, with centre-of-mass in-plane wavevector $k_\parallel \leq k_0 = (\sqrt{\varepsilon_b}/c)\omega_0$, with ε_b the dielectric constant of the hosting material, $\hbar\omega_0$ the exciton energy at $k_\parallel = 0$ and c the *in vacuo* speed of light. The dipole interaction couples excitons with wavevector $\mathbf{k}_\parallel$ with bulk photons with the same in-plane wavevector but with all possible values of k_z, where z coincides with

the growth direction. Hence, the density of states for radiative decay is given by

$$\rho(\mathbf{k}_\|, \omega_{\mathbf{k}_\|}) = \frac{V}{2\pi S} \left(\frac{\sqrt{\varepsilon_b}}{\hbar c} \right)^2 \frac{\hbar \omega_{\mathbf{k}_\|}}{\sqrt{k_0^2 - k_\|^2}} \Theta(k_0 - k_\|), \tag{4.58}$$

where $\omega_{\mathbf{k}_\|} = \omega_0 + (\hbar k_\|^2 / 2M_x)$ is the QW exciton dispersion, $k_0 = \sqrt{\varepsilon_b}\omega/c$ is the wavevector of light in the sample with volume (area) V (S) and $\Theta(x)$ is the Heaviside function $[\Theta(x) = 1$ for $x > 0$, $\Theta(x) = 0$ for $x < 0]$. One can calculate the decay rates of excitons with $k_\| = 0$ into photons with longitudinal (L) and transverse (T) polarisation in terms of the exciton oscillator strength per unit area as $f_{\hat{\varepsilon}}/S^2$

$$\Gamma(\mathbf{k}_\|) = \frac{2\pi}{\varepsilon_b} \frac{e^2}{m_0 c} \frac{k_0}{k_z} \sum_\lambda \frac{f_{\hat{\varepsilon}}}{S} |\hat{e} \cdot \hat{\epsilon}^{(\lambda)}|^2 \Theta(k_0 - k_\|), \tag{4.59}$$

where $k_z = \sqrt{k_0^2 - k_\|^2}$ and $\hat{e}$ and $\hat{\epsilon}^{(\lambda)}$ are the exciton and photon polarisation vectors, respectively. If we define the oscillator strength for in-plane polarisation as

$$f_{xy} = \sum_\lambda f_{\hat{\varepsilon}} |\hat{e} \cdot \hat{\epsilon}^{(\lambda)}|^2 \tag{4.60}$$

the radiative widths for the T- and L-modes read:

$$\Gamma_{\mathrm{T}}(\mathbf{k}_\|) = \Gamma_0 \frac{k_0}{\sqrt{k_0^2 - k_\|^2}} \tag{4.61}$$

$$\Gamma_{\mathrm{L}}(\mathbf{k}_\|) = \Gamma_0 \frac{\sqrt{k_0^2 - k_\|^2}}{k_0}. \tag{4.62}$$

Equations (4.61) and (4.62) imply that at $\mathbf{k}_\| = 0$ both L- and T-modes have the same intrinsic radiative decay rate $\Gamma_0 = (2\pi e^2/(\sqrt{\varepsilon_b}m_0 c))(f_{xy}/S)$. The efficiency of the resonant conversion of a QW exciton in an outgoing bulk photon is given by the sum of Γ_{T} and Γ_{L}

$$\Gamma_{x-\gamma}(k_\|) = \frac{2k_0^2 - k^2}{k_0^2 \sqrt{k_0^2 - k^2}}. \tag{4.63}$$

Thus, in calculating the coherence function of decaying excitons one should multiply their distribution by Eq. (4.63) in order to account only for those excitons participating in the recombination process.

---

[2]For the Z polarization the oscillator strength vanishes for the heavy-hole exciton and therefore its decay rate is zero for all $k_\|$

In PL experiments the light is collected within an angle α from the normal which reflects the distribution of excitons in momentum space. We consider $1° \leq \alpha \leq 20°$, a selection which covers all practical applications. The maximum wavevector is related to this angle through

$$k_{\text{max}}^{(\alpha)} = \frac{k_0}{\sqrt{\varepsilon_b}} \sin \alpha \,, \tag{4.64}$$

with $k_0 = 2.85 \times 10^5 \text{cm}^{-1}$ and $\varepsilon_b = 12.9$ the dielectric constant of the barrier layers. Therefore the maximum wavevector lies in the region $0.004 \, k_0 \leq k_{\text{max}}^{(\alpha)} \leq 0.09 \, k_0$. With increasing the angle of collection the coherence length decreases dramatically as it is shown in the following Section.

4.4.2   OPTICAL COHERENCE FUNCTION

As mentioned above, in order to account for the radiative exciton states that are the ones probed in an actual PL experiment we need when calculating correlation functions to perform the integrations up to k_{max} and multiply by a k-dependent prefactor which describes the proper fraction of excitons, $i.e.$, those who have momentum inside the photon cone. In this case the coherence function takes the form

$$\tilde{g}^{(1)}(R) = \frac{\int_0^\infty G_f(k) J_0(kR) \, n_k \, k \, dk}{\int_0^\infty G_f(k) \, n_k \, k \, dk} \,, \tag{4.65}$$

where $G_f = \Theta(k^{(\alpha)} - k)\Gamma_{x-\gamma}(k)$ is the $k_\parallel$-filtering function with $\Theta(x)$ the step function and $\Gamma_{x-\gamma}(k)$ the efficiency of the resonant conversion of a QW exciton in an outgoing bulk photon given by Eq. (4.63). The function G_f reduces the integration limits on the right-hand side of Eq. (4.65) to a narrow band $\Delta k = [0, k^{(\alpha)}]$ and describes the $k_\parallel$-filtering effect in high-quality planar nanostructures. If both the function $\Gamma_{x-\gamma}(k)$ and the occupation number n_k do not change significantly in the narrow band Δk, Eq. (4.65) reduces to

$$\tilde{g}^{(1)} = \tilde{g}_f^{(1)}(R) = 2J_1(k^{(\alpha)}R)/(k^{(\alpha)}R) \,, \tag{4.66}$$

where J_1 is the first-order Bessel function of the first kind. From Eq. (4.66) one concludes that the optical coherence length ξ_γ, evaluated as the half width at half maximum of $\tilde{g}^{(1)} = \tilde{g}_f^{(1)}(R)$, is given by

$$4J_1(k^{(\alpha)}\xi_\gamma) = k^{(\alpha)}\xi_\gamma \quad \rightarrow \quad k^{(\alpha)}\xi_\gamma \simeq 2.215 \,. \tag{4.67}$$
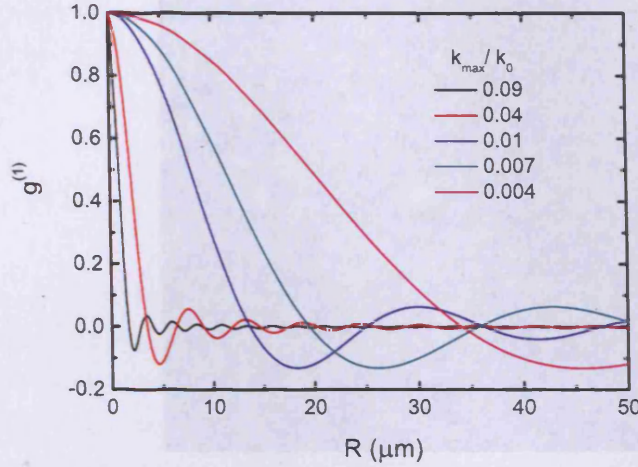
Figure 4.7: The optical coherence function for different values function of the maximum wavevector which reflects the angle of collection in a far-field experiment. The coherence is preserved for macroscopically large distances and the damped oscillatory behavior is a consequence of the sharp cutoff in k-space and the interference produced by the coherent excitons.

Equations (4.66)-(4.67) illustrate the net $k_\parallel$-filtering effect: $\xi_\gamma \propto 1/k^{(\alpha)} \propto 1/\sin\alpha$ strongly increases with decreasing aperture angle α.

Equation (4.65) can be expressed as a function of the maximum wavevector if both the Bose-Einstein distribution (see Eq. (4.20)) and the Bessel function are rewritten in a series representation

$$J_0(z) = \sum_{k=0}^{\infty} \frac{(-\frac{1}{4}z^2)^k}{(k!)^2}. \tag{4.68}$$

Substitution in Eq. (4.65) and integration of the numerator and the denominator yields the analytical expression

$$\bar{g}^{(1)}(R) = \frac{1}{\ln[1 - e^{k_{max}^2 \lambda^2} F] + \frac{T_0}{T}} \left[g^{(1)}(R) - \sum_{n=1}^{\infty} \frac{F^n}{n} \sum_{m=0}^{\infty} \left(-\frac{R^2}{4n\lambda^2} \right)^m \frac{\Gamma(m+1, k_{max}^2 \lambda^2 n)}{(m!)^2} \right] \tag{4.69}$$

where Γ is the incomplete Gamma function.
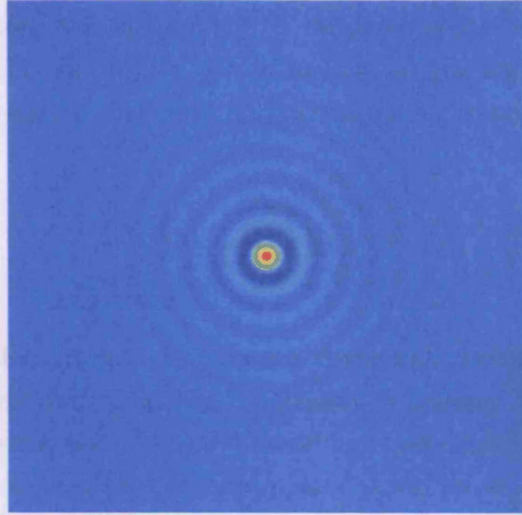
Figure 4.8: A real space image of the optical coherence function. The radially symmetric coherence function produces an interference pattern. The red colour corresponds to perfect coherence then yellow and green represent decreasing values of the coherence function, light and dark blue coincide with the zeros and negative values of the coherence function respectively.

As the angle of collection and hence the maximum wavevector decreases, the coherence in the exciton system is preserved for macroscopically large distances. The effect of temperature is also important: at temperatures ten times lower than the degeneracy temperature a huge increase of the coherence length is observed. Comparing to the case were no $k_\parallel$-filtering is taken into account, a rather oscillating than exponential decay behaviour of the coherence function is found. This feature is reminiscent of the Friedel oscillations in a Fermi liquid which are produced due to the sharp Fermi surface and the discontinuities in the dielectric function [178]. Similarly the sharp cutoff at $k_\parallel = k_\parallel^{(\alpha)}$ produces the damped oscillatory behavior of $\tilde{g}^{(1)}$ with $k_\parallel^{(\alpha)}$ akin to the Fermi wavevector k_F. The negative values of the coherence function originate from the regions where the Wigner function becomes negative and reflect the interference of the matter waves. In fact the two-dimensional illustration of the coherence function is similar to an interference pattern in a Young's double slit experiment (see Fig. 4.8).

We conclude that the $k_\parallel$-filtering stems from the energy and in-plane momentum conservation in the resonant conversion "quasi-2D QW exciton$\rightarrow$ outgoing bulk photon". The α-dependent narrowing of the detected states results in an effective broadening

of the the first-order spatial coherence function. Furthermore, the sharp cutoff at $k_\parallel = k_\parallel^{(\alpha)}$ yields an oscillatory behaviour for $\tilde{g}^{(1)}$. Apparently this natural optical filter imposes an inherent coherence to the system, as light originating from a narrow strip in k-space will exhibit spatial coherence and produce interference patterns.

4.5 SUMMARY

In this Chapter the spatial coherence of quantum degenerate bosons was studied analytically in terms of appropriate normalised correlation functions. In particular an expression for the coherence function of a two-dimensional boson gas was derived and applied to indirect excitons in coupled quantum wells created under a non-resonant laser excitation. In this case the angular dependence of the exciton PL serves as an optical filter since only a small fraction of excitons with energies inside the photon cone can decay radiatively. Therefore, one should distinguish between the coherence function inferred from far-field experiments and the actual degree of coherence of the excitons. Indeed the large coherence lengths observed in systems of excitons and polaritons can be obtained only if such a distinction is made and the optical coherence function is used. The damped oscillatory behaviour of the optical coherence function originates from the sharp cut-off of the maximum exciton wavevector and is a signature of quantum mechanical interference. Thus, we conclude that even in the case were no Bose-Einstein condensation is assumed, the system of ideal bosons exhibits long range coherence as a combined effect of both statistics and low dimensionality.

5 CONCLUSIONS

This Chapter provides a brief summary of the conclusions of this dissertation and suggestions for possible future extension of the ideas presented in this work.

5.1 FORMATION OF EXCITON RINGS IN QUANTUM WELLS

The formation of excitonic rings around quantum well localities was described in Chapter 2 by means of a transport model for the free carriers and a quantum mass action law for the exciton formation. The influence of the effective temperature by the electron-phonon interaction and heating mechanisms were included in the description. In accordance with experimental observations, excitons were found to form in the perimeter of transverse electric current filaments which inject hot electrons in the QW plane. Under excitation by a defocused laser electrons and holes are dominant at different in-plane regions and excitons form only in the interface between these regions.

The accumulation of free carriers influences the local potential which is determined by solving the relevant Poisson equation. The current filaments act as anti-traps for the excitons created around them due to the strong repulsion between free and bound electrons. A quantum mass action law was introduced in order to describe the binding of free carriers into excitons as it proved to be necessary for the region of temperatures used in the experiments. Within this approach, the calculated exciton density reaches a maximum at a distance of $\sim 10\,\mu m$ from the filament centre, in agreement with the experimental observations of increase of the PL signal at the same distance.

Moreover, the appearance of PL rings indicates that the created excitons have low energies because they are created by well-thermalised carriers. This is consistent with the evolution of the temperature described by the thermalisation equation where both heating by the laser and the current filament is taken into account.

Hence, quantum well defects where an electrical breakdown occurs can serve as anti-traps around which a thermalised exciton cloud may form.

5.2   OPTICAL TRAPPING OF INDIRECT EXCITONS

In Chapter 3 the kinetics of indirect excitons in optically-induced traps is studied and compared with recent experimental results. Optical trapping exploits the dipolar character of indirect excitons in coupled quantum wells and offers a novel method where excitons are created by an annular laser excitation with the minimum energy at its centre. The migration of excitons from the ring position towards the trap centre is described by a quantum diffusion equation where the effects of degeneracy are incorporated via a generalised Einstein relation between the mobility and the diffusion coefficient. As in Chapter 2 the temporal evolution of the effective energy is governed by a thermalisation equation which now includes the possibility of heating or cooling due to radiative recombination of excitons.

The theoretical model is solved numerically in space and time domain to simulate the kinetics of excitons in the optical trap. In the presence of the laser excitation the trap is loaded with a degenerate exciton gas within 40 ns, $i.e.$, faster than their recombination time, and the effective temperature in its centre coincides with the lattice temperature. The maximum exciton density achieved for low excitation power is $n_{2D} = 1.4 \times 10^{10}\,\mathrm{cm}^{-2}$ corresponding to ground state occupation number $N_{E=0} \sim 1$. The system of indirect excitons reaches a steady state in approximately 50 ns. After removal of the confining potential excitons are free to expand in the QW plane and cool down very rapidly, within hundreds of picoseconds. In the simulations performed, the time evolution of the diffusion coefficient within a thermionic model approach is also recorded and found to increase with the passage of time. The latter behaviour is attributed to an effective screening of the long-range correlated disorder with increasing exciton density.

In conclusion, the hierarchy of time scales in an optically-induced trap allows for the

creation of a dense degenerate exciton gas at its centre, opening new routes for the appearance of spontaneous coherence in excitonic systems.

5.3 SPATIAL COHERENCE OF EXCITONS

Chapter 4 deals with the subject of exciton spatial coherence and the appropriate definition of the coherence length in systems of planar nanostructures. An analytic expression for the coherence function in a general system of two-dimensional non-interacting bosons is derived and compared with the corresponding expression for a classical gas. Although in both cases there is an increase of the coherence length with decreasing temperature, in quantum systems the coherence function exhibits at large spatial separations an exponential rather than Gaussian decay. Furthermore, the coherence in the case of particles obeying BE statistics is maintained for larger distances than in the case of MB distributed particles. Inclusion of interactions within a self-consistent Hartree-Fock approximation limits the coherence but leaves unchanged the exponential asymptotic behaviour of the coherence function. This is due to an increase of the effective exciton mass which is induced by the dipole-dipole repulsion between excitons.

Comparison of the calculated coherence lengths with available experimental data reveals a significant discrepancy. In order to find a compromise between these two different results the concept of $k_\parallel$-filtering is introduced. In far-field experiments the light collected from decaying excitons originates only from a narrow band in momentum space and consequently is expected to be coherent. An expression for the optical coherence function of excitons is developed and associated directly with the collection angle in experiments. This angle corresponds to a maximum wavevector as the upper limit of integration and introduces a $k_\parallel$-filtering effect. The calculated coherence function in this case exhibits a damped oscillatory behaviour and the corresponding coherence length is of the same order as the one inferred from the observations. These oscillations, originating from the sharp cutoff in the wavevector reflect the interference fringes emerging from matter waves with slightly different momentum.

Hence, the methods used in experiments to determine the spatial exciton coherence are proven to be inadequate to probe the existence of long range order in these systems. The analytic expressions for the coherence function presented in this Chapter offer a unique approach to study the coherence of two-dimensional bosonic systems

in the dilute limit and above the phase transition temperature, and a method for the calculation of the coherence length is presented for the first time. In the absence of any phase transitions, the system of indirect excitons in QWs exhibits coherence as a combined effect of both statistics and reduced dimensionality.

5.4 FUTURE WORK

In this thesis the transport and coherence properties of excitons were studied with no reference to a phase transition such as BEC, BCS or BKT superfluidity. However, the crossover to a degenerate gas was identified both in the vicinity of the QW localities and inside the optical traps where a sufficiently cold exciton gas was formed. This could be the onset of quantum degeneracy which would eventually lead to the appearance of spontaneous coherence in exciton systems. In spite of the fact that in the thermodynamic limit BEC in 2D is not possible at finite temperatures, the possibility of confining the excitons system offers a unique opportunity for the realisation of a condensate.

As far as the spatial coherence of excitons is concerned it seems that more sophisticated experiments should be designed to probe the emergence of long-range order, such as the famous Hanbury Brown-Twiss experiment for the measurement of the second order correlation function. From a theory point of view the calculation of higher order correlation functions in excitonic systems appears as a challenging task especially in the case of interacting particles. Finally, topological effects, such as Berry's phase, seem to have huge impact in the formation of excitonic condensates and their study is in progress.

These problems offer a unique discipline where the quantum nature of excitons can manifest itself in the macroscopic scale and places them between the most promising directions in fundamental solid state research.

A Derivation of the generalised Einstein relation

In classical diffusion the mobility of particles scales linearly with the diffusion coefficient and is inversely proportional to their thermal energy. In the case of transport through a crystal lattice the effect of temperature becomes even more pronounced as the interaction with the quanta of the lattice vibrations, *i.e.*, the phonons, is suppressed at low temperatures resulting in high values of the mobility. However, when the transport of quantum particles is considered the effect of different statistics is expected to alter the linear relation between the diffusion coefficient and mobility. Indeed, as we show below, the quantum nature of particles is reflected onto their *generalized Einstein relation* which now depends on the quantum degeneracy temperature and therefore on the density. Bosons, particles which tend to occupy the same quantum state, exhibit exponential increase of their mobility with increasing density. On the contrary, fermions, particles characterized by their avoidance of states already occupied, show decreasing mobility as their density increases an effect which can be traced back to Pauli's exclusion principle. In this Appendix the Einstein relation is derived first for a classical gas and then is generalized to include quantum particles obeying both statistics. The analysis is performed in terms of simple thermodynamic arguments and the only assumption made is that of local equilibrium, an approximation completely justifiable for the phenomena described in this thesis. The description is restricted in two dimensions although a generalisation in 3D is straightforward.

A.0.1 THE EINSTEIN RELATION

In the presence of an external field all thermodynamics potentials are shifted according to

$$\Delta X = \Delta X_0 + \Delta N \cdot u(\mathbf{R}),\qquad\text{(A.1)}$$

where ΔX_0 is the corresponding value when the external field $u(\mathbf{R})$ is zero and ΔN is the number of particles inside the area ΔS. The vector $\mathbf{R}$ defines the center of the area ΔS. Thus, for Gibbs free energy

$$\Delta G(\mathbf{R}) = \mu \cdot \Delta N\qquad\text{(A.2)}$$

Eq. (A.1) yields

$$\mu = \mu_0(n(\mathbf{r}), T) + u(\mathbf{r}),\qquad\text{(A.3)}$$

where $n(\mathbf{R}) \equiv \frac{\Delta N}{\Delta S}$ is the concentration of particles in the presence of the external field.

In the case of local inhomogeneity, a particle current occurs in order to bring the system back to equilibrium and flatten any local extrema in the concentration. This particle current is given as the gradient of the total chemical potential, namely

$$J_{total} = -C\nabla\mu = -C\frac{\partial\mu_0}{\partial n}\nabla n - C\nabla u,\qquad\text{(A.4)}$$

with n being the concentration of particles and C a constant of proportionality which will be defined below. In the presence of an external field the total flux of particles includes two contributions: a diffusion current due to gradients in the concentration and a drift current caused by the gradient of the external potential. Thus in the most general case the total particle current is given by the well known formula

$$J_{total} = J_{diffusion} + J_{drift} = -D_\mathrm{x}\nabla n - \mu_\mathrm{x} n\nabla u,\qquad\text{(A.5)}$$

where μ_x is the mobility and D_x the diffusion coefficient. By direct comparison of Eqs. (A.4) and (A.5) one can determine the constant C as:

$$C = \mu_\mathrm{x}\, n\qquad\text{(A.6)}$$

and the diffusion coefficient as

$$D_{\mathrm{x}} = C \frac{\partial \mu_0}{\partial n} \Rightarrow D_{\mathrm{x}} = \mu_{\mathrm{x}} n \frac{\partial \mu_0}{\partial n} , \tag{A.7}$$

Thus the mobility is proportional to the diffusion coefficient. Equation A.7 is rather general and allows one to determine the relation between the mobility and the diffusion coefficient for different distributions. For a classical distribution the chemical potential reads

$$\mu_0 = -k_{\mathrm{B}} T \ln[n^{-1} f(T)] = k_{\mathrm{B}} T \ln n + ... \Rightarrow \left(\frac{\partial \mu_0}{\partial n} \right)_T = \frac{k_{\mathrm{B}} T}{n} \tag{A.8}$$

and therefore

$$\mu_{\mathrm{x}} = \frac{D_{\mathrm{x}}}{k_{\mathrm{B}} T} \tag{A.9}$$

which is the Einstein relation.

A.0.2 THE GENERALISED EINSTEIN RELATION

For low temperatures quantum degeneracy plays an important role and the Maxwell-Boltzmann distribution is no longer valid but it should be replaced by Bose-Einstein or Fermi-Dirac statistics for bosons and fermions, respectively. The difference in the two cases is manifested via the chemical potential. In this subsection Einstein's relation is generalised for the two different types of quantum particles.

BOSONS

The chemical potential for a two-dimensional gas of N bosons with spin $s = 0$ and mass M confined to move in an area S is:

$$\mu_0 = k_{\mathrm{B}} T \ln(1 - e^{-T_0/T}) \quad ; \quad k_{\mathrm{B}} T_0 = \frac{2\pi \hbar^2}{M} n_{2\mathrm{D}} , \tag{A.10}$$

where T_0 is the degeneracy temperature $n_{2\mathrm{D}} = N/S$. Differentiation with respect to concentration yields

$$\frac{\partial \mu_0}{\partial n_{2\mathrm{D}}} = \frac{k_{\mathrm{B}} T_0}{n_{2\mathrm{D}}} \frac{1}{e^{T_0/T} - 1} \tag{A.11}$$

and substitution into the general expression (A.7) yields the generalized Einstein relation for bosons

$$\mu_B = \frac{D_x}{k_B T_0}(e^{T_0/T} - 1).$$ (A.12)

It is evident from Eq. (A.12) that in the classical limit the usual Einstein relation is recovered.

FERMIONS

The chemical potential for a two-dimensional gas of N fermions with spin $s = 1/2$ and mass m confined to move in an area S is:

$$\mu_0 = k_B T \ln(e^{T_0/T} - 1) \quad ; \quad k_B T_0 = \frac{\pi \hbar^2}{m} n_{2D}$$ (A.13)

hence

$$\frac{\partial \mu_0}{\partial n_{2D}} = \frac{k_B T_0}{n_{2D}} \frac{1}{1 - e^{T_0/T}}$$ (A.14)

and therefore for fermions the generalised Einstein relation reads

$$\mu_F = \frac{D_x}{k_B T_0}(1 - e^{-T_0/T}).$$ (A.15)

Comparison of Eqs. (A.12) and (A.15) reveals a striking difference between particles obeying Bose and those described by Fermi statistics. For the former the mobility increases with increasing density as a consequence of their tendency to cluster together, whereas for the latter the effect of rise in the concentration is a phase-space filling and consequently the value of the mobility saturates. In conclusion, the underlying quantum characteristics of diffusing particles manifest themselves in their macroscopic transport through Eqs. (A.12) and (A.15) introducing nonlinearities in the corresponding transport equations.

B CALCULATION OF THE CAPTURE COEFFICIENT

In order to describe simultaneously the equilibration kinetics of electrons, holes and excitons, we formulate a Boltzmann-Uhlenbeck equation taking into account all scattering processes which create an exciton from an electron-hole pair and vice versa.

$$
\partial_t N(\mathbf{K}) = -\frac{2\pi}{\hbar} \sum_{\mathbf{k}} U_0^2 \left\{ f(\mathbf{k}_e)f(\mathbf{k}_h)[1 + \eta(\mathbf{K})] - \eta(\mathbf{K})[1 - f(\mathbf{k}_e)][1 - f(\mathbf{k}_h)] \right\}
$$
$$
\times \delta \left(\frac{\hbar^2 K^2}{2M_x} + E_b - \frac{\hbar^2 k_e^2}{2m_e} - \frac{\hbar^2 k_h^2}{2m_h} \right), \tag{B.1}
$$

where m_e, $\mathbf{k}_e$, m_h, $\mathbf{k}_h$ and M_x, $\mathbf{K}$ denote the effective masses and wavevectors of electrons, holes and excitons respectively, E_b is the exciton binding energy, and f, η are the Fermi-Dirac and Bose-Einstein distributions, respectively.

It is convenient to change coordinate system and describe the motion of bound and unbound electron-hole pairs using the centre of mass and relative motion coordinates defined as follows:

$$
\mathbf{R} = \frac{m_e \mathbf{r}_e + m_h \mathbf{r}_h}{m_e + m_h}, \qquad \mathbf{r} = \mathbf{r}_e + \mathbf{r}_h. \tag{B.2}
$$

In the new system the Boltzmann-Uhlenbeck equation takes the form:

$$
\partial_t N(\mathbf{K}) = -\frac{2\pi}{\hbar} \sum_{\mathbf{k}} U_0^2 \left\{ f(\alpha\mathbf{K} + \mathbf{k})f(\beta\mathbf{K} - \mathbf{k})[1 + \eta(\mathbf{K})] - \eta(\mathbf{K})[1 - f(\alpha\mathbf{K} + \mathbf{k})] \right.
$$
$$
\left. \times [1 - f(\beta\mathbf{K} - \mathbf{k})] \right\} \delta \left(E_b - \frac{\hbar^2 k^2}{2\mu} \right), \tag{B.3}
$$

where $\beta = m_e/M_x, \alpha = m_h/M_x, \mu = m_e m_h/M_x$ and $M_x = m_e + m_h$.

The summation over **k** can be transformed into two-dimensional integration using:

$$\sum_{\mathbf{k}} \to \frac{S}{(2\pi)^2} \int_0^\infty \int_0^{2\pi} k \, dk \, d\theta, \tag{B.4}$$

Assuming that the dominant process is annihilation of an electron-hole pair and simultaneous creation of an exciton and that in the dilute limit the Fermi-Dirac distribution can be substituted by Boltzmann statistics, Eq. (B.3) yields:

$$\partial_t N(\mathbf{K}) = -\frac{2\pi}{\hbar} U_0^2 \frac{S}{(2\pi)^2} A_e A_h A_K \int_0^\infty \int_0^{2\pi} k e^{\hbar^2 k^2 / 2\mu k_B T} \delta \left(E_b - \frac{\hbar^2 k^2}{2\mu} \right) dk \, d\theta, \tag{B.5}$$

where A_e and A_h are the fugacities of electrons and holes respectively:

$$A_e = e^{\mu_e / k_B T}, \qquad A_h = e^{\mu_h / k_B T}, \tag{B.6}$$

and

$$A_K = e^{-\hbar^2 K^2 / 2M_x k_B T}. \tag{B.7}$$

Performing the integration with respect to θ and changing variables we obtain:

$$\partial_t N(\mathbf{K}) = -\frac{U_0^2 S}{k_B T \hbar} A_e A_h A_K \frac{\mu k_B T}{\hbar^2} \int_0^\infty dx \, e^{-x} \delta \left(x - \frac{E_b}{k_B T} \right). \tag{B.8}$$

The last integration is easily carried out if we use:

$$\delta(f(x)) = \sum_i \frac{\delta(x - x_i)}{|f'(x_i)|} \quad ; \quad f(x_i) = 0. \tag{B.9}$$

and the result is

$$\partial_t N(\mathbf{K}) = -U_0^2 S \frac{\mu}{\hbar^3} A_e A_h A_K e^{-E_b / k_B T} \tag{B.10}$$

The temporal evolution of the exciton density will be determined by

$$\partial_t n_x = \frac{1}{S} \sum_{\mathbf{K}} \partial_t N(\mathbf{K}). \tag{B.11}$$

Substituting (B.10) into (B.11) and using (B.4) once more gives

$$\partial_t n_x = -\frac{1}{S} U_0^2 S \frac{\mu}{\hbar^3} A_e A_h e^{-E_b / k_B T} \frac{S}{(2\pi)^2} 2\pi \int_0^\infty K e^{-\hbar^2 K^2 / 2M_x k_B T} dK, \tag{B.12}$$

which after the integration becomes:

$$\partial_t n_{\mathrm{x}} = -U_0^2 S \frac{\mu}{2\pi\hbar^5} A_e A_h M k_{\mathrm{B}} T e^{-E_b/k_{\mathrm{B}}T} \,. \tag{B.13}$$

Equation (B.13) can be further simplified if we use the definition of the degeneracy temperature for fermions

$$k_{\mathrm{B}} T_0^{e(h)} = \frac{\pi\hbar^2}{m_{e(h)}} n_{\mathrm{2D}}^{e(h)} \,, \tag{B.14}$$

and notice that

$$A_e A_h = \frac{T_0^e T_0^h}{T^2} \quad ; \quad \mu M_{\mathrm{x}} = m_e m_h \,. \tag{B.15}$$

Finally the evolution in time of the electron-hole pairs scattering into excitons is governed by:

$$\partial_t n_{\mathrm{x}} = -U_0^2 S \frac{\pi}{2\hbar k_{\mathrm{B}}T} \, n_{\mathrm{2D}}^e \, n_{\mathrm{2D}}^h \, e^{-E_b/k_{\mathrm{B}}T} \,, \tag{B.16}$$

or

$$\partial_t n_{\mathrm{x}} = -\gamma n_{2D}^e \, n_{2D}^h \quad ; \quad \gamma = U_0^2 S \frac{\pi}{2\hbar k_{\mathrm{B}}T} \, e^{-E_b/k_{\mathrm{B}}T} \,. \tag{B.17}$$

B.0.3 THE MATRIX ELEMENT OF THE INTERACTION

In the above discussion the matrix element of the interaction U_0 was left undefined since we restricted ourselves in a general description of the scattering process. Let us now determine U_0 by starting with the general scattering Hamiltonian written in the second quantization language:

$$H = H_0 + H_1 \,, \tag{B.18}$$

$$H_1 = \frac{1}{\sqrt{S}} \sum_{\mathbf{K},\mathbf{k}} \tilde{U}_0 \left[B_{\mathbf{K}}^\dagger \, a_{\alpha\mathbf{K}+\mathbf{k}} \, b_{\beta\mathbf{K}-\mathbf{k}} + H.C. \right] \,, \tag{B.19}$$

where B is a bosonic operator, a, b are operators for fermions and:

$$\frac{\tilde{U}_0}{\sqrt{S}} = U_0 \Rightarrow U_0^2 S = \tilde{U}_0^2 \quad ; \quad U_0 = \langle i | V_0 | f \rangle \,. \tag{B.20}$$

For the case under investigation the initial state, denoted by $|i\rangle$, can be considered to be a product of two plane waves, whereas the final state, $|f\rangle$, should be described by the product of a plane wave and the exciton wavefunction. Finally, the interaction

potential is taken to be of Coulomb form. Summarising all these properties we have:

$$|i\rangle = \frac{1}{\sqrt{S}} e^{i\mathbf{K}\mathbf{R}} \frac{1}{\sqrt{S}} e^{i\mathbf{k}\mathbf{r}} , \tag{B.21}$$

$$|f\rangle = \phi_{\mathrm{x}}(\mathbf{r}) e^{i\mathbf{K}'\mathbf{R}} , \tag{B.22}$$

$$\phi_{\mathrm{x}}(\mathbf{r}) = \left(\frac{2}{\pi a_0^2}\right)^{1/2} e^{-r/a_0} , \tag{B.23}$$

$$V_0 = \frac{e^2}{\varepsilon_{\mathrm{b}} r} . \tag{B.24}$$

Using the above definitions we are able to determine the matrix element of the interaction as follows:

$$U_0 = \langle i|V_0|f\rangle \tag{B.25}$$

$$= \left(\frac{1}{S} \int d^2\mathbf{R}\ e^{i(\mathbf{K}'-\mathbf{K})\mathbf{R}}\right) \frac{1}{\sqrt{S}} \frac{e^2}{\varepsilon_{\mathrm{b}}} \left(\frac{2}{\pi a_0^2}\right)^{1/2} \int d^2\mathbf{r}\ \frac{1}{r}\ e^{-i\mathbf{k}\mathbf{r}}\ e^{-r/a_0} \tag{B.26}$$

$$= \delta_{\mathbf{K}\mathbf{K}'} \frac{1}{\sqrt{S}} \frac{e^2}{\varepsilon_{\mathrm{b}}} \left(\frac{2}{\pi a_0^2}\right)^{1/2} 2\pi \int_0^\infty dr e^{-r/a_0} J_0(k\,r) \tag{B.27}$$

$$= \delta_{\mathbf{K}\mathbf{K}'} \frac{1}{\sqrt{S}} \frac{e^2}{\varepsilon_{\mathrm{b}}} \left(\frac{2}{\pi a_0^2}\right)^{1/2} 2\pi \frac{1}{\sqrt{\frac{1}{a_0^2} + k^2}} . \tag{B.28}$$

Finally we end up with the following expression for $\tilde{U}_0$:

$$\tilde{U}_0{}^2 = U_0^2 S = \frac{e^4}{\varepsilon_{\mathrm{b}}^2} \frac{8\pi}{(k^2 a_0^2 + 1)} , \tag{B.29}$$

where a_0 is the excitonic Bohr radius and is given by

$$a_0 = \frac{\hbar^2 \varepsilon_{\mathrm{b}}}{\mu e^2} . \tag{B.30}$$

Combining Eq. (B.17) with (B.29) and considering only the limit $\mathbf{k} \to 0$ one obtains the final expression for γ:

$$\gamma = \frac{4\pi^2 e^4}{\varepsilon_{\mathrm{b}} \hbar k_{\mathrm{B}} T}\ e^{-E_{\mathrm{b}}/k_{\mathrm{B}} T} . \tag{B.31}$$

REFERENCES

[1] L. V. Butov, A. C. Gossard and D. S. Chemla. Macroscopically ordered state in an exciton system. *Nature*, **418**, 751 (2002).

[2] A. L. Ivanov, L. E. Smallwood, A. T. Hammack, S. Yang, L. V. Butov and A. C. Gossard. Origin of the inner ring in photoluminescence patterns of quantum well excitons. *Europhys. Lett.*, **73**, 920 (2006).

[3] C. W. Lai. *Spatially Indirect Excitons in Coupled Quantum Wells*. Ph.D. thesis, University of California, Berkeley (2004).

[4] C. Kittel. *Introduction to Solid State Physics, 7th ed.* (Wiley, New York, 1996).

[5] D. L. Dexter and R. S. Knox. *Excitons* (Wiley, New York, 1965).

[6] J. Frenkel. On the transformation of light into heat in solids. I. *Phys. Rev.*, **37**, 17 (1931).

[7] J. Frenkel. On the transformation of light into heat in solids. II. *Phys. Rev.*, **37**, 1276 (1931).

[8] G. H. Wannier. The structure of electronic excitation levels in insulating crystals. *Phys. Rev.*, **52**, 191 (1937).

[9] N. F. Mott. Conduction in polar crystals. II. the conduction band and ultra-violet absorption of alkali-halide crystals. *Trans. Faraday Soc.*, **34**, 500 (1938).

[10] E. Burstein and C. Weisbuch, editors. *Confined Electrons and Photons - New Physics and Devices* (Plenum Press, New York, 1995).

[11] P. Y. Yu and M. Cardona. *Fundamendals of semicontuctors: physics and material properties* (Springer, Berlin, 2001).

[12] R. C. Miller, D. A. Kleinman, W. T. Tsang and A. C. Gossard. Observation of the excited level of excitons in gaas quantum wells. *Phys. Rev. B*, **24**, 1134 (1981).

[13] G. Bastard, E. E. Mendez, L. L. Chang and L. Esaki. Exciton binding energy in quantum wells. *Phys. Rev. B*, **26**, 1974 (1982).

[14] R. L. Greene, K. K. Bajaj and D. E. Phelps. Energy levels of Wannier excitons in GaAs-Ga$_{1-x}$Al$_x$As quantum-well structures. *Phys. Rev. B*, **29**, 1807 (1984).

[15] S. Charbonneau, M. L. W. Thewalt, E. S. Koteles and B. Elman. Transformation of spatially direct to spatially indirect excitons in coupled double quantum wells. *Phys. Rev. B*, **38**, 6287 (1988).

[16] Y. E. Lozovik and I. V. Ovchinnikov. Controlling spatially indirect exciton condensate in coupled quantum wells by external fields and phonon laser. *Solid State Commun.*, **118**, 251 (2001).

[17] J. E. Golub, K. Kash, J. P. Haribson and L. T. Florez. Long-lived spatially indirect excitons in coupled GaAs/Al$_x$Ga$_{1-x}$As quantum wells. *Phys. Rev. B*, **41**, 8564 (1990).

[18] A. Alexandrou, J. A. Kash, E. E. Mendez, M. Zachau, J. M. Hong, T. Fukuzawa and Y. Hase. Electric-field effects on exciton lifetimes in symmetric coupled GaAs/Al$_{0.3}$Ga$_{0.7}$As double quantum wells. *Phys. Rev. B*, **42**, 9225 (1990).

[19] A. V. Larionov, V. B. Timofeev, J. Hvam and K. Soerensen. Interwell excitons in GaAs/AlGaAs double quantum wells and their collective properties. *JETP*, **90**, 1093 (2000).

[20] P. Noziéres and C. Comte. Exciton Bose condensation: the ground of an electron-hole gas II. spin states, screening and band structure effects. *J. Phys. (Paris)*, **43**, 1083 (1982).

[21] K. Huang. *Statistical Mechanics* (Wiley, New York, 1987).

[22] L. D. Landau and E. M. Lifshitz. *Statistical Physics Vol. 5: Course of Theoretical Physics* (Pergamon Press, 1980).

[23] S. A. Moskalenko and D. W. Snoke. *Bose-Einstein condensation of excitons and biexcitons* (Cambridge University Press, 2000).

[24] S. Bose. *Z. Physik*, **26**, 178 (1924).

[25] A. Einstein. *Sitzber. Kgl. Preuss. Akad. Wiss.*, page 261 (1924).

[26] M. H. Anderson, J. R. Ensher, M. R. Matthews, C. E. Wieman and E. A. Cornell. Observation of Bose-Einstein condensation in a dilute atomic vapour. *Science*, **269**, 198 (1995).

[27] K. B. Davis, M. O. Mewes, M. A. Joffe, M. R. Andrews and W. Ketterle. Evaporative cooling of sodium atoms. *Phys. Rev. Lett.*, **74**, 5202 (1995).

[28] E. A. Cornell and C. E. Wieman. Nobel Lecture: Bose-Einstein condensation in a dilute gas, the first 70 years and some recent experiments. *Rev. Mod. Phys.*, **74**, 875 (2002).

[29] G. Modugno, G. Ferrari, G. Roati, R. J. Brecha, A. Simoni and M. Inguscio. Bose-Einstein condensation of potassium atoms by sympathetic cooling. *Science*, **294**, 1320 (2001).

[30] C. C. Bradley, C. A. Sackett, J. J. Tollet and R. G. Hulet. Evidence of Bose-Einstein condensation in an atomic gas with attractive interactions. *Phys. Rev. Lett.*, **75**, 1687 (1995).

[31] A. Griffin, D. W. Snoke and S. Stringari, editors. *Bose-Einstein Condensation* (Cambridge University Press, 1995).

[32] T. Weber, J. Herbig, M. Mark, H. C. Nägerl and R. Grimm. Bose-Einstein condensation of cesium. *Science*, **299**, 232 (2003).

[33] D. G. Fried, T. C. Killian, L. Willmann, D. Landhuis, S. C. Moss, D. Kleppner and T. J. Greytak. Bose-Einstein condensation of atomic hydrogen. *Phys. Rev. Lett.*, **81**, 3811 (1998).

[34] S. A. Moskalenko. Reversible optico-hydrodynamic phenomena in a nonideal exciton gas. *Fiz. Tverd. Tela*, **4**, 276 (1962).

[35] J. M. Blatt, K. W. Böer and W. Brandt. Bose-Einstein condensation of excitons. *Phys. Rev.*, **126**, 1691 (1962).

[36] L. V. Keldysh and A. N. Kozlov. Collective properties of excitons in semiconductors. *Sov. Phys. JETP*, **27**, 521 (1968).

[37] D. Hulin, A. Mysyrowciz and C. B. à la Guillaume. Evidence for Bose-Einstein statistics in an exciton gas. *Phys. Rev. Lett.*, **45**, 1970 (1980).

[38] D. Snoke, J. P. Wolfe and A. Mysyrowicz. Quantum saturation of a Bose gas: Excitons in Cu_2O. *Phys. Rev. Lett.*, **59**, 827 (1987).

[39] D. W. Snoke, J. P. Wolfe and A. Mysyrowicz. Evidence for Bose-Einstein condensation of a two-component exciton gas. *Phys. Rev. Lett.*, **64**, 2543 (1990).

[40] M. Hasuo, N. Nagasawa, T. Itoh and A. Mysyrowicz. Progress in the Bose-Einstein condesation of biexcitons in CuCl. *Phys. Rev. Lett.*, **70**, 1303 (1993).

[41] E. Fortin, S. Fafard and A. Mysyrowicz. Exciton transport in Cu_2O: Evidence for excitonic superfluidity? *Phys. Rev. Lett.*, **70**, 3951 (1993).

[42] T. Goto, M. Y. Shen, S. Koyama and T. Yokouchi. Bose-Einstein statistics of orthoexcitons generated by two-photon resonant absorption in cuprous oxide. *Phys. Rev. B*, **55**, 7609 (1997).

[43] G. M. Kavoulakis, G. Baym and J. P. Wolfe. Quantum saturation and condensation of excitons in Cu_2O: A theoretical study. *Phys. Rev. B*, **53**, 7227 (1996).

[44] G. M. Kavoulakis and A. Mysyrowicz. Auger decay, spin exchange, and their connection to Bose-Einstein condensation of excitons in Cu_2O. *Phys. Rev. B*, **61**, 16619 (2000).

[45] M. Kuwata-Gonokami, M. Kubouchi, R. Shimano and A. Mysyrowicz. Time-resolved excitonic Lyman spectroscopy of Cu_2O. *J. Phys. Soc. Japan*, **73**, 1065 (2003).

[46] K. Johnsen and G. M. Kavoulakis. Bose-Einstein condensation of excitons with electromagnetic radiation. *Phys. Rev. Lett.*, **86**, 858 (2001).

[47] M. Nagai, R. Shimano, K. Horiuchi and M. Kuwata-Gonokami. Creation of supercooled exciton gas and transformation to electron-hole droplets in diamond. *Phys. Rev. B*, **68**, 081202(R) (2003).

[48] C. Ell, A. L. Ivanov and H. Haug. Relaxation kinetics of a low-density exciton gas in Cu_2O. *Phys. Rev. B*, **57**, 9663 (1998).

[49] A. L. Ivanov, C. Ell and H. Haug. Phonon-assisted Boltzmann kinetics of a Bose gas: Generic solution for $T \leq T_c$. *Phys. Rev. E*, **55**, 6363 (1997).

[50] J. P. Wolfe and J. I. Jang. New perspectives on kinetics of excitons in Cu_2O. *Solid State Commun.*, **134**, 143 (2005).

[51] K. E. O'Hara, L. O. Súilleábhain and J. P. Wolfe. Strong non-radiative recombination of excitons in Cu_2O and its impact on Bose-Einstein statistics. *Phys. Rev. B*, **60**, 10565 (1999).

[52] A. Swarup and B. Cowan. Fermi-Bose correspondence and Bose-Einstein condensation in the two-dimensional ideal gas. *J. Low Temp. Phys.*, **134**, 881 (2004).

[53] V. Bagnato and D. Kleppner. Bose-Einstein condensation in low-dimensional traps. *Phys. Rev. A*, **44**, 7439 (1991).

[54] W. Ketterle and N. J. van Druten. Bose-Einstein condensation of a finite number of particles trapped in one or three dimensions. *Phys. Rev. A*, **54**, 656 (1996).

[55] V. L. Berezinskii. Destruction of long-range order in one-dimensional and two-dimensional systems possesing a continuous symmetry group. II. Quantum systems. *Soviet Physics JETP*, **34**, 610 (1972).

[56] J. M. Kosterlitz and D. J. Thouless. Ordering, metastability and phase transitions in two-dimensional systems. *J. Phys. C*, **6**, 1181 (1973).

[57] P. Roussignol, C. Delalande, A. Vinattieri, L. Carraresi and M. Colocci. Dynamics of exciton relaxation in $GaAs/Al_xGa_{1-x}As$ quantum wells. *Phys. Rev. B*, **45**, 6965 (1992).

[58] M. H. Zhang, Q. Huang and J. M. Zhou. Calculations of the time taken for excitons to form in GaAs quantum wells. *J. Phys.: Condens, Matter*, **9**, 10185 (1997).

[59] T. C. Damen, J. Shah, D. Y. Oberli, D. S. Chemla, J. E. Cunningham and J. M. Kuo. Dynamics of exciton formation and relaxation in GaAs quantum wells. *Phys. Rev. B*, **42**, 7434 (1990).

[60] P. W. M. Blom, P. J. van Hall, C. Smit and J. P. C. andJ H Wolter. Selective exciton formation in thin $GaAs/Al_xGa_{1-x}As$ quantum wells. *Phys. Rev. Lett.*, **71**, 3878 (1993).

[61] D. Robart, X. Marie, B. Baylac, T. Amand, M. Brousseau, G. Bacquet, G. Debart, R. Planel and J. M. Gerard. Dynamical equilibrium bewteen excitons and free carriers in quantum wells. *Solid State Commun.*, **95**, 287 (1995).

[62] R. Kumar, A. S. Vengurlekar, S. S. Prabhu, J. Shah and L. N. Pfeiffer. Picosecond time evolution of free electron-hole pairs into excitons in GaAs quantum wells. *Phys. Rev. B*, **54**, 4891 (1996).

[63] J. Kusano, Y. Segawa, Y. Aoyagi, S. Namba and H. Okamoto. Extremely slow energy relaxation of a two-dimensional exciton in a GaAs superlattice structure. *Phys. Rev. B*, **40**, 1685 (1989).

[64] A. Thilagam and J. Singh. Generation rate of 2D excitons in quantum wells. *J. Lumin.*, **55**, 11 (1993).

[65] J. Szczytco, L. Kappei, J. Berney, F. Morier-Genoud, M. T. Portella-Oberli and B. Deveaud. Determination of the exciton formation in quantum wells from time-resolved interband luminescence. *Phys. Rev. Lett.*, **93**, 137401 (2004).

[66] J. Szczytco, L. Kappei, F. Morier-Genoud, T. Guillet, M. T. Portella-Oberli and B. Deveaud. Excitons or free carriers? That is the question. *Phys. stat. sol. (c)*, **1**, 493 (2004).

[67] I. K. Oh and J. Singh. Formation of excitons from free electron-hole pairs due to acoustic phonon interactions in quantum wells. *Superlattices Microstruct.*, **30**, 221 (2001).

[68] A. L. Ivanov, P. B. Littlewood and H. Haug. Bose-Einstein statistics in thermalization and photoluminescence of quantum-well excitons. *Phys. Rev. B*, **59**, 5032 (1999).

[69] A. L. Ivanov. Thermalization and photoluminescence dynamics of indirect excitons at low bath temperatures. *J. Phys.: Condens. Matter*, **16**, S3629 (2004).

[70] U. Bockelmann. Phonon scattering between zero-dimensional electronic states: Spatial versus Landau quantization. *Phys. Rev. B*, **50**, 17271 (1994).

[71] P. J. Price. Two-dimensional electron transport in semiconductor layers, 1. Phonon scattering. *Ann. Phys.*, **133**, 217 (1981).

[72] L. E. Smallwood. *Thermalization, Diffusion and Photoluminescence of Statistically-Degenerate Indirect Excitons in Coupled Quantum Wells*. Ph.D. thesis, Cardiff University, Cardiff (2006).

[73] P. Stenius. *Creation of coherent excitons in semiconductor quantum structures*. Ph.D. thesis, University of California, Santa Barbara (1998).

[74] E. Hanamura. Rapid radiative decay and enhanced optical nonlinearity of excitons in a quantum well. *Phys. Rev. B*, **38**, 1228 (1988).

[75] L. C. Andreani, F. Tassone and F. Bassani. Radiative lifetime of free excitons in quantum wells. *Solid State Commun.*, **77**, 641 (1990).

[76] G. Björk, S. Pau, J. Jacobson and Y. Yamamoto. Wannier exciton superradiance in a quantum-well microcavity. *Phys. Rev. B*, **50**, 17336 (1994).

[77] D. S. Citrin. Radiative lifetimes of excitons in quantum wells: Localization and phase coherence effects. *Phys. Rev. B*, **47**, 3832 (1993).

[78] A. V. Soroko, A. L. Ivanov and L. V. Butov. Thermalization and photoluminescence kinetics of statistically-degenerate indirect excitons in GaAs/AlGaAs coupled quantum wells. *Phys. stat. sol. (a)*, **190**, 719 (2002).

[79] L. V. Butov, A. L. Ivanov, A. Imamoglu, P. B. Littlewood, A. A. Shashkin, V. T. Dolgopolov, K. L. Campman and A. C. Gossard. Stimulated scattering of indirect excitons in coupled quantum wells: signature of a degenerate Bose-gas of excitons. *Phys. Rev. Lett.*, **86**, 5608 (1998).

[80] U. Bockelmann, G. Abstreiter, G. Weimann and W. Schlapp. Single-particle and transport scattering times in narrow $GaAs/Al_xGa_{1-x}As$ quantum-wells. *Phys. Rev. B*, **41**, 7864 (1990).

[81] H. Sakaki, T. Noda, K. Hirakawa, M. Tanaka and T. Matsusue. Interface roughness scattering in GaAs/AlAs quantum wells. *Appl. Phys. Lett.*, **51**, 1934 (1987).

[82] A. Gold. Electronic transport properties of a two-dimensional electron gas in a silicon quantum-well structure at low temperature. *Phys. Rev. B*, **35**, 723 (1987).

[83] B. Vinter. Low-temperature phonon-limited electron mobility in modulation-doped heterostructures. *Phys. Rev. B*, **33**, 5904 (1985).

[84] E. E. Mendez, P. J. Price and M. Heiblum. Temperature dependence of the electron mobility in GaAs-AlGaAs heterostuctures. *Appl. Phys. Lett.*, **45**, 294 (1984).

[85] H. Wang, M. Jiang and D. G. Steel. Measurement of phonon-assisted migration of localized excitons in GaAs/AlGaAs multiple-quantum-well stuctures. *Phys. Rev. Lett.*, **65**, 1255 (1990).

[86] H. W. Yoon, D. R. Wake, J. P. Wolfe and H. Morkoç. In-plane transport of photoexcited carriers in GaAs quantum wells. *Phys. Rev. B*, **46**, 13461 (1992).

[87] D. Oberhauser, K. H. Pantke, J. M. Hvam, G. Weimann and C. Klingshirn. Exciton scattering in quantum wells at low temperatures. *Phys. Rev. B*, **47**, 6827 (1993).

[88] G. D. Gilliland, M. S. Petrovic, H. P. Hjalmarson, D. J. Wolford, G. A. Northrop, T. F. Kuech, L. M. Smith and J. A. Bradley. Time-dependent heterointerfacial band bending and quasi-two-dimensional excitonic transport in GaAs structures. *Phys. Rev. B*, **58**, 4728 (1998).

[89] M. Achermann, B. A. Nechay, F. Morier-Genoud, A. Schertel, U. Siegner and U. Keller. Direct experimental observation of different diffusive transport regimes in semiconductor nanostructures. *Phys. Rev. B*, **60**, 2101 (1999).

[90] H. Zhao, S. Moehl, S. Wachter and H. Kalt. Hot exciton transport in ZnSe quantum wells. *Appl. Phys. Lett.*, **80**, 1391 (2002).

[91] H. Zhao, B. D. Don, S. Moehl and H. Kalt. Spatiotemporal dynamics of quantum-well excitons. *Phys. Rev. B*, **67**, 035306 (2003).

[92] Z. Vörös, R. Balili, D. W. Snoke, L. Pfeiffer and K. West. Long-distance diffusion of excitons in double quantum well structures. *Phys. Rev. Lett.*, **94**, 226401 (2005).

[93] R. Rapaport, G. Chen and S. H. Simon. Nonlinear dynamics of a dense two-dimensional dipolar exciton gas. *Phys. Rev. B*, **73**, 033319 (2006).

[94] J. Hegarty, L. Goldner and M. D. Sturge. Localized and delocalized two-dimensional excitons in GaAs/AlGaAs multiple-quantum-well structures. *Phys. Rev. B*, **30**, R7346 (1984).

[95] A. L. Ivanov. Quantum diffusion of dipole-oriented indirect excitons in coupled quantum wells. *Europhys. Lett.*, **59**, 586 (2002).

[96] F. Martelli, A. Polimeni, A. Patanè, M. Capizzi, P. Borri, M. Gurioli, M. Colocci, A. Bosacchi and S. Franchi. Exciton localization by potential fluctuations at the interface of InGaAs/GaAs quantum wells. *Phys. Rev. B*, **53**, 7421 (1996).

[97] G. Bastard, C. Delalande, M. H. Meynadier, P. M. Frijlink and M. Voos. Low-temperature exciton trapping on interface defects in semiconductor quantum wells. *Phys. Rev. B*, **29**, 7042 (1984).

[98] M. Zachau, J. A. Kash and T. Masselink. Relaxation of excitons in thin quantum wells. *Phys. Rev. B*, **44**, 8403 (1991).

[99] H. Hillmer, A. Forchel, S. Hansmann, M. Morohashi, E. Lopez, H. P. Meier and K. Ploog. Optical investigations on the mobility of two-dimensional excitons in GaAs/Ga$_{1-x}$Al$_x$As quantum wells. *Phys. Rev. B*, **39**, 10901 (1989).

[100] H. Tang. Influence of interface roughness on excitonic diffusion in semiconductor quantum well. *J. Phys.: Condens. Matter*, **15**, 8137 (2003).

[101] L. Schrottke, H. T. Grahn and K. Fujiwara. Excitonic properties of weakly coupled GaAs single quantum wells investigated with high-resolution photoluminescence excitation spectroscopy. *Phys. Rev. B*, **56**, 13321 (1997).

[102] S. D. Baranovskii, R. Eichmann and P. Thomas. Temperature-dependent exciton luminescence in quantum wells by computer simulation. *Phys. Rev. B*, **58**, 13081 (1998).

[103] L. V. Butov. Condensation and pattern formation in cold exciton gases in coupled quantum wells. *J. Phys.: Condens. Matter*, **16**, R1577 (2004).

[104] V. Negoita, D. W. Snoke and K. Eberl. Huge density-dependent blueshift of indirect excitons in biased coupled quantum wells. *Phys. Rev. B*, **61**, 2779 (2000).

[105] S. B.-T. de Leon and B. Laikhtman. Exciton-exciton interactions in quantum wells: Optical properties and energy spin relaxation. *Phys. Rev. B*, **63**, 125306 (2001).

[106] L. V. Butov, A. A. Shashkin, V. T. Dolgopolov, K. L. Campman and A. C. Gossard. Magneto-optics of the spatially separated electron and hole layers in GaAs/Al$_x$Ga$_{1-x}$As coupled quantum wells. *Phys. Rev. B*, **60**, 8753 (1999).

[107] L. V. Butov, C. W. Lai, D. S. Chemla, Y. E. Lozovik, K. L. Campman and A. C. Gossard. Observation of magnetically induced effective-mass enhancement of quasi-2D excitons. *Phys. Rev. Lett.*, **87**, 216804 (2001).

[108] J. Lee, E. S. Koteles and M. O. Vassell. Luminescence linewidths of excitons in GaAs quantum wells below 150 K. *Phys. Rev. B*, **33**, 5512 (1986).

[109] P. Stenius and A. L. Ivanov. Relaxation kinetics of quasi two-dimensional excitons coupled to a bath of bulk acoustic phonons. *Solid State Commun.*, **108**, 117 (1998).

[110] M. Levinshtein, S. Rumyantsev and M. Shur, editors. *Handbook Series on Semiconductor Properties (Vol. 1)* (World Science Publishing Co., Singapore, 1996).

[111] M. Neuberger. *III-V Semiconducting compounds* (Plenum, New York, 1971).

[112] L. R. Weisberg and J. Blanc. Measurements of the density of gaas. *J. Appl. Phys.*, **34**, 1002 (1963).

[113] A. V. Soroko and A. L. Ivanov. Phonon-assisted relaxation kinetics of statistically degenerate excitons in high-quality quantum wells. *Phys. Rev. B*, **65**, 165310 (2002).

[114] D. Snoke, S. Denev, Y. Liu, L. Pfeiffer and K. West. Long-range transport in excitonic dark states in coupled quantum wells. *Nature*, **418**, 754 (2002).

[115] A. V. Larionov, V. B. Timofeev, P. A. Ni, S. V. Dubonos, J. Hvam and K. Soerensen. Bose condensation of interwell excitons in double quantum wells. *JETP Letters*, **75**, 570 (2002).

[116] R. Rapaport, G. Chen, D. Snoke, S. H. Simon, L. Pfeiffer, K. West, Y. Liu and S. Denev. Charge separation of dense two-dimensional electron-hole gases: mechanism for exciton ring pattern formation. *Phys. Rev. Lett.*, **92**, 117405 (2004).

[117] A. M. Turing. The chemical basis of morphogenesis. *Philos. Trans. R. Soc. London B*, **327**, 37 (1952).

[118] L. S. Levitov, B. D. Simons and L. V. Butov. Pattern formation as a signature of quantum degeneracy in a cold exciton system. *Phys. Rev. Lett.*, **94**, 176404 (2005).

[119] V. I. Sugakov. Islands of exciton condensed phases in a two-dimensional system, the distribution of their sizes and coherence in position. *Solid State Commun.*, **134**, 63 (2005).

[120] A. A. Chernyuk and V. I. Sugakov. Ordered dissipative structures in exciton systems in semiconductor quantum wells. *Phys. Rev. B*, **74**, 085303 (2006).

[121] V. I. Sugakov. Formation of inhomogeneous structures of condensed phases of excitons in quantum wells. *Phys. Rev. B*, **76**, 115303 (2007).

[122] M. H. Szymanska and P. B. Littlewood. Excitonic binding in coupled quantum wells. *Phys. Rev. B*, **67**, 193305 (2003).

[123] D. Snoke, Y. Liu, S. Denev, L. Pfeiffer and K. West. Luminescence rings in quantum well structures. *Solid State Commun.*, **127**, 187 (2003).

[124] L. V. Butov, L. S. Levitov, A. V. Mintsev, B. D. Simons, A. C. Gossard and D. S. Chemla. Formation mechanism and low-temperature instability of exciton rings. *Phys. Rev. Lett.*, **92**, 117404 (2004).

[125] D. Snoke, S. Denev, Y. Liu, S. Simon, R. Rapaport, G. Chen, L. Pfeiffer and K. West. Moving beyond a simple model of luminescence rings in quantum well structures. *J. Phys.: Condens. Matter*, **16**, S3621 (2004).

[126] S. Denev, S. H. Simon and D. W. Snoke. Luminescence ring formation in quantum wells – a model with Coulomb interaction. *Solid State Commun.*, **134**, 59 (2005).

[127] G. Chen, S. H. Simon, L. Pfeiffer and K. West. Dynamics of the in-plane charge separation front in a two-dimensional electron-hole gas. *Phys. Rev. B*, **71**, 041301 (2005).

[128] I. V. Kukushkin. *Unpublished* (2002).

[129] I. V. Kukushkin, K. von Klitzing, K. Ploog, V. E. Kirpichev and B. N. Shepel. Reduction of the electron density in $GaAs/Ga_{1-x}Al_xAs$ single heterojunctions by continuous photoexcitation. *Phys. Rev. B*, **40**, 4179 (1989).

[130] A. Zrenner, J. M. Worlock, L. T. Florez, J. P. Harbison and S. A. Lyon. Intrinsic bistability in an optically pumped quantum well structure. *Appl. Phys. Lett.*, **56**, 1763 (1990).

[131] J. Shah. *Hot Carriers in Semiconductor Nanostructures: Physics and Applications* (Academic Press, New York, 1992).

[132] L. V. Butov, C. W. Lai, A. L. Ivanov, A. C. Gossard and D. S. Chemla. Towards Bose-Einstein condensation of excitons in potential traps. *Nature*, **417**, 47 (2002).

[133] C. W. Lai, J. Zoch, A. C. Gossard and D. S. Chemla. Phase diagram of degenerate exciton systems. *Science*, **303**, 503 (2004).

[134] V. Negoita, D. W. Snoke and K. Eberl. Harmonic-potential traps for indirect excitons in coupled quantum wells. *Phys. Rev. B*, **60**, 2661 (1999).

[135] A. T. Hammack, N. A. Gippius, S. Yang, G. O. Andreev, L. V. Butov, M. Hanson and A. C. Gossard. Excitons in electrostatic traps. *J. Appl. Phys.*, **99**, 066104 (2006).

[136] A. T. Hammack, M. Griswold, L. V. Butov, L. E. Smallwood, A. L. Ivanov and A. C. Gossard. Trapping of cold excitons in quantum well structures with laser light. *Phys. Rev. Lett.*, **96**, 227402 (2006).

[137] A. Gärtner, A. W. Holleitner, J. P. Kotthaus and D. Schuh. Drift mobility of long-living excitons in coupled GaAs quantum wells. *Appl. Phys. Lett.*, **89**, 052108 (2006).

[138] A. V. Gorbunov and V. B. Timofeev. Collective state in a bose gas of interacting interwell excitons. *JETP Lett.*, **83**, 146 (2006).

[139] Z. Vörös, D. W. Snoke, L. Pfeiffer and K. West. Trapping excitons in a two-dimensional in-plane harmonic potential: Experimental evidence for equilibration of indirect excitons. *Phys. Rev. Lett.*, **97**, 016803 (2006).

[140] L. Mouchliadis and A. L. Ivanov. Anti-trapping of indirect excitons by a current filament. *J. Phys.: Condens. Matter*, **19**, 295215 (2007).

[141] F. Stern and W. E. Howard. Properties of semiconductor surface inversion layers in the electric quantum limit. *Phys. Rev.*, **163**, 816 (1967).

[142] M. E. Portnoi and I. Galbraith. Variable-phase method and Levinsons theorem in two dimensions: Application to a screened Coulomb potential. *Solid State Commun.*, **103**, 325 (1997).

[143] M. E. Portnoi and I. Galbraith. Ionization degree of the electron-hole plasma in semiconductor quantum wells. *Phys. Rev. B*, **60**, 5570 (1999).

[144] N. B. B. Aouani, L. Mandhour, R. Bennaceur, S. Jaziri, T. Amand and X. Marie. Thermodynamic equilibrium of screened exciton system by electron-hole plasma in the two-dimensional structure. *Solid State Commun.*, **108**, 199 (1998).

[145] H. Reinholz. Mott effect for an electron-hole plasma in a two-dimensional structure. *Solid State Commun.*, **123**, 489 (2002).

[146] A. V. Larionov, V. B. Timofeev, J. Hvam and C. Soerensen. Collective behavior of interwell excitons in GaAs/AlGaAs double quantum wells. *JETP Lett.*, **75**, 200 (2002).

[147] Y. Naveh and B. Laikhtman. Excitonic instability and electric-field-induced phase transition towards a two-dimensional exciton condensate. *Phys. Rev. Lett.*, **77**, 900 (1996).

[148] L. V. Butov, A. Imamoglu, A. V. Mintsev, K. L. Campman and A. C. Gossard. Photoluminescence kinetics of indirect excitons in GaAs/Al$_x$Ga$_{1-x}$As coupled quantum wells. *Phys. Rev. B*, **59**, 1625 (1999).

[149] V. Negoita, D. W. Snoke and K. Eberl. Stretching quantum wells: A method for trapping free carriers in GaAs heterostructures. *Appl. Phys. Lett.*, **75**, 2059 (1999).

[150] J. P. Wolfe, W. L. Hansen, E. E. Haller, R. S. Markiewicz, C. Kittel and C. D. Jeffries. Photograph of an electron-hole drop in Germanium. *Phys. Rev. Lett.*, **34**, 1292 (1975).

[151] D. P. Trauernicht, A. Mysyrowicz and J. P. Wolfe. Strain confinement and thermodynamics of free excitons in a direct-gap semiconductor. *Phys. Rev. B*, **28**, 3590 (1983).

[152] R. Rapaport, G. Chen, S. Simon, O. Mitrofanov, L. Pfeiffer and P. M. Platzman. Electrostatic traps for dipolar excitons. *Phys. Rev. B*, **72**, 075428 (2005).

[153] T. Huber, A. Zrenner, W. Wegscheider and M. Bichler. Electrostatic exciton traps. *Phys. Stat. Sol. (a)*, **166**, R5 (1998).

[154] G. Chen, R. Rapaport, L. N. Pffeifer, K. West, P. M. Platzman, S. Simon, Z. Vörös and D. Snoke. Artificial trapping of a stable high-density dipolar exciton fluid. *Phys. Rev. B*, **74**, 045309 (2006).

[155] X. Zhu, P. B. Littlewood, M. S. Hybertsen and T. M. Rice. Exciton condensate in semiconductor quantum well structures. *Phys. Rev. Lett.*, **74**, 1633 (1995).

[156] A. Schmeller, W. Hansen, J. P. Kotthaus, G. Tränkle and G. Weimann. Franz-keldysh effect in a two-dimensional system. *Appl. Phys. Lett.*, **64**, 330 (1993).

[157] S. Zimmermann, A. O. Govorov, W. Hansen, J. P. Kotthaus, M. Bichler and W. Wegscheider. Lateral superlattices as voltage-controlled traps for excitons. *Phys. Rev. B*, **56**, 13414 (1997).

[158] S. Zimmermann, G. Schedelbeck, A. O. Govorov, A. Wixforth, J. P. Kotthaus, M. Bichler, W. Wegscheider and G. Abstreiter. Spatially resolved exciton trapping in a voltage-controlled lateral superlattice. *Appl. Phys. Lett.*, **73**, 154 (1998).

[159] K. Brunner, U. Bockelmann, G. Abstreiter, M. Walther, G. Böhm, G. Tränkle and G. Weimann. Photoluminescence from a single GaAs/AlGaAs quantum dot. *Phys. Rev. Lett.*, **69**, 3216 (1992).

[160] P. C. M. Cristianen, F. Piazza, J. G. S. Lok, J. C. Maan and W. van der Vleuten. Magnetic trap for excitons. *Physica B*, **249**, 624 (1998).

[161] A. Ashkin. Acceleration and trapping of particles by radiation pressure. *Phys. Rev. Lett.*, **24**, 156 (1970).

[162] T. Kuga, Y. Torii, N. Shiokawa, T. Hirano, Y. Shimizu and H. Sasada. Novel optical trap of atoms with a doughnut beam. *Phys. Rev. Lett.*, **78**, 4713 (1997).

[163] D. M. Stamper-Kurn, M. R. Andrews, A. P. Chikkatur, S. Inouye, H. J. Miesner, J. Stenger and W. Ketterle. Optical confinement of a Bose-Einstein condensate. *Phys. Rev. Lett.*, **80**, 2027 (1998).

[164] L. V. Butov, A. L. Ivanov, A. Imamoglu, P. B. Littlewood, A. A. Shashkin, V. T. Dolgopolov, K. L. Campman and A. C. Gossard. Stimulated scattering of indirect excitons in coupled quantum wells: Signature of a degenerate Bose-gas of excitons. *Phys. Rev. Lett.*, **86**, 5608 (2001).

[165] J. Feldmann, G. Peter, E. O. Göbel, P. Dawson, K. Moore, C. Foxon and R. J. Elliott. Linewidth dependence of radiative exciton lifetimes in quantum wells. *Phys. Rev. Lett.*, **59**, 2337 (1987).

[166] G. D. Smith. *Numerical solution of partial differential equations* (Oxford University Press, 1965).

[167] J. Crank. *The Mathematics of Diffusion* (Oxford University Press, 1975).

[168] S. Yang, A. T. Hammack, M. M. Fogler, L. V. Butov and A. C. Gossard. Coherence length of cold exciton gases in coupled quantum wells. *Phys. Rev. Lett.*, **97**, 187402 (2006).

[169] A. V. Gorbunov and V. B. Timofeev. Large-scale coherence of the Bose condensate of spatially indirect excitons. *JETP Lett.*, **84**, 329 (2006).

[170] J. Kasprzak, M. Richard, S. Kundermann, A. Baas, P. Jeambrun, J. M. J. Keeling, F. M. Marchetti, M. H. Szymańska, R. André, J. L. Staehli, V. Savona, P. B. Littlewood, B. Deveaud and L. S. Dang. Bose-Einstein condensation of exciton polaritons. *Nature*, **443**, 409 (2006).

[171] H. Deng, G. S. Solomon, R. Hey, K. H. Ploog and Y. Yamamoto. Spatial coherence of a polariton condensate. *Phys. Rev. Lett.*, **99**, 126403 (2007).

[172] E. Hecht. *Optics, 4th ed.* ((Addison-Wesley, Reading, Massachusetts, 2001).

[173] R. Loudon. *The quantum theory of light* (Clarendon Press, Oxford, 1973).

[174] I. S. Gradshteyn and I. M. Ryzhik. *Table of integrals, series, and products* (Academic Press Inc., New York, 1980).

[175] M. Naraschewski and R. J. Glauber. Spatial coherence and density correlations of trapped bose gases. *Phys. Rev. A*, **59**, 4595 (1999).

[176] M. Abramowitz and I. A. Stegun, editors. *Handbook of Mathematical Functions with Formulas, Graphs, and Mathematical Tables* (Dover, New York, 1965).

[177] D. M. Kachintsev and S. E. Ulloa. Dielectric function and collective modes of two-dimensional interacting bosons. *Phys. Rev. B*, **50**, 8715 (1994).

[178] J. M. Ziman. *Principles of the Theory of Solids* (Cambridge University Press, 1979).